Dissertation zur Erlangung des Doktorgrades
an der Fakultät für Chemie und Pharmazie
der Ludwig-Maximilians-Universität München

A Bridge between Salts and Metals: Intermetallic Compounds with Polar Metallic Bonding

Jonathan Sappl
aus Starnberg, Deutschland
2020

Dissertation zur Erlangung des Doktorgrades
an der Fakultät für Chemie und Pharmazie
der Ludwig-Maximilians-Universität München

A Bridge between Salts and Metals: Intermetallic Compounds with Polar Metallic Bonding

Jonathan Sappl
aus Starnberg, Deutschland
2020

Erklärung

Diese Dissertation wurde im Sinne von § 7 der Promotionsordnung vom 28. November 2011 von Herrn PD Dr. Constantin Hoch betreut.

Eidesstattliche Versicherung

Diese Dissertation wurde eigenständig und ohne unerlaubte Hilfe erarbeitet.

München, 13. Juli 2020

.....

Jonathan Sappl

Dissertation eingereicht am:	15.06.2020
1. Gutachter:	PD Dr. Constantin Hoch
2. Gutachter:	Prof. Dr. Dirk Johrendt
Mündliche Prüfung am:	09.07.2020

— Dank —

Mein persönlicher Dank gebührt vielen Menschen, bei denen als erstes meine Eltern und Großeltern zu nennen sind, die mich über all die Jahre unterstützt haben, ebenso meine Geschwister, die in Zeiten der Not stets zu mir hielten.

Des Weiteren danke ich den Professoren Dr. Wolfgang Schnick, Dr. Thomas Bein und Dr. Oliver Trapp, die mir durch ihre finanzielle Unterstützung das Erstellen dieser Arbeit ermöglicht haben.

Ganz besonderer Dank gebührt meinen Laborkollegen Anna-Katharina Hatz, Sascha Harm und Fabian Keßler, die nicht nur bei fachlichen, sondern auch bei persönlichen Fragen immer ein offenes Ohr hatten, die durch einen kleinen Stupser dafür sorgten, dass das Labor stets ordentlich war und die sehr zu dem guten Arbeitsklima beigetragen haben.

Zu erwähnen sind natürlich auch all die Mitarbeiter aus den Arbeitskreisen Schnick, Johrendt und Lotsch, mit denen allesamt ein gutes Auskommen war, die zu Probevorträgen zahlreich erschienen und auf Nachfrage stets konstruktive Kritik übten.

Auch meinen Praktikanten Robert Calaminus, Ralph Freund und Felix Jung möchte ich danken, da auch sie einen Teil zu dieser Arbeit beigetragen haben, indem sie nicht nur die von mir aufgetragenen Arbeiten erledigt, sondern auch eigene Ideen mit eingebracht haben.

Meinen Studienkollegen Elisabeth Rackles, Kerstin Gottschling, Jörn Dietze, Stefan Thumser und Patrick Hirschle gebührt ebenso Dank, da sie mich durchs Studium begleitet und viel zu meiner Charakterentwicklung beigetragen haben.

Zum Schluss möchte ich noch die wichtigste Person, die zum Gelingen dieser Arbeit geführt hat, benennen, meinen Betreuer PD Dr. P. Constantin Hoch, welcher stets mit Rat und Tat zur Seite stand und über all die Jahre mehr Freund als Chef wurde.

Contents

Chapter 1

Introduction

1.1 Polar Metallic Bonding

One essential topic affecting the properties of materials is the type of chemical bonding. In general, there are three basic bonding types: covalent, metallic and ionic bond. The gradual transition between covalent and metallic as well as ionic bonds is also known. The three bonding types and their transitions can be seen in the van-Arkel-Ketelaar triangle which is a simple graphic representation of this topic (see Figure 1.1). The triangle first proposed by van Arkel[1] shows the fundamental interatomic interactions on the three vertices: Ionic bond (CsF) on the top, covalent bond (F_2) on the left, metallic bond (Sn) on the right and their hybrids in between. However, the gradual transition from metallic to ionic bond is not well described. To describe this bonding type the term "polar metal" or "polar metallic bond" will be used in this work. To form a polar metallic bonding a high electronegativity difference (ΔEN) in combination with an endothermic electron affinity (EA) of the noble partner is essential. The ΔEN must be high enough for a considerable electron transfer but not high enough for a full electron transfer to the noble partner (which would result in the formation of Zintl phases, see below). If the ΔEN is too low intermetallic phases like Frank-Kasper or Hume-Rothery phases will be formed. A high ΔEN normally leads to formation of cation–anion

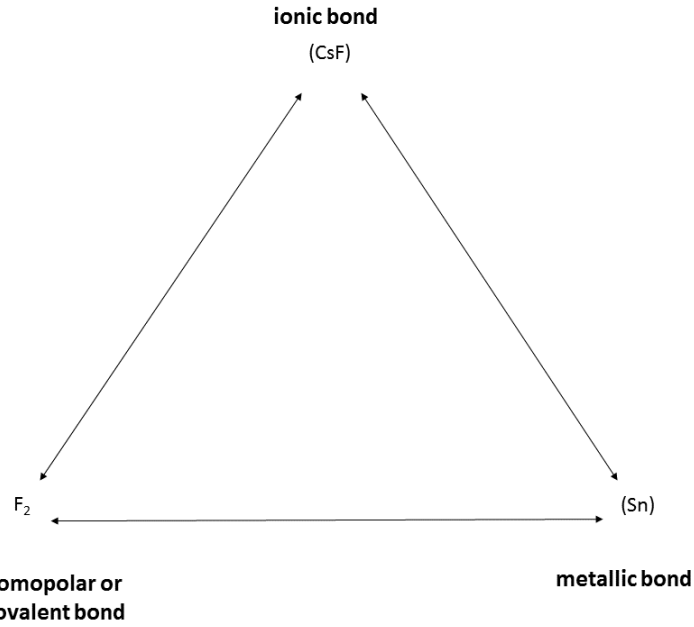

Figure 1.1: Van-Arkel-Ketelaar triangle, showing the three basic types of chemical bonding and their hybrids.[1]

pairs. In order to prevent this, the electron affinity of the nobler component must be chosen to be endothermic. Then, the combination of high ΔEN with unfavourable EA leads to a highly polar metallic compound.

Compounds with polar metal bonding often show interesting properties, like special magnetic properties and non-classical temperature dependence of the resistance and unconventional superconductivity.[2,3] Therefore, polar metal bonding may be the key to unlock new combinations of magnetic and electric properties.

1.2 Polar Metal Bonding in Other Contexts

The term "polar metal" (bonding) has often been used in the literature of the last few decades, yet it is not well defined.

The most frequent occurrence of the term is found within the context of "ferroelectric metals", as proposed by P.W. Anderson and E.I. Blount[4] in 1965. By martensitic phase transformations, they argued, cubic materials such as β-W-structured superconductors may adopt a tetragonal, non-centrosymmetric structure short above their superconducting transition temperatures T_c, as demonstrated by Batterman and Barrett.[5] Then, a polar axis and consequently ferroelectricity can occur. Today, this effect is known for e. g. thin film $NdNiO_3$[6] or non-centrosymmetric ($R3c$) $LiOsO_3$[7]. One substance family known for forming polar metals are the nickelate perovskites like $LaNiO_3$ or $NdNiO_3$, see Figure 1.2. Ferroelectric behavior in metals may seem counterintuitive, since usually the coexistence of metallic behavior and electric ordered dipoles is forbidden by Gauss's law which states that the net electric field in an electron conductor is zero due to effective charge screening. But the rule can be broken due to symmetry considerations in cases of weak electron-phonon coupling as given in systems with low carrier concentrations. A number of perovskite-related metalates are known today as polar antiferromagnetics and as multiferroic materials.[6]

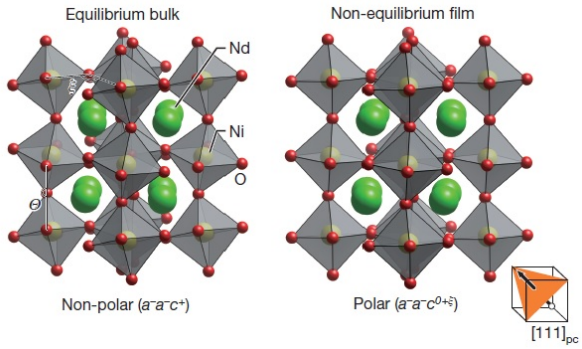

Figure 1.2: Left: The equilibrium bulk structure of metallic $NdNiO_3$. Right: The pseudocubic representation of the geometrically stabilized polar metal $NdNiO_3$-structure in non-equilibrium state on a $LaAlO_3$ (111) base (Figure published by Kim et al.[6]).

Multiferroics are materials that contain more than one of the primary ferroic properties in the same phase, as there are: ferroelasticity, ferromagnetism and ferroelectrictiy.[9] Multiferroic materials may find future application as data storage systems with long lifetimes and high data density in those cases were gigantic magnetoelectric effects and magnetism-driven ferroelectricity coexist.[10,11]

The term “polar metal” is in the most cases connected with the abovementioned class of perovskite-type multiferroic materials, however, there is a number of other contexts in which the term “polar metal”, or “polar metallic bonding” is applied. In coordination chemistry, for example, homodinuclear complexes with considerable metal-metal interactions are generally symmetrical "dimers" with a nonpolar metal-metal bond.[12] Polarity can be introduced, by a "one-sided" exchange of a ligand in homoleptic complexes, while having the same oxidation state of the metal.[12] Some examples can be seen in Figure 1.3. The metal atoms in example a and b have the same oxidation state, while the oxidation states in c and d differ, leading to an increased polarity of the metal-metal bond. In di- or polynuclear complexes the polar metal-metal bond can be found in a more expressed form when transition elements from the two ends of the d-block of the periodic table are involved,[13] for example see Figures 1.3 e and f.

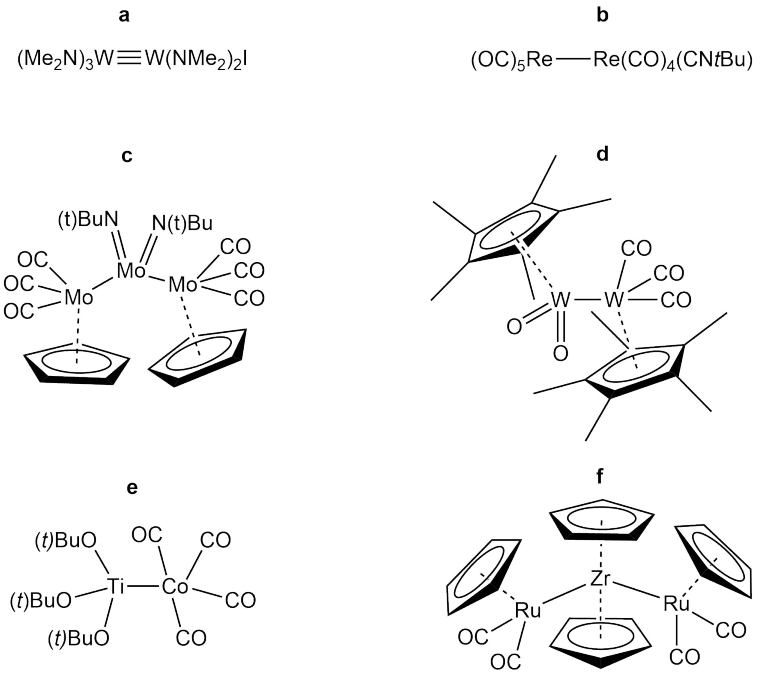

Figure 1.3: Homodimetallic complexes with polar metal-metal bonding and the same oxidation state: a: $W^{+III}{}_2(NMe_2)_5I$[16] b: *t*-Butylisocyanidenonacarbonyldirhenium(0) $Re^0{}_2(CO)_9(CNtBu)$[17]. Homodi(multi)-metallic complexes with polar metal-metal bonding and different oxidation state: c: $[(tBuN)_2Mo^{+IV}\{Mo^{+I}(CO)_3Cp\}_2]$[18] d: $(\eta^5\text{-}C_5Me_5)(CO)_3W^{+I}\text{–}W^{+V}(O)_2(\eta^5\text{-}C_5Me_5)$[19]. Heterodi(multi)-metallic complexes with polar metal-metal bonding: e: $(tert\text{-}C_4H_9O)_3Ti^{+III}Co^0(CO)_4$[20] f: $(C_5H_5)_2Zr^{+II}[Ru^{+I}(CO)_2C_5H_5]_2$[21]

In literature, the term “polar metallic bonding” is sometimes referred to when describing the height of the Schottky barrier creating polarity at the interface of a metallic conductor and a semiconductor.[14,15] It is named after Walter H. Schottky and describes a potential energy barrier for electrons formed on the intersection between a metal and a semiconductor. Examples would be: Al/Ge, Al/GaAs, or Al/AlAs.[15] For illustration see Figure 1.4. A good description of the situation can be found in literature:

> „The difference between the barrier heights of the anion- and cation-terminated interfaces results from a microscopic dipole generated by the screened charge of the polar semiconductor surface and its image charge at the metal surface.“[15]

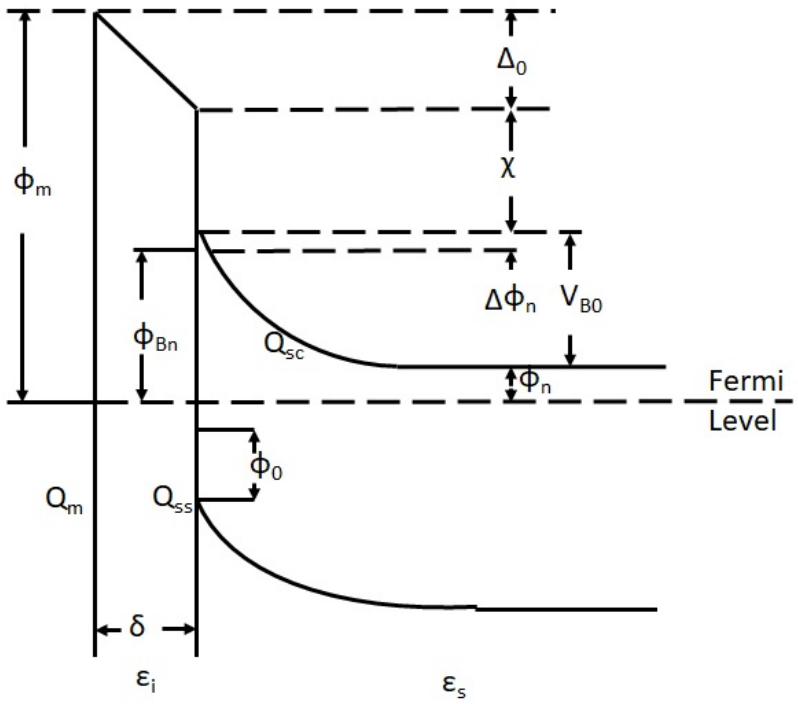

Figure 1.4: Energy band diagram of an interfacial layer contact with a metal-*n*-type-semiconductor (drawn after the original from Cowley and Sze[22]). ϕ_0 = energy level at surface, ϕ_m = work function of metal, ϕ_Bn = barrier height of metal-semiconductor surface barrier, ϕ_m = energy difference between conduction band and E_F in bulk semiconductor, $\Delta\phi_\mathrm{m}$ = image force barrier lowering, Δ_0 = potential across interfacial layer, V_B0 = diffusion potential, χ = electron affinity of semiconductor, ϵ_i = dielectric constant of interfacial layer, ϵ_s = dielectric constant of semiconductor, δ = thickness of interfacial layer, Q_ss = surface state charge density on semiconductor, Q_sc = space-charge density in semiconductor, Q_m = surface charge density on metal.

1.3 Amalgams - Models for Compounds with Polar Metal Bonding

A more chemical meaning of the term "polar metallic bonding" would be the Coulombic polarity created by partial electron transfer within a metallic phase in the sense of $M^{\delta+} - M^{\delta-}$. This would, in the van-Arkel-Ketelaar picture, correspond to a gradual transition from metallic to ionic bonding with increasing δ.

There are two methods our research group uses to prepare solids which can be taken as model substances for this kind of polar metallic bonding. One consists of the implementation of discrete building blocks of ionic character into a metallic matrix by reacting combination of ionic and metallic reactants in a suitable way, to maintain both ionic and metallic building units in a new, homogenous crystal structure.[23–27]

The second method has been used for this work and consists of creating a polar metallic bonding by increasing the ionic bonding contributions in intermetallic compounds. To provide an increase in Coulombic polarity in an intermetallic compound, the metallic components must exhibit a considerable difference in their respective electronegativities. In addition, the electron affinity of the nobler component has to be low enough to avoid the formation of anions which would result in to the formation of Zintl phases (see Chapter 1.4). Most elements have exothermic electron affinities often leading to a full electron transfer from the less noble component. For a polar metallic bonding, a less noble metal therefore has to be combined with a nobler metal with endothermic electronaffinity. There is only one example of a noble metal with an endothermic electron affinity – mercury. In addition, Hg is on the left side of the Zintl border. Due to this and the endothermic electron affinity the electron transfer from a less noble metal is always incomplete, as shown in numerous amalgams such as KHg[28], KHg_6[29] or $Eu_{10}Hg_{55}$[30]. Therefore, our research group mainly focused on amalgams of the less noble metals, including alkaline, alkaline earth and lanthanoid metals.[29–31] These amalgams often show "bad metal" behavior which means a high specific resistance and a low Ioffe-Regel limit (see Figure 1.5).[29,32] One reason why especially the Hg-rich amalgams are rarely known consists in the combination of generally low peritectical decomposition temperatures and at the same time highly exothermic reactions of the elements. To gain access to those amalgams, the isothermal electrolysis has proven a convenient preparation method.[29–34]

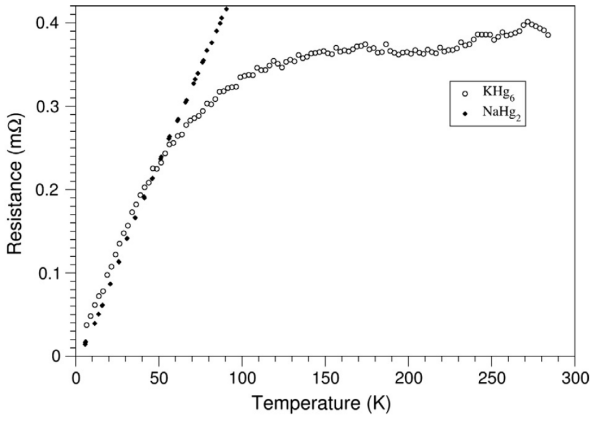

Figure 1.5: Resistance of KHg_6 depending on the temperature, in comparison to $NaHg_2$[32]. It shows aberration from ideal metallic behavior and a low Ioffe–Regel limit resistance (Figure published by Tambornino and Hoch[29]).

Electrolysis was first established in 1806 by two independent scientists. Jöns Jacob Berzelius conducted research on electrolytic reactions in Stockholm while Humphry Davy did the same in London.[35,36] Both of them did their work with a small amount of mercury as cathode and small portions of common salts. The anode was a wire which was in touch with the salt. With the help of the shortly before introduced Voltaic pile, they were able to observe the formation of amalgams. Humphry Davy also discovered a series of elements with the help of electrolysis like sodium, potassium, magnesium, calcium, strontium, barium and boron. Nowadays in industrial chemistry, electrolytic processes are still in use. It is used for anodic oxidation or to purify metals by reducing metal cations from solutions. The amalgam process is a very energy-consuming process and is used for the production of chlorine and soda lye from brine.[37,38] In chemical research, electrolysis is also in use. The most common electrolytic method in organic chemistry is probably the Kolbe electrolysis (formally a decarboxylative dimerization of two carboxylic acids). Apart from that, both electrolytic reduction and oxidation are used.[39] In previous works, of our group isothermal electrolysis was used to synthesize $Na_{11}Hg_{52}$.[32,40] Its synthesis was only possible via electrocrystallization due to the highly exothermal reaction of Na with Hg: The reaction temperature is so high that the low-lying decomposition temperature of the Hg-richest amalgam is always exceeded, and tempering of e. g. Hg-$NaHg_2$ mixtures of fitting compositions has to be performed at temperatures so low that kinetic effects prevent phase formation. The great advantage of the electrolytic method is its isothermal reaction under soft conditions which is almost perfect for strong exothermic reactions.

By electrolyzing a solution of an alkaline earth or alkali metal salt in an aprotic polar solvent, the cation can be inserted into the liquid mercury cathode. N,N-Dimethylformamide (DMF) has proven to be a suitable solvent with a wide temperature range from -61°C to 153°C. Iodides of the respective metals are preferred as starting materials for two reasons: Iodides have high polarity and therefore good solubility of metal salts, a high tolerance versus the applied voltages and there is an optical feedback as soon as the reaction starts due to the formation of iodine. Additionally, iodine is less aggressive towards anode materials than chlorine or fluorine. As stated above, mercury has a positive electron affinity which is necessary in terms of a polar metal bonding. It is liquid at room temperature which is also a prerequisite for preparative electrolysis. Our research group was able to obtain several new amalgams using this method.[29–31] Another advantage of this technique is that the electrolysis automatically stops once a solid phase is formed, resulting, in most of the cases, in a phase pure product. The applied isothermal electrolysis apparatus is built from glass and handmade. It is designed to be used under inert conditions. The two chambers are

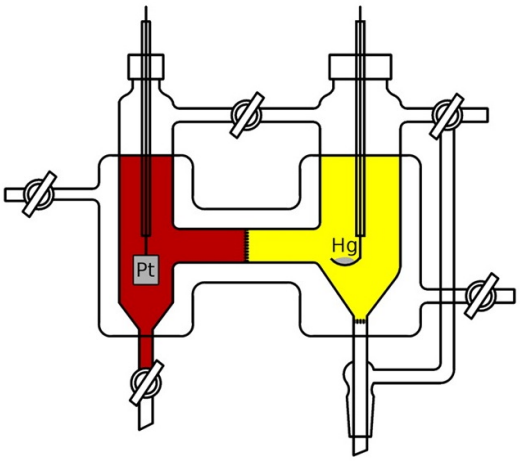

Figure 1.6: Apparatus of the isothermal electrolysis, used for the preparation of amalgams.[41]

separated by a glass frit. A Pt wire is used as anode. The cathode consists of an amalgamated copper spoon in which a small drop of mercury is suspended in cases of amalgam preparations. A schematic drawing can be seen in Figure 1.6. The isothermal electrolysis is not limited to Hg. In fact, every metal or metal-metal mixture which is liquid in the range of the used solvent can be used as cathode material. Testing other intermetallic systems may convenient in terms of preparation of intermetallic phases with polar metallic bonding.

1.4 Mercury-Free Compounds with Polar Metallic Bonding

The purpose of this work is to broaden the number of metals used as nobler components in intermetallic phases with Coulombic polarity and to transfer the methods and experiences gained from the synthesis of amalgams to other intermetallic systems. For this, several aspects have to be considered. Many metallic elements have only low electronegativity differences, resulting in the formation of intermetallic phases with no or only small ionic bonding contributions. This excludes Laves-, Heusler-, Frank-Kasper-, Hume-Rothery-phases etc. for our studies on intermetallic compounds with polar metal bonding.

Only a small number of phases with bonding properties between metallic and ionic are known, which are addressed as “nonclassical” Zintl phases. The term "Zintl phases" was introduced in 1941 by Laves in honor of the German chemist Eduard Zintl.[42] They are intermetallic compounds crystallizing in salt-like structures due to their high difference in electronegativity of their components. Later on, this definition was extended by Klemm and Busmann (Zintl-Klemm-Busmann concept). They stated that the metal transfers its electrons to the nobler element, which then builds an anionic structure that can be understood following the 8 - *N* rule.[43] Classical Zintl phases have small band gaps at the Fermi level and show semiconducting properties. Most of these intermetallic compounds are red and transparent and can be reversibly dissolved and recrystallized from polar solvents. They have high melting points and almost no phase widths. On the contrary, nonclassical Zintl phases[44,46,47] show hypervalent bonding and a combination of ionic bonding contributions with metallic properties. The standard electron counting rules can still be used for the anionic substructures, e.g. shown on the examples of several antimony phases. These phases are interesting due to their rich structural chemistry. Antimony can form classical Zintl anions like in $BaSb_3$[48] showing an anionic network of di- and trivalent Sb atoms following the ionic separation $Ba^{2+}[Sb^{-}]_2[Sb^{0}]$ or nonclassical Zintl anions like in $Ca_{14}AlSb_{11}$[49]. $BaSb_3$ can be described as $Ba^{2+}[Sb^{-}]_2[Sb^{0}]$, forming antimony chains with three-connected Sb (Sb^0) centers and two-connected Sb (Sb^-) centers (see Figure 1.7). If the charge of Al is 3+ and Ca is 2+ in $Ca_{14}AlSb_{11}$ are 31 positive charges per formula unit. The Sb atoms split into eight isolated Sb atoms with 24 negative charges in total and a Sb_3 unit which should be charged -7 in total (see Figure 1.7). The Sb_3^{7-} group can be seen isoelectronic to I_3^{4-} or XeF_2, both known as electron-rich four-electron three-center species or classical hypervalent. The length of the Sb_3 Sb-Sb bonds (3.20 Å) and the linear geometry are consistent with this theory.[44] $Ca_{14}AlSb_{11}$ can be described as electron precise, however it does contain nonclassical

local coordination. The phase K_5Sb_4 [45] illustrates the case where electron counting rules do not apply anymore: in the crystal structure of K_5Sb_4 contains zig-zag groups of four Sb atoms (see Figure 1.7), with two-bonding internal and single-bonding terminal Sb atoms, which would sum up to $[Sb_4]^{6-}$. To summarize, the term "nonclassical Zintl phase" is used to describe Zintl phases with hypervalent bonding and nonclassical coordination and for non-electron precise compounds.

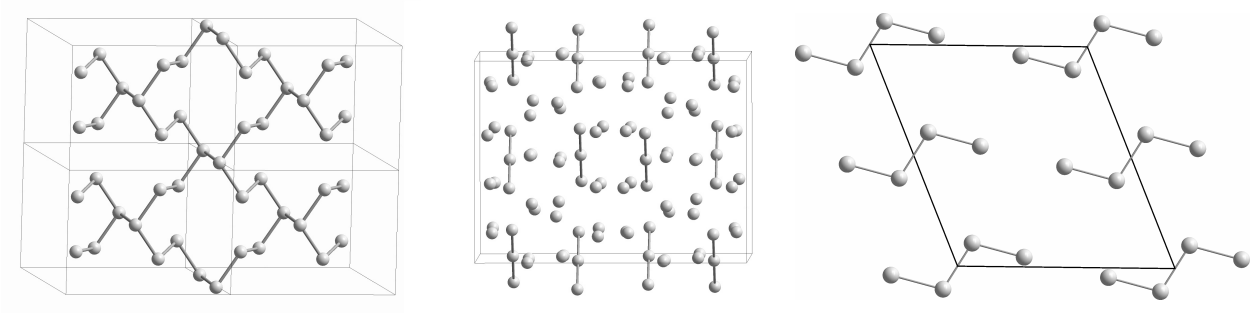

Figure 1.7: Left: The Sb chains of $BaSb_3$ including three-connected Sb^0 centers and two-connected Sb^- centers (classical Zintl anion). Center: The Sb atoms of $Ca_{14}AlSb_{11}$ with isolated Sb atoms and linear Sb_3 units (nonclassical Zintl anion). Right: $[Sb_4]$ anionic substructure in K_4Sb_5 with two-connected central Sb^- and single-bonding terminal Sb^{2-} atoms (non-classical Zintl anion).

Nonclassical Zintl phases can have interesting properties. It is stated that phases including mixed- or intermediate-valent rare-earth elements can have anomalous physical behavior such as heavy fermion occurrence, Kondo insulating phenomena and also technologically relevant properties such as anomalous thermal expansion and large thermoelectric power. [50] As mentioned above, the term "non-classical Zintl phases" is not sharply defined. Therefore, there is no systematic approach to create such compounds and already existent compounds are often not viewed under these aspects. A few examples for nonclassical Zintl phases which were pinpointed by the authors would be GaGe [50], $Yb_8Ge_3Sb_5$ [51] or $Ca_{14}AlSb_{11}$ [49].

The so-called Zintl border is a line separating the third and the fourth main group in the periodic table. By combining alkali or alkaline earth metals with elements on the right side of the Zintl border (fourth main group, late transition metals), classical Zintl phases can be obtained. With elements on the left side (third main group), the electronegativity difference is not high enough for a full electron transfer to the more noble element, thus resulting in an incomplete electron transfer and in the formation of non-classical Zintl phases.

1.5 Li/Ga – a Promising System?

One point of interest (as mentioned above) of this work was to extend the preparative method of electrocrystallization to other systems than amalgams. Therefore, focusing on the left side of the "Zintl border", especially on Ga (which is convenient for isothermal electrolysis due to its low melting point) as noble metallic compound, seemed promising. By scanning the literature of alkali metal gallides, (see Table 1.1) problems in electron counting can be found in structures like Li_3Ga_{14} [52,53] or $LiGa_{3.42}$ [54].

Table 1.1: Binary compounds of Ga with alkali metals.

Lithium	Sodium	Potassium	Rubidium	Caesium
$LiGa$ [55]	$NaGa_4$ [59]	K_2Ga_3 [62]	$RbGa_7$ [65–67]	Cs_8Ga_{11} [69]
$LiGa_{3.42}$ [54]	$Na_{22}Ga_{39}$ [60]	KGa_3 [63]	$RbGa_3$ [68]	$CsGa_7$ [67]
Li_3Ga_{14} [52,53]	Na_7Ga_{13} [61]	K_3Ga_{13} [64]		$CsGa_3$ [67]
Li_2Ga_7 [56]				
Li_3Ga_2 [57]				
Li_2Ga [57]				
Li_5Ga_4 [58]				

Following these considerations, LiGa is an interesting example. It is often mentioned in context with Ga and classical Zintl phases. Zintl reported on this compound in 1933.[55] Although often claimed otherwise, it is not a classical Zintl phase, even in its earliest definition by Zintl who drew the Zintl border due to the experimental finding that alkali metal compounds of fourth and fifth main group metall(oid)s showed solubility in liquid ammonia whereas compounds with third main group metall(oid)s are insoluble. LiGa has a considerable phase width, shows metallic conductivity and its electronic structure shows no band gap. It is better described as an ordered variant of a bcc packing. The low melting point and its place on the periodic table (left side of the Zintl-border) makes Ga (and its low melting eutectica Ga/Sn, Ga/Zn or Ga/In) a promising starting material for compounds with polar metal bonding. The cathode apparatus was redesigned for this purpose to enable the electrolysis process.[41] By adding an amperemeter information about the reaction process could be obtained. It also grants evaluation of the reaction independent from the optical feedback of coloring of the solution by iodine formation. After adjusting the apparatus for new systems, first experiments with Li, K, Na, Rb and Cs salt solutions were made. Preliminary results of electrolysis of NaI, KI, RbI and CsI on a Ga cathode showed formation of very air-sensitive products in all cases. During the electrolysis of LiI in DMF with Ga as cathode we found first hints for the existence of a new Li-Ga phase. Studies on other cathode materials (Ga/Sn, Ga/Zn and Ga/In eutectic liquid mixtures) then were postponed while focusing on the Li-Ga-system.

Li-Ga-phases seemed promising within the context of polar intermetallic compounds for multiple reasons. Firstly, Li phases often differ from the analogous alkali metal phases (Na, K, Rb, Cs) as far as structural and electronic properties are concerned, which can be seen on the example LiSi. LiSi is the first in the row of alkali metal silicides with 1:1 composition (NaSi, KSi, RbSi and CsSi). It

does not contain isolated $(Si^{-})_4$-tetrahedra like the others, which would be analogous to molecular white phosphorus as expected for Si^{-} in a classical Zintl phase. It forms a three-dimensional three-connected Si net.[70] It nevertheless can be considered to be electron precise. However, other Li-Si phases which are interesting from the point of view of anode materials in Li-ion batteries show a number of peculiarities: There is no phase $Li_{16}Si_4$ which would be electron precise, containing isolated Si^{4-} anions, isoelectronic and isovalent to noble gas atoms. The Li-richest silicide is $Li_{15}Si$, contains isolated Si atoms and is a metal. Also other Li-rich silicides (and germanides) are metallic, cannot be described with electron-precise counting and show phase widths. This is typical for Li-containing systems, in contrast to the heavier alkali metals.

Secondly, as mentioned, Ga is on the left side of the Zintl border and therefore should not form classical Zintl anions. Thirdly, in the Li-Ga system, on the Ga-rich side there are many reported phases of which the existences and structures are not clear until now, like "$LiGa_4$"[71], "$LiGa_2$"[72], "$LiGa_3$"[72], "$LiGa_6$"[73], "Li_3Ga_8"[73] or "Li_5Ga_9"[73]. In Figure 1.8 the phase-diagram used for this work is given.[74] On the Ga-rich side, which is of interest for the isothermal electrolysis, the only confirmed phase is Li_3Ga_{14}[52], all the other named Ga-rich phases are not included (except $LiGa_2$, marked with (?)). It could be possible that some of these phases are existent and could be synthesized with the help of electrocrystallization, and they also may have show polar metallic bonding in the above-mentioned sense.

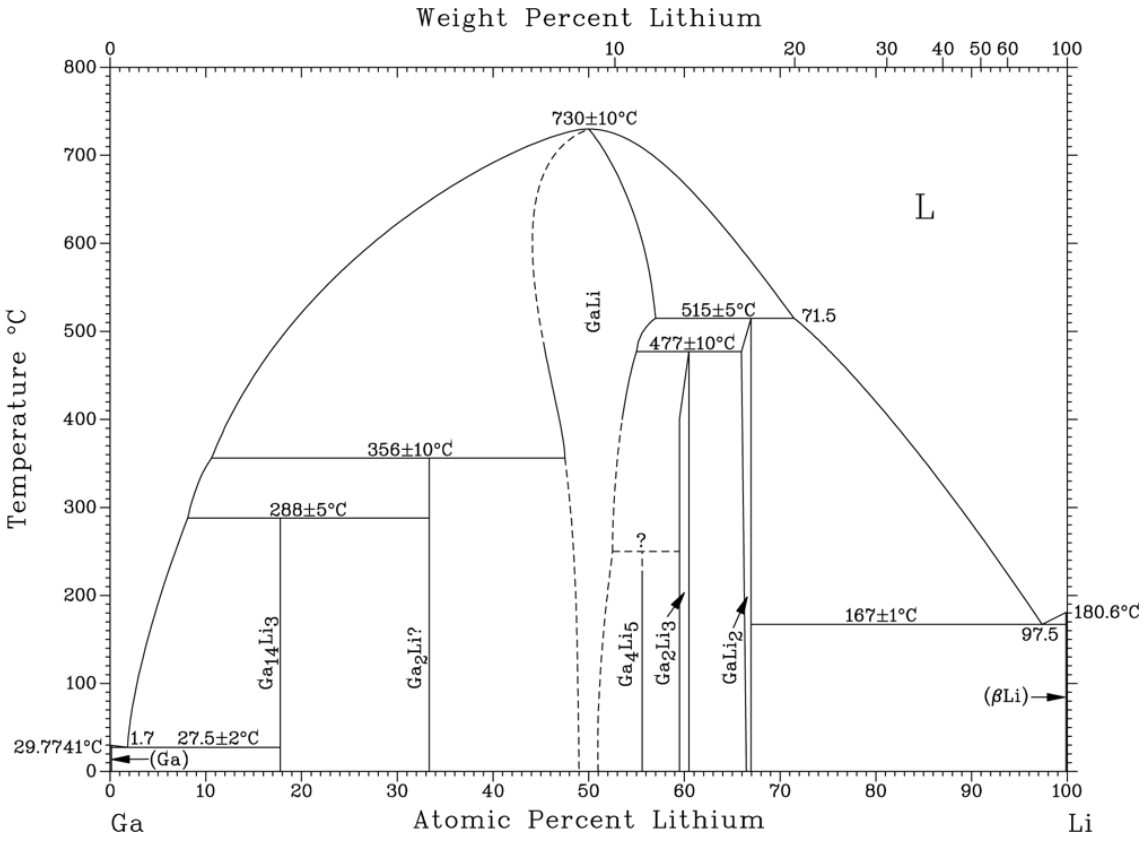

Figure 1.8: Phase diagram of Ga and Li by Sangster and Pelton.[74]

1.6 Overview of This Work

This section gives a short explanation of the organization of this work. In Chapter 2 the main results are presented in the form of peer-reviewed publications. Chapter 2.1 presents the new binary copper amalgam Cu_3Hg, which was gained as byproduct via electrocrystallization. The structure is described based on single crystal data.

The high reactivity of Li-Ga-phases were the reason for the second publication in Chapter 2.2. It describes the use of LiGa as intermetallic precursor for the formation of compounds with potential interest in electroactive materials, such as $LiGaO_2$ or $LiGaS_2$.

The third publication (Chapter 2.3) shows three new binary Li-Ga phases, as there are: $LiGa_6$, $LiGa_2$ and $Li_{11}Ga_{24}$. Their crystal structures are discussed on the basis of single crystal data and Rietveld refinements of powder samples. The DOS (Density Of States) for $LiGa_6$, "Li_6Ga_{14}", an ordered variant of the Li-deficient compound $Li_{6-x}Ga_{14}$ with $2 \leq x \leq 4$, $LiGa_2$ and LiGa are calculated and DSC (Differential Scanning Calorimetry) and conductivity measurements were performed in order to establish a new version of the Ga-rich part of the Li-Ga phase diagram.

A short summary about all results is given in Chapter 3. It summarizes the main aspects of each publication and gives a short overview.

In the last Chapter (see Chapter 4) a conclusion and outlook is given. It puts the results into context with the aspects of polar metallic bonding discussed in the Introduction, and some new pathways are proposed on the basis of the gained insights towards targeted syntheses of new polar intermetallic phases.

In Chapter 5 a list of publications with detailed author contributions can be found.

References

[1] A. E. van Arkel, *Molecules and Crystals* (Butterworth, London, 1949).

[2] X. Deng, J. Mravlje, R. Žitko, M. Ferrero, G. Kotliar, A. Georges, How Bad Metals Turn Good: Spectroscopic Signatures of Resilient Quasiparticles, *Phys. Rev. Lett.* **110** (2013) 1-5, DOI: 10.1103/PhysRevLett.110.086401.

[3] V. J. Emery, S. A. Kivelson, Superconductivity in Bad Metals, *Phys. Rev. Lett.* **74** (1995) 3253-3256, DOI: 10.1103/PhysRevLett.74.3253.

[4] P. W. Anderson, E. I. Blount, Symmetry Considerations on Martensitic Transformations: "Ferroelectric" Metals?, *J. American Physical Society* **14** (1965) 217-219, DOI: 10.1103/PhysRevLett.14.217

[5] B. W. Batterman, C. S. Barrett, Crystal Structure of Superconducting V_3Si, *Phys. Rev. Lett.* **13** (1964) 390-392, DOI: 10.1103/PhysRevLett.13.390.

[6] T. H. Kim, D. Puggioni, Y. Yuan, L. Xie, H. Zhou, N. Campbell, P. J. Ryan, Y. Choi, J. -W. Kim, J. R. Patzner, S. Ryu, J. P. Podkaminer, J. Irwin, Y. Ma, C. J. Fennie, M. S. Rzchowski, X. Q. Pan, V. Gopalan, J. M. Rondinelli, C. B. Eom, Polar metals by geometric design *Nature* **533** (2016) 68-72, DOI: 10.1038/nature17628.

[7] Y. Shi, Y. Guo, X. Wang, A. J. Princep, D. Khalyavin, P. Manuel, Y. Michiue, A. Sato, K. Tsuda, S. Yu, M. Arai, Y. Shirako, M. Akaogi, N. Wang, K. Yamaura, A. T. Boothroyd, A ferroelectric-like structural transition in a metal. *Nat. Mater.* **12** (2013) 1024–1027, DOI: 10.1038/nmat3754

[8] J. M. Rondinelli, S. J. May, J. W. Freeland, Control of octahedral connectivity in perovskite oxide heterostructures: an emerging route to multifunctional materials discovery. *MRS Bull.* **37** (2012) 261–270.

[9] H. Schmid, Multi-ferroic magnetoelectrics, *Ferroelectrics* **162** (1994) 317-338, DOI: 10.1080/00150199408245120.

[10] J. F. Scott, Data storage: Multiferroic memories. *Nat. Mater.* **6** (2007) 256–257.

[11] M. Morin, E. Canévet, A. Raynaud, M. Bartkowiak, D. Sheptyakov, V. Ban, M. Kenzelmann, E. Pomjakushina, K. Conder, M. Medarde, Tuning magnetic spirals beyond room temperature with chemical disorder. *Nat. Commun.* **7** (2016) 13758.

[12] M. Herberhold, G.-X. Jin, Heterodimetallic Complexes with an Unbridged, Polar Metal–Metal Bond, *Angew. Chem. Int. Ed. Engl.* **33** (1994) 964-966, DOI: 10.1002/anie.199409641.

[13] L. H. Gade, Highly Polar Metal - Metal Bonds in "Early - Late" Heterodimetallic Complexes *Angew. Chem., Int. Ed.* **39** (2000) 2658-2678.

[14] W. Mönch (Ed.), Electronic structure of metal-semiconductor contacts, Jaca Book (Milano), 1990, ISBN: 978-94-009-0657-0.

[15] C. Berthold, N. Binggeli, A. Baldereschi, Schottky barrier heights at polar metal/semiconductor interfaces, *Phys. Rev. B* **68** (2003) 085323–1-085323–11, DOI: 10.1103/PhysRevB.68.085323.

[16] H. Schulz, K. Folting, J. C. Huffman, W. E. Streib, M. H. Chisholm. Studies of Monosubstituted Compounds of Formula $M_2(NMe_2)_5X$ (M=M), Where M = Mo and W and X = I, Alkyl, Aryl, and Diphenylphosphido, and the Bridged-l,l'-ferrocenyl Complex $W_2(NMe_2)_4(\mu$-$(C_5H_4)_2Fe)$ *Inorg. Chem.* **32** (1993) 6056-6066, DOI: 10.1021/ic00078a025.

[17] M. O. Albers, J. C. A. Boeyens, N. J. Coville, G. W. Harris, Synthesis and crystal structure of t-butylisocyanidenonacarbnyldirhenium(0): $Re_2(CO)_9(CNBu^t)$ *J. Organomet. Chem.* **260** (1984) 99-104, DOI: 10.1016/S0022-328X(00)98677-7

[18] J. Sundermeyer, D. Runge, J. S. Field, Direct Metal–Metal Bonds Between High and Low Valent Complex Fragments: The Reaction of Metal Bases with the Metal Acids $[Re(NR)_3]^+$ and $[Mo(NR)_2]^{2+}$ *Angew. Chem. Int. Ed. Engl.* **33** (1994) 678-681, DOI: 10.1002/anie.199406781.

[19] H. G. Alt, H. I. Hayen, R. D. Rogers, Preparation and Crystal Structure of the Dinuclear, Asymmetric Dioxo Complex $(\eta^5$-$C_5Me_5)(CO)_3W$–$W(O)_2(\eta^5$-$C_5Me_5)$ *J. Chem. Soc. Chem. Commun.* (1987) 1795-1796, DOI: 10.1039/C39870001795.

[20] D. Selent, R. Beckhaus, J. Pickardt, Heterodinuclear titanium-cobalt complexes: syntheses and properties. X-ray structure of $[(tert\text{-}C_4H_9O)_3TiCo(CO)_4]$(Ti-Co) *Organometallics* **12** (1993) 2857-2860, DOI: 10.1021/om00031a067.

[21] C. P. Casey, R. F. Jordan, A. L. Rheingold, $(C_5H_5)_2Zr[Ru(CO)_2C_5H_5]_2$. A metal-metal bonded zirconium-diruthenium complex *Organometallics* **3** (1984) 504-506, DOI: 10.1021/om00081a036.

[22] A. M. Cowley, S. M. Sze, Surface States and Barrier Height of Metal-Semiconductor Systems, *J. Appl. Phys.* **36** (1965) 3212-3220, DOI: https://doi.org/10.1063/1.1702952.

[23] C. Hoch, J. Bender, A. Simon, Suboxide mit komplexen Anionen: das Suboxoindat Cs_9InO_4, *Angew. Chem.* **121** (2009) 2451-2454, DOI: 10.1002/ange.200805736.

[24] C. Hoch, J. Bender, A. Wohlfarth, A. Simon, Die Suboxometallate A_9MO_4 (A = Rb, Cs; M = Al, Ga, In, Fe, Sc) , *Z. Anorg. Allg. Chem.* **635** (2009) 1777-1782, DOI: 10.1002/zaac.200900193.

[25] M. Wörsching, C. Hoch, Alkali Metal Suboxometalates-Structural Chemistry between Salts and Metals, *Inorg. Chem.* **54** (2015) 7058-7064, DOI: 10.1021/acs.inorgchem.5b01060.

[26] M. Wörsching, F. Tambornino, S. Datz, C. Hoch, Chemische Verzwilligung von Salz und Metall in den Subnitridometallaten $Ba_{23}Na_{11}(MN_4)_4$ mit M=V, Nb, Ta *Angew. Chem.* **128** (2016) 11026-11030, DOI: 10.1002/ange.201605113.

[27] M. Wörsching, S. K. Fricke, J. Minár, R. Niklaus, C. Hoch, $Ba_6(MN_4)N_2$-x ($M = Mo^{VI}/Ta^{V}$), a Subvalent Nitridometalate with Perovskite-like Crystal Structure, *Z. Anorg. Allg. Chem.* **645** (2019) 278-283, DOI: 10.1002/zaac.201800400.

[28] E. J. Duwell, N. C. Baenziger, The crystal structures of KHg and KHg_2, *Acta Crystallogr.* **8** (1955) 705-710, DOI: 10.1107/S0365110X55002168.

[29] F. Tambornino, C. Hoch, Bad metal behaviour in the new Hg-rich amalgam KHg_6 with polar metallic bonding, *J. Alloys Compd.* **618** (2015) 299-304, DOI: 10.1016/j.jallcom.2014.08.173.

[30] F. Tambornino, C. Hoch, The Mercury-richest Europium Amalgam $Eu_{10}Hg_{55}$, *Z. Anorg. Allg. Chem.* **641** (2015) 537-542, DOI: 10.1002/zaac.201400561.

[31] F. Tambornino, K. Schwärzer, C. Hoch, Synthesis and characterization of $La_{11+x}Hg_{45-x}$ and $RE_{11}Hg_{44.5}$ (RE = Nd, Sm) as hettotypes of the $Sm_{11}Cd_{45}$ structure type, *J. Solid State Chem.* **242** (2016) 162-169, DOI: 10.1016/j.jssc.2016.07.001.

[32] C. Hoch, A. Simon, $Na_{11}Hg_{52}$ - Komplexität in einem polaren Metall, *Angew. Chem.* **124** (2012) 3316-3319, DOI: 10.1002/ange.201108064.

[33] C. Hoch, A. Simon, Tetramethylammoniumamalgam, $[N(CH_3)_4]Hg_8$, *Z. Anorg. Allg. Chem.* **632** (2006) 2288-2294, DOI: 10.1002/zaac.200600163.

[34] C. Hoch, A. Simon, Cs_2Hg_{27}, das quecksilberreichste Amalgam - ein naher Verwandter der Bergman-Phasen, *Z. Anorg. Allg. Chem.* **634** (2008) 853-856, DOI: 10.1002/zaac.200700535.

[35] H. Davy, On some chemical agencies of electricity (Bakerian Lecture of 1807), *Phil. Trans. R. Soc.* London **97** (1807) 1-56.

[36] J. J. Berzelius, Föreläsningar i Djurkemien, Carl Delén (Stockholm), 1806.

[37] T. F. O'Brien, T. V. Bommaraju, F. Hine, Handbook of Chlor-Alkali Technology, Springer (New York), 2005.

[38] I. Moussallem, J. Jörrisen, U. Kunz, S. Pinnow, T. Turek, Chlor-alkali electrolysis with oxygen depolarized cathodes: history, present status and future prospects, *J. Appl. Electrochem.* **38** (2008) 1177-1194, DOI: 10.1007/s10800-008-9556-9.

[39] F. D. Popp, H. P. Schultz, Electrolytic reduction of organic compounds, *Chem. Rev.* **62** (1962) 19-40, DOI: 10.1021/cr60215a002.

[40] C. Hoch, A. Simon, $Na_{11}Hg_{52}$ - complexity in a polar metal, *Angew. Chem. Int. Ed.* **51** (2012) 3262-3265, DOI: 10.1002/anie.201108064.

[41] F. Tambornino, J. Sappl, F. Pultar, T.M. Cong, S. Hübner, T. Giftthaler, C. Hoch, Electrocrystallization: A Synthetic Method for Intermetallic Phases with Polar Metal–Metal Bonding, *Inorg. Chem.* **55** (2016) 11551-11559, DOI: 10.1021/acs.inorgchem.6b02068.

[42] F. Laves, Eduard Zintls Arbeiten über die Chemie und Struktur von Legierungen *Naturwiss.* **29** (1941) 244-255, DOI: 10.1007/BF01479157.

[43] W. Klemm, E. Busmann, Volumeninkremente und Radien einiger einfach negativ gelandener Ionen *Z. Anorg. Allg. Chem.* **319** (1963) 297-311, DOI: 10.1002/zaac.19633190511.

[44] G. A. Papoian, R. Hoffmann, Hypervalent bonding in one, two and three dimensions: extending the Zintl-Klemm concept to nonclassical electron-rich networks, *Angew. Chem. Int. Ed.* **39** (2000) 2408-2448, DOI: 10.1002/1521-3773(20000717)39:14<2408::AID-ANIE2408>3.0.CO;2-U.

[45] M. Somer, M. Hartweg, K. Peters, H. G. von Schnering, Crystal structure of pentapotassium tetraantimonide, *Z. Kristallogr.* **195** (1991) 103-104, DOI: 10.1524/zkri.1991.195.14.103.

[46] J.D. Corbett, Polyatomic Zintl anions of the post-transition elements, *Chem. Rev.* **85** (1985) 383-397, DOI: 10.1021/cr00069a003.

[47] T. F. Fässler (Ed.), Zintl Phases, priciples and recent developments, in: Structure and Bonding Vol. 139, Springer (Berlin, Heidelberg), 2011.

[48] K. Deller, B. Eisenmann, $BaSb_3$, ein Antimonid mit einem zweidimensional unendlichen $[Sb_3^{2-}]_n$ - Polyanion / $BaSb_3$, an Antimonide with an Infinite Twodimensional $[Sb_3^{2-}]_n$ - Anion *Z. Naturforsch., B* **33** (1978) 676-677, DOI: 10.1515/znb-1978-0626.

[49] G. Cordier, H. Schäfer M. Stelter, Darstellung und Struktur der Verbindung $Ca_{14}AlSb_{11}$, *Z. Anorg. Allg. Chem.* **519** (1984) 183-188, DOI: 10.1002/zaac.19845191219.

[50] J. R. Salvador, F. Guo, T. Hogan, M. G. Kanatzidis, Zero thermal expansion in YbGaGe due to an electronic valence transition, *Nature* **425** (2003) 702-705, DOI: 10.1038/nature02011.

[51] J. R. Salvador, D. Bilc, S. D. Mahanti, T. Hogan, F. Guo, M. G. Kanatzidis, $Yb_8Ge_3Sb_5$, a Metallic Mixed-Valent Zintl Phase Containing the Polymeric$^1_\infty[Ge_3^{4-}]$ Anions. *J. Am. Chem. Soc.* **126** (2004) 4474-4475, DOI: 10.1021/ja0395487.

[52] C. Belin, R. J. Ling, The unexpected lithium-deficient phase of Li_3Ga_7: Synthesis and X-ray structure of Li_3Ga_{14}.*Solid State Chem.* **45** (1982) 290-292, DOI: 10.1016/0022-4596(82)90285-7.

[53] J. Stoehr, H. Schaefer, Ga-Clusterverbaende im Li_3Ga_{14}. *Rev. Chim. Miner.* **19** (1982) 122-127.

[54] C. Belin, Synthesis and crystal structure of the nonstoichiometric phase Li $Ga_{3.42}$. *Rev. Chim. Miner.* **21** (1984) 263-271.

[55] E. Zintl, G. Brauer, über die Valenzelektronenregel und die Atomradien unedler Metalle in Legierungen. *Z. Phys. Chem.* **B 20** (1933) 245-271, DOI: 10.1515/zpch-1933-2023.

[56] M. Tillard-Charbonnel, C. Belin, J. L. Soubeyroux, The lithium-gallium intermetallic system: electrochemical and neutron powder diffraction study of the lithium deficient phase Li_2Ga_7. *J. Solid State Inorg. Chem.* **27** (1990) 759-769.

[57] W. Mueller, J. Z. Stoehr, Die Kristallstruktur von Li_2Ga und Li_3Ga_2. *Z. Naturforsch. B,* **32** (1977) 631-636, DOI: 10.1515/znb-1977-0607.

[58] J. Stoehr, H. Z. Schaefer, Darstellung und Struktur von Li_5Ga_4. *Anorg. Allg. Chem.* **474** (1981) 221-225, DOI: 10.1002/zaac.19814740323.

[59] G. Bruzzone, The D13 structure type in intermetallic compounds. *Acta Crystallogr. B,* **25** (1969) 1206-1207, DOI: 10.1107/S0567740869003761.

[60] R. G. Ling, C. Belin, Structure of the intermetallic compound $Na_{22}Ga_{39}$ (ca. 36.07% Na). *C. Acta Crystallogr. B,* **38** (1982) 1101-1104, DOI: 10.1107/S0567740882005068.

[61] U. Frank-Cordier, G. Cordier, H. Z. Schaefer, Die Struktur des Na_7Ga_{13} - I und ein Konzept zur bindungsmaessigen Deutung. *Naturforsch. B,* **37** (1982) 119-126, DOI: 10.1515/znb-1982-0201.

[62] R. W. Henning, J. D. Corbett, Formation of isolated nickel-centered gallium clusters in $Na_{10}Ga_{10}Ni$ and a 2-D network of gallium octahedra in K_2Ga_3. *Inorg. Chem.* **38** (1999) 3883-3888, DOI: 10.1021/ic990335l.

[63] C. Belin, G. Rong, Le systeme potassium-gallium. Preparation et structure cristalline du compose intermetallique KGa_3. *C. R. Seances Acad. Sci., Ser. 2* **294** (1982) 1083-1086.

[64] C. Belin, The structure determination of a new intermetallic compound K_3Ga_{13}. *Acta Crystallogr. B,* **36** (1980) 1339-1343, DOI: 10.1107/S0567740880006048.

[65] C. Belin, Synthesis and structure determination of the new intermetallic compound $RbGa_7$. *Acta Crystallogr. B,* **37** (1981) 2060-2062, DOI: 10.1107/S0567740881007966.

[66] R. E. Marsh, F. H. Herbstein, Some additional changes in space groups of published crystal structures. *Acta Crystallogr. B,* **39** (1983) 280-287, DOI: 10.1107/S0108768183002402.

[67] J. H. N. van Vucht, On the crystal structures of some compounds of gallium with potassium, rubidium and cesium. *J. Less-Common Met.* **108** (1985) 163-175, DOI: 10.1016/0022-5088(85)90440-0.

[68] R.-G. Ling, C. Belin, Preparation and crystalstructure determination of the new intermetallic compound $RbGa_3$. *Z. Anorg. Allg. Chem.* **480** (1981) 181-185, DOI: 10.1002/zaac.19814800923.

[69] R. W. Henning, J. D. Corbett, Cs_8Ga11, a new isolated cluster in a binary gallium compound. A family of valence analogues $A_8Tr_{11}X$: A= Cs, Rb; Tr= Ga, In, Tl; X= Cl, Br, I. *Inorg. Chem.* **36** (1997) 6045-6049, DOI: 10.1021/ic970904u.

[70] J. Evers, G. Oehlinger, G. Sextl, LiSi a unique Zintl phase - although stable, it long evaded synthesis, *Eur. J. Solid State Inorg. Chem.* **34** (1997) 773-784, DOI: 10.1002/chin.199813026.

[71] S. P. Yatsenko, K. A. Chuntonov, S. I. Alyamovsky, E. N. Diyeva, *Izv. Akad. NaukSSR Met.* **1** (1973) 185-188.; in Russian; TR: *Russ. Metall* **1** (1973) 131-133.

[72] S. P. Yatsenko, Peculiarities chemical interaction of Ga in binary alloys *J. Chim. Phys.* **74** (1977) 836-843, DOI: 10.1051/jcp/1977740836.

[73] M. Tillard-Charbonnel, C. Belin, Le système lithium–gallium. Redétermination du diagrammedes équilibres de phases dans le domaine Ga–LiGa. *C. R. Acad. Sci. Paris* **306** (1988) 1161-1164.

[74] J. Sangster, A. D. Pelton, The Ga–Li (Gallium–Lithium) System. *J. Phase Equilib.* **12** (1991) 33-36, DOI: 10.1007/BF02663670.

Chapter 2

Results

2.1 Stuck in Our Teeth? Crystal Structure of a New Copper Amalgam, Cu_3Hg

Jonathan Sappl, Ralph Freund and Constantin Hoch

Department Chemie, Ludwig-Maximilians-Universität München, Butenandtstraße 5-13 (D), D-81377 München, Germany, Phone: +49 (0)89 2180-77421, Fax: +49 (0)89 2180-77440

published in: *Crystals* **7** (2017) 352-363. DOI: 10.3390/cryst7120352

2.1.1 Abstract

We have synthesised a new Cu amalgam, the Cu-rich phase Cu_3Hg. It crystallises with the Ni_3Sn structure type with a hexagonal unit cell (space group $P6_3/mmc$, $a = 5.408(4)$ Å, $c = 4.390(3)$ Å) and shows some mixed occupancy of Cu on the Hg site, resulting in a refined composition of $Cu_{3.11}Hg_{0.89}$. This is the first example of an amalgam with Ni_3Sn structure type where Hg is located mainly on the Sn site. Cu_3Hg might be one of the phases constituting dental amalgams and therefore has a major relevance, as well as the only Cu amalgam phase described so far, Cu_7Hg_6 with γ-brass structure. It occurs as byphase in our samples. Thermal decomposition of Cu amalgam samples in dynamic vacuum yields nanostructured copper networks, possibly suitable for catalytic applications.

2.1.2 Introduction

Modern dental amalgams consist of Hg, Ag, Sn, Cu and minor metallic additives. In order to prepare a typical amalgam filling, liquid mercury is mixed with powders or shavings of an alloy containing Ag, Sn and Cu in the suitable composition: 40–70 weight-% Ag, 12–30% Sn and 12–24% Cu. Additives can be Zn, In or Pd up to ca. 4%[1–3]. The alloy is mixed with an equal weight amount of Hg to form the plastic amalgam solidifying within minutes to hours. The solidification goes along with formation of a number of intermetallic phases. The most important in the resulting metal matrix composite are Ag_2Hg_3 as the major matrix phase, Ag_3Sn as the mechanically strongest phase, Sn_8Hg as the most corrosive phase, Ag_5Sn, Cu_6Sn_5 and Cu_3Sn amongst others[4,5]. The $\gamma 2$-phase Sn_8Hg is posing a major problem as it is relatively corrosive and leads to degradation of the filling over the years, especially at the tooth-amalgam interface. Today, so-called $\gamma 2$-free amalgams are in use which are higher in Cu content[6,7]. As the reaction takes place at physiological temperatures, the resulting alloy may not be the thermodynamically stable system. Other combinations of the metal atoms may also be considered: Cu amalgams and Ag-Cu solid solutions as well as ternary and quaternary phases may also come into play at equilibrium conditions.

Table 2.1: Decomposition temperatures or melting points of Hg-rich amalgams $A\mathrm{Hg}_x$ with $x > 3$. Values are taken from[11] if not given otherwise. Congruent melting temperatures are given in slanted numbers.

Composition	Hg/A ratio x	decomposition temperature [°C]
Cs_2Hg_{27}	13.5	12[16]
KHg_{11}	11.0	70[17]
$RbHg_{11}$	11.0	70[17]
$CaHg_{11}$	11.0	84
$SrHg_{11}$	11.0	63[17]
$BaHg_{11}$	11.0	162[17]
$(N(CH_3)_4)Hg_8$	8.0	6[18]
Rb_3Hg_{20}	6.67	132
Cs_3Hg_{20}	6.67	*158*
KHg_6	6.0	170[19]
$BaHg_6$	6.0	*410*
$Ba_{20}Hg_{103}$	5.15	505
$M_{11}Hg_{45}$[1]	4.09	145–720
$PtHg_4$	4.0	$\geq$ *200*[20]
K_7Hg_{31}	4.43	187
Rb_7Hg_{31}	4.43	162
Rb_5Hg_{19}	3.8	193
Cs_5Hg_{19}	3.8	*164*
K_3Hg_{11}	3.67	195
$M_{14}Hg_{51}$[2]	3.64	157–*480*
K_2Hg_7	3.5	202[21]
Rb_2Hg_7	3.5	*197*[21]

[1] Amalgams with the $Sm_{11+x}Cd_{45-x}$ structure type show compositional ranges between $x = 3.79$ (La, $T = 720$ °C) and 4.09 (Gd, $T = 145$) and have been reported for $M =$ La, Ce, Pr, Nd, Sm, Gd and U[22,23].

[2] Amalgams with variants of the $Gd_{14+x}Ag_{51-x}$ structure type show compositional ranges between $x = 4.63$ (Na, $T = 157$ °C) and 5.44 (Sr, $T = 480$ °C) and have been described for $M =$ Na, Ca, Sr, Eu and Yb[22,24,25].

First reports on the employment of amalgams in dental fillings date back to 659 during the Tang dynasty in ancient China[8], in european medical history first evidence of an amalgam fillings after the chinese recipe dates back to the end of 16th century[9]. Despite the slow but constant replacement of amalgams by other dental filling materials[10], many people still rely on amalgam fillings as they are very long-time resistive and the mechanical removal of existing amalgam fill-

ings harbours the risk of unnecessary Hg release. With respect to the vast employment of dental amalgams it is very surprising that new binary Cu–Hg phases can be found. It becomes even close to improbable when taking into account that both mercury and copper are important materials since prehistoric times, the combination of both is employed e.g. in the centuries-old fire gilding process where a copper surface is amalgamated by submerging in a Hg nitrate solution prior to applying gold amalgam and subsequent distillation of the Hg. Despite the widespread and longtime preparation of Cu–Hg phases knowledge hereon is scarce. The published phase diagram[11] shows only one phase, Cu_7Hg_6, and even for this phase there exist concurring structure descriptions, some of them expressing reasonable doubt on the others[12–15]. Details on behaviour of the liquidus curve or thermodynamic stability ranges also remain unclear.

The problem with identifying amalgam phases often lies in their low thermal stability. As Hg has a very low melting point, the liquidus curve in most phase diagrams shows a steep run in the Hg-rich region, and the Hg-richest phases normally show low peritectic decomposition temperatures (see Table 2.1). Standard solid state preparation techniques usually are not suitable to prepare those delicate phases. Thermoanalytic methods can show presence of low-decomposing phases, however, if accompanying structural elucidations are impeded, their exact compositions remain unclear. In addition, thermoanalytic studies can be hampered by kinetic effects which are much more pronounced at low than at high temperatures (seed formation, phase transformations and suchlike). Problems with structural analyses of crystalline amalgams with high Hg content are caused by their high X-ray absorption coefficients. A special case is given for the widely employed Au amalgams which show an especially inconvenient combination of high absorption and especially low X-ray contrast, leading to only very few structurally sufficiently described phases and a rudimentary phase diagram[11].

It now comes clear that with all the named complications a number of new amalgams can be expected to be found even in systems that have been employed technically since a very long time. Both synthesis and structural analysis require non-standard techniques and diligence.

2.1.3 Results

Single crystals of Cu_3Hg were found together with crystals of Cu_7Hg_6 on the surface of an amalgamated copper spoon after 12 days at 90 °C. Both phases form crystals of dark bronze colour when Hg-free, and of bright silver luster when a thin film of Hg covers the surface. Cu_3Hg forms prismatic crystals whereas Cu_7Hg_6 forms platelets. Both amalgams are air-stable at room temperature at least over several weeks. A rod-shaped crystal of Cu_3Hg was selected under a binocular and glued on top of a glass fiber. Data were carefully corrected for considerable absorption effects on the basis of indexed crystal faces. Metric and extinction conditions pointed towards the Ni_3Sn structure type (space group $P6_3/mmc$), and structure solution and refinement showed this to be correct. Crystallographic details and results of the single crystal structure refinement are compiled in Tables 2.2, 2.3, 2.4 and 2.5.

Cu_3Hg crystallises with the Ni_3Sn structure type representing a colouring variant of the hcp packing. The lattice parameter a of the Ni_3Sn structure type is doubled with respect to simple hcp by creating two crystallographic sites with non-equal Wyckoff numbers for Sn (Hg) on $2d$ and Ni (Cu) on $6h$ while retaining the original space group type $P6_3/mmc$. By this colouring, Hg atoms are only coordinated by 12 Cu atoms forming $[HgCu_{12}]$ anticuboctahedra. Cu atoms form streaks of *trans*-facesharing $[Cu_6]$ octahedra (see Figure 2.1). In an alternative picture, the crystal structure can be visualised with plane hexagonal nets at heights $z = 1/4$ and $3/4$ which are stacked along c with...ABAB... periodicity, where A and B are shifted by (1/3, 2/3, 1/2) with respect to each other.

Table 2.2: Crystallographic data and details on single crystal data collection, structure solution and refinement for $Cu_{3.11(4)}Hg_{0.89(4)}$. Data collection was performed at room temperature. All standard deviations are given in parentheses in units of the last digit.

Composition	$Cu_{3.11(4)}Hg_{0.89(4)}$
Crystal system	hexagonal
Space group	$P6_3/mmc$, (No. 194)
Lattice parameters a,c [Å]	5.408(4), 4.390(3)
V [Å^3]	111.18(13)
Z	2
Density (X-ray) [gcm^{-3}]	11.235
Diffractometer	STOE IPDS 1, AgK_α radiation
Absorption coeff. μ [mm^{-1}]	48.62
ϑ range [°]	5.02-23.53
Index range	-7 $\leq h, k \leq$ 7, -6 $\leq l \leq$ 6
No. of collected refl.	2154
No. of independent refl.	72
No. of indep. refl. ($I \geq 2\sigma(I)$)	71
R_{int}	0.2198
R_σ	0.0485
$F(000)$	322.8
Corrections	Lorentz, polarisation, absorption effects
Absorption correction	numerical [44,45]
Structure solution	direct methods [46]
Structure refinement	full-matrix least-squares on F^2 [46]
No. of L.S. parameters	9
GooF	1.180
R values ($I \geq 2\sigma(I)$)	$R1 = 0.0345$, $wR2 = 0.0757$
R values (all data)	$R1 = 0.0368$, $wR2 = 0.0773$
Res. ρ(e$^-$) min/max [e$^-$Å^{-3}]	+1.698/-1.419
Extinction coefficient	0.047(4)

During structure refinement, unusual residual electron densities and weight factors pointed towards possible mixed occupation on the two crystallographic sites. This was tested by independently refining mixed occupations with retaining an overall full occupation of the two sites. The Cu2 site on $6h$ shows no sign of mixed occupation by Hg, whereas there is significant Cu content on the Hg/Cu1 site on $2d$ (see Table 2.13). Refinement of the mixed occupation according to the denotation $Cu_3(Hg_{1-x}Cu_x)$ leads to $x = 0.11(4)$ and the overall refined composition $Cu_{3.11(4)}Hg_{0.89(4)}$. EDX analyses on the crystal specimen used for single crystal X-ray data collection and on two other crystal specimens showed the absence of further metal atoms and a similar composition, however, slightly lower in Cu content. The mean measured composition is $Cu_{2.79}Hg$, see Figure 2.2, calculated: $Cu_{3.49}Hg$. This is somehow surprising as decomposition in high vacuum of the electron microscope can clearly be seen in the crystal picture which would mean evaporation of Hg and therefore a higher Cu content with respect to the results from single crystal refinement.

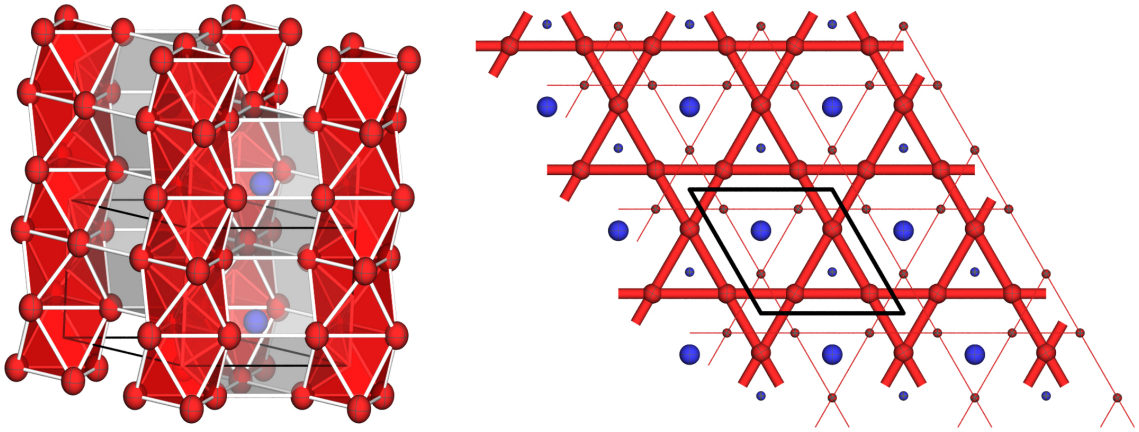

Figure 2.1: Crystal structure of Cu_3Hg with Ni_3Sn structure type. Left: polyhedra packing with blue Hg atoms centering light grey [$HgCU_{12}$] anticuboctahedra and red Cu atoms forming empty *trans*-facesharing [Cu_6] octahedra, *c* pointing upwards. Right: net representation in the *ab* plane at height $z = 1/4$ (fat bonds, large atoms) and $z = 3/4$ (thin bonds, small atoms). Stacking of the nets follows periodicity ...ABAB... along *c* while shifting B versus A by (1/3, 2/3, 1/2) as shown. Ellipsoids are drawn at a probability level of 99% for Cu (red) and Hg (blue).

Table 2.3: Standardised fractional atomic coordinates[47] and equivalent isotropic displacement parameters [$Å^2$] for $Cu_{3.11(4)}Hg_{0.89(4)}$. The equivalent isotropic displacement parameter is defined as 1/3 of the trace of the anisotropic displacement tensor. All standard deviations are given in parentheses in units of the last digit.

Atom	occupation factor	Wyckoff letter	x	y	z	U_{equiv}
Hg1	0.89(5)	2*d*	$\frac{1}{3}$	$\frac{2}{3}$	$\frac{3}{4}$	0.0160(7)
Cu1	0.11(5)	2*d*	$\frac{1}{3}$	$\frac{2}{3}$	$\frac{3}{4}$	0.0160(7)
Cu2	1	6*h*	0.1589(3)	2*x*	$\frac{1}{4}$	0.0201(18)

2.1.4 Discussion

Cu_3Hg in comparison to other amalgams with the Ni_3Sn structure type

All amalgams adopting the Ni_3Sn structure type[26–28] are compiled in Table 2.6. Always the minority component *A* is coordinated only by Hg atoms in an anticuboctahedral environment, and all known examples have the Hg-rich composition MHg_3. This can be seen as an expression of some Coulombic contributions $A^{\delta+}[Hg_3]^{\delta-}$ and formation of coordination spheres of negatively polarised Hg atoms around the cationic species *A*. This is corroborated by the fact that this class of amalgams is only formed by explicitly electropositive metals.

The Ni_3Sn structure type is a favoured sphere packing in amalgams where the atomic radii of *A* do not differ much from the one of Hg (151 pm,[29]). Differences according to Table 2.6 seem only favourable if the *A* metal is larger than Hg. The largest difference can be found for Sr with an

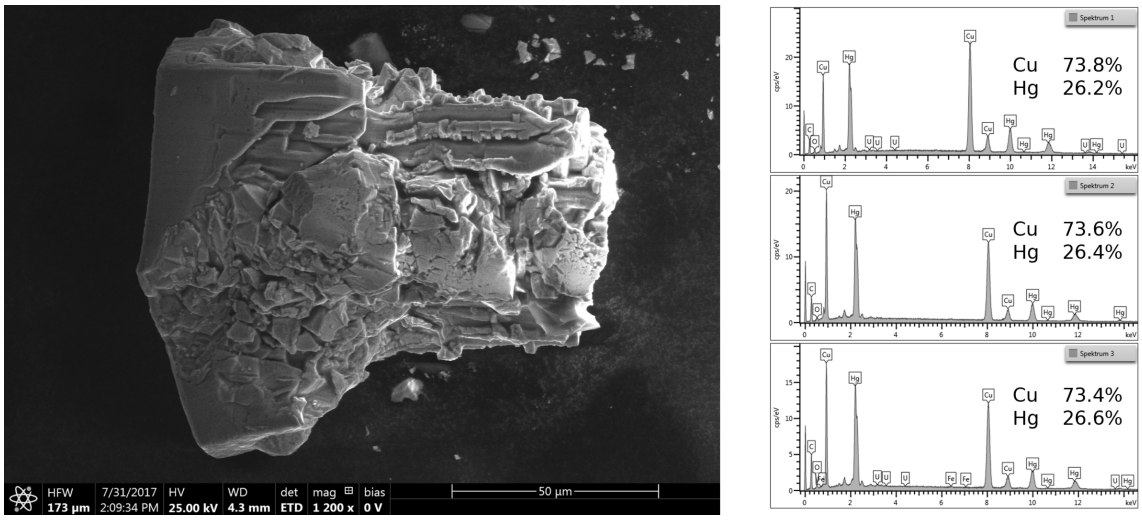

Figure 2.2: Scanning electron micrograph of a Cu_3Hg crystal. Deterioration effects due to high vacuum and electron beam are clearly visible. On the right EDX spectra taken on three different crystals are shown. Cu and Hg contents are given in atomic percent.

Table 2.4: Coefficients of the anisotropic displacement tensor [Å^2] for $Cu_{3.11(4)}Hg_{0.89(4)}$. U_{ij} is defined as $U_{ij} = \exp{-2\pi^2[U_{11}(ha^*)^2 + ... + 2U_{21}hka^*b^*]}$. All standard deviations are given in parentheses in units of the last digit.

Atom	U_{11}	U_{22}	U_{33}	U_{23}	U_{13}	U_{12}
Hg1	0.0156(7)	$= U_{11}$	0.0168(8)	0	0	0.0078(4)
Cu1	0.0156(7)	$= U_{11}$	0.0168(8)	0	0	0.0078(4)
Cu2	0.0195(19)	0.024(2)	0.019(2)	0	0	0.0118(10)

atomic radius 42% larger than the one of Hg. No amalgams are known with A atoms smaller than Hg so far. In addition, it can be stated that all known amalgams of this type show a ratio of the lattice parameters c/a smaller than its ideal value for a packing of incompressible spheres of equal size with all spheres in contact. The ab plane is widened with respect to the stacking of the planes. This distortion cannot be due to only geometrical reasons because the larger A atoms should distort the packing equally in all directions, not only the ab plane. The anticuboctahedral coordination polyhedra [AHg_{12}] thus are oblate with the 6 equatorial Hg atoms having larger distances than the other 6. The variation of the c/a ratio does not follow the quotient of the atomic radii: c/a is largest (and therefore closest to ideal geometric ratio) for $LiHg_3$ (0.768) and for $YbHg_3$ (0.761) while Li and Hg have almost identical atomic radii and Yb is 17% larger than Hg. The smallest c/a ratios are found for $LaHg_3$ (0.729, La being 24% larger than Hg), $CeHg_3$ (0.731, 21%), Th (0.730, 19%) and U (0.735, 3%). Geometric as well as electronic reasons may contribute to the structural distortion, and heteroatomic interactions seem to have higher bonding contributions than homoatomic ones, as suggested by studies on the electronic structure of Ni_3Sn[27]. In the amalgam cases, Coulombic contributions may be the underlying reason, however, the degree of interplay of different contributions still remain speculative. One could assume bonding $Hg^{\delta-}$-$Hg^{\delta-}$ interactions

Table 2.5: Selected interatomar distances in $Cu_{3.11(4)}Hg_{0.89(4)}$ in Å. All standard deviations are given in parentheses in units of the last digit.

Atom 1	Atom 2	distance
Hg1	Cu2	2.7048(19) (6x)
	Cu2	2.736(2) (6x)
Cu2	Cu2	2.578(5) (2x)
	Cu2	2.6521(19) (4x)

to cause a contraction of the [AHg$_{12}$] anticuboctahedra along the 001 direction, as $Hg^{\delta-}$ formally behaves like an early p group metal[32] and tends to form Hg-Hg bonding.

A similar case of deviation from ideal sphere packing geometry is known for elemental mercury. Rhombohedral α-Hg crystallises in a distortion variant of fcc where the individual hexagonal sphere planes are widened with respect to their stacking along the {111} directions of the cubic fcc cell, leading to a rhombohedral metric with $\alpha = 70.44(6)°$[33] instead of 60° for an ideal fcc packing. Band structure calculations show differences in bond strenghts for σ- and π-type interactions between the Hg(p_z) orbitals within and between the hexagonal layers, resulting in the structural distortion of the sphere packing[34].

Table 2.6: Amalgams AHg$_3$ adopting the Ni_3Hg structure type. Hg has an atomic radius of 151 pm[29]. The ideal c/a ratio for hcp is 1.633. Due to a doubling of a, the ideal c/a ratio in the Ni_3Sn structure type is 0.8167. In Ni_3Sn (r_{Ni} = 124 pm, r_{Sn} = 132 pm, ratio r_{Sn}/r_{Ni} = 1.06) the a/c ratio is 0.802[28].

Phase AHg$_3$	r_A [pm]	r_A/r_{Hg}	c/a
LiHg$_3$ [22,35]	152	1.01	0.768
CaHg$_3$ [24]	197	1.30	0.757
SrHg$_3$ [24,36]	215	1.42	0.741
ScHg$_3$ [22,37]	160	1.06	0.748
YHg$_3$ [22,37,38]	181	1.20	0.744
LaHg$_3$ [22,39]	187	1.24	0.729
CeHg$_3$ [40]	182	1.21	0.731
EuHg$_3$ [24]	180	1.19	0.747
GdHg$_3$ [22,41]	180	1.19	0.742
TbHg$_3$ [41]	177	1.17	0.748
DyHg$_3$ [22,41]	178	1.18	0.746
HoHg$_3$ [22,41]	176	1.17	0.747
ErHg$_3$ [22,41]	176	1.17	0.748
TmHg$_3$ [22,41]	176	1.17	0.748
YbHg$_3$ [41]	176	1.17	0.761
LuHg$_3$ [22,41]	174	1.15	0.750
ThHg$_3$ [42]	179	1.19	0.730
UHg$_3$ [43]	156	1.03	0.735

Most interestingly within this context is Cu_3Hg as the first amalgam in this structure type with a reversed composition. In comparison to the other amalgams, Cu_3Hg may be seen as *anti*-Ni_3Sn-type, as it is the only amalgam where the A element constitutes the majority component, and Hg is coordinated in an anticuboctahedron of Cu atoms. The structural deviation from ideal geometry leads to a c/a ratio of 0.812 which is much closer to the ideal value of 0.8167 than for all amalgams with AHg$_3$ composition. Here, the bonding situation is obviously quite different. Obviously, Coulombic interactions cannot play a major role here, as Cu is not a very electropositive metal. This would explain the absence of bonding Hg-Hg contributions and therefore no contraction along c.

While the details of chemical bonding still remain unclear, the inversed composition may as well be explained by geometrical reasons. If the Ni_3Hg structure type demands a structural necessity for

the minority component to be the bigger atom then Cu with atomic radius of 128 pm [29] favours the formation of Cu_3Hg with a quotient $r_{Hg}/r_{Cu} = 1.18$ over the formation of $CuHg_3$ with a quotient of $r_{Cu}/r_{Hg} = 0.878$. If the atomic radii really play a decisive over the formation of amalgams of the Ni_3Sn structure type with a composition A_3Hg, then the respective amalgams should also be found for A = Cr (r = 128 pm), Mn (r = 127 pm), Fe (r = 126 pm), Co (r = 125 pm) and Ni (r = 124 pm). As from these elements only Mn and Ni are known to form amalgams and as from these no amalgam with composition A_3Hg is known so far, we consider it worthwhile to have a closer look on the respective binary phase diagrams in the near future.

2.1.5 Notes on the crystal structure of Cu_7Hg_6

The Hg-richer amalgam Cu_7Hg_6 was the only structurally described Cu amalgam so far. It was first described as a member of the rhombohedral γ-brass-type structures [12] in 1969. Later on, its natural occurence as mineral Belendorffite was revealed [13]. In rhombohedral setting, the rhombohedral angle α of its unit cell is 90.4°, and it may be due to the consequent pseudocubic twinning that also a cubic mineral Kolymite with identical composition can be found in literature [14]. It is most probable that both minerals are actually the same; strikingly the space group of Kolymite, $I\bar{4}3m$, is a direct supergroup of the space group $R3m$ of Belendorffite, as would be expected for either a reversible temperature-driven phase transition of higher order or an overlooked twinning problem.

At close sight, also the rhombohedral γ-brass-type structure in $R3m$ has severe flaws: it has already been pointed out [15] that single crystals of this phase showed the right metric (a = 13.36 Å, c = 8.08 Å in hexagonal setting) but the extinction conditions for a rhombohedral centering (hkl only observed for $-h+k+l = 3n$) are violated, pointing rather to a primitive trigonal lattice. We have performed X-ray single-crystal studies on several specimens of Cu_7Hg_6 single crystals, however, we cannot give a conclusive structure model for this phase at the moment. As the amalgam is air-stable, the specimens were glued on a glass fiber and centered on a diffractometer system with MoKα radiation (Bruker D8 Venture with rotating anode, Bruker AXS, Karlsruhe, Germany). In all studied cases, the diffraction patterns suffered from low intensity, high background and a rapid drop of Bragg intensities with ϑ. This can also be seen in a powder diffraction pattern recorded in MoKα radiation (parafocussing Debye-Scherrer geometry, see Figure 2.4). There is an intrinsic reason for this: In the crystal structure of Cu_7Hg_6 there are six crystallographic Cu and three crystallographic Hg sites. Our preliminary studies show mixed occupation Cu/Hg on all positions, in varying degrees. The amount of aperiodically delocalised Hg atoms causes a high diffuse diffraction intensity and lowers the Bragg intensities significantly, also causing the structure factor to decay rapidly with ϑ. Structure solution from intensities resulting from disordered heavy atoms is difficult by itself, but here another problem comes into place. We have observed the same discrepancy between reported R-centered metric and extinction conditions pointing rather to a primitive cell. From one well-diffracting specimen we have collected data of a whole Ewald sphere and calculated the reciprocal lattice sections shown in Figure 2.3. It becomes obvious that

the crystal in question suffers from twinning, causing the observed extinction condition violations. Although the intensity patterns seem to be in accordance with a standard obverse-reverse twinning according to $\begin{pmatrix} -1 & 0 & 0 \\ 0 & -1 & 0 \\ 0 & 0 & 1 \end{pmatrix}$, no reasonable structure model could be derived from these data so far. We believe additional (merohedral) twinning problems to be the reason for this, and crystallographic studies on this intriguing phase are being continued at the moment.

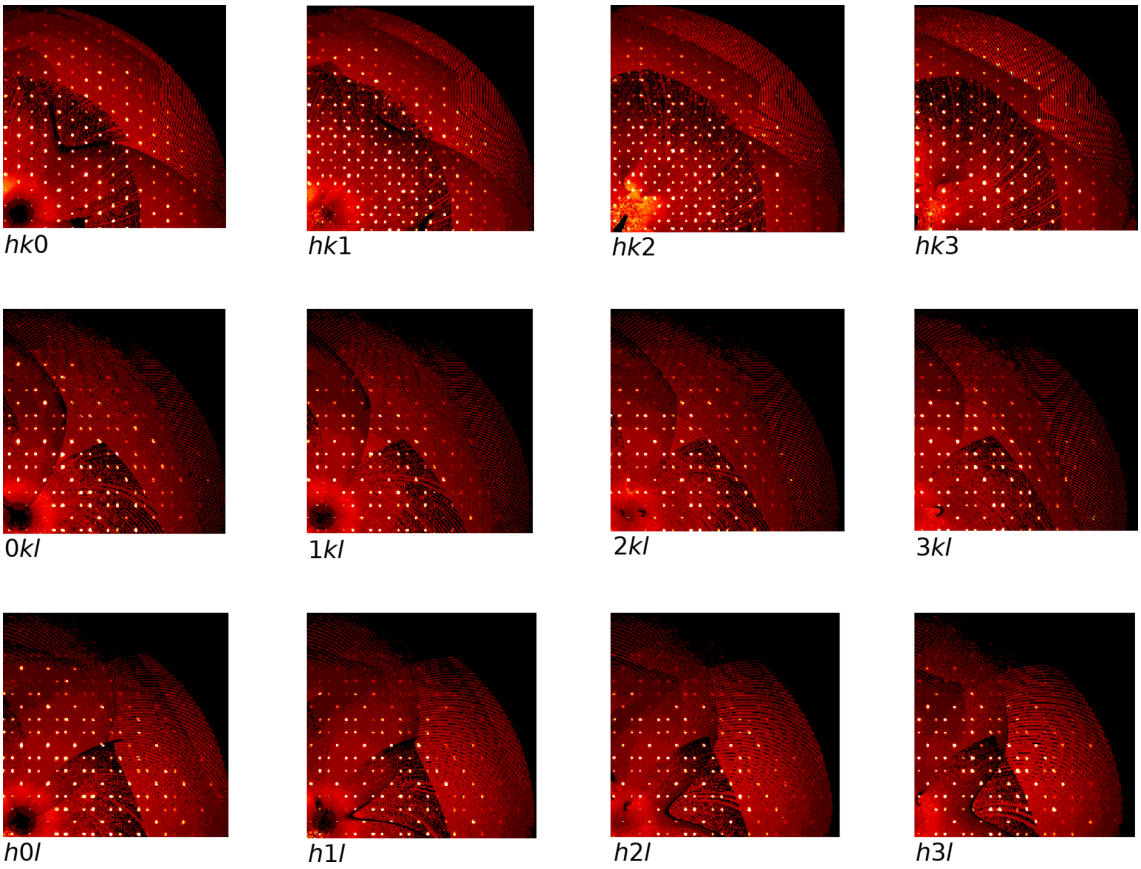

Figure 2.3: Reciprocal lattice sections calculated from a single crystal data collection for Cu_7Hg_6. For clarity, only the right upper quadrants are shown.

2.1.6 Materials and Methods

Synthesis of copper amalgams

We did not inted to prepare copper amalgams. Crystals of Cu_3Hg and Cu_7Hg_6 were the serendipitous results of the attempt to synthesise Hg-rich uranium amalgams by electrocrystallisation, starting from a solution of UI_4 in N,N-Dimethylformamide (DMF) and a reactive cathode consisting of a Hg drop suspended in an amalgamated Cu spoon. The preparative approach to temperature-sensitive Hg-rich amalgams via electrocrystallisation had proven very convenient in previous cases[16,25,48,49]. Electrocrystallisation was performed at 90 °C for two weeks and resulted in the formation of nanocrystalline UO_2 (see Figure 2.4, left), while the Hg drop formed the copper amalgams Cu_3Hg

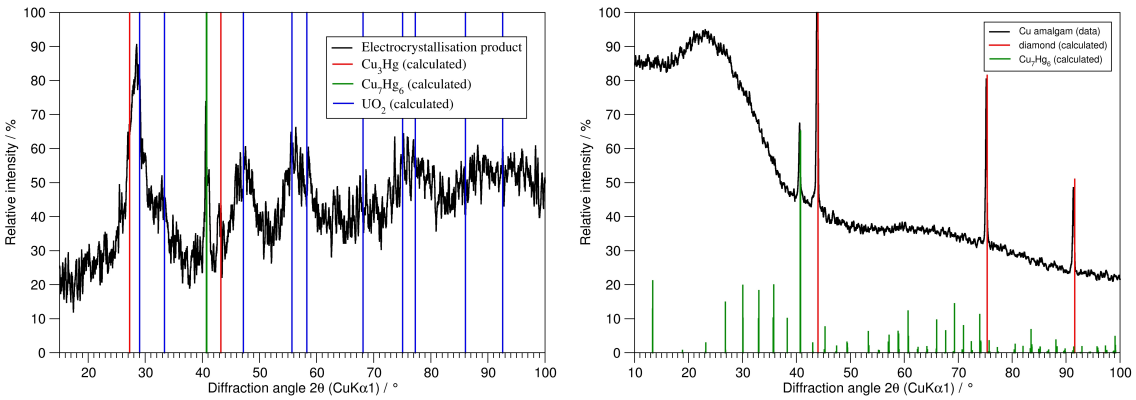

Figure 2.4: Left: Powder diffraction pattern of the electrocrystallisation product. The broad maxima originate from nano-scaled UO_2, the sharp maxima belong to both Cu amalgams Cu_3Hg and Cu_7Hg_6. Right: Powder diffraction pattern of a sample of Cu amalgams. Data collection was performed in parafocussing Debye-Scherrer transmission geometry on a capillary sample diluted with diamons powder.

and Cu_6Hg_7 over the reaction time of two weeks. The reason for the unsuccessful U amalgam synthesis is that UI_4 dissolves in molecular form in DMF, and does not form ionic complexes $[U(DMF)_x]^{4+}$ as other metal iodides do. This has been shown by recording UV-vis spectra of the solutions and comparison with literature.

The reaction of a copper foil with mercury at 105 °C was repeated outside of the electrocrystallisation chamber and also resulted in formation of the Cu amalgams directly from the elements, see Figure 2.4. Both amalgams decompose at temperatures between 110 and 200 °C. By heating the amalgamated copper foil in dynamic vacuum to 200 °C the released mercury is distilled off and a homogeneous copper network with interpenetrating nano-scaled copper rod structures is formed (see Figure 2.5). This copper network with high porosity might be interesting for utilisation in heterogeneous catalysis reactions due to its simple and straightforward preparation.

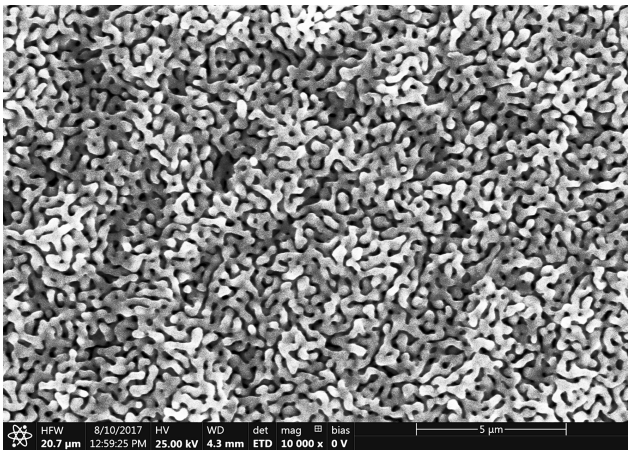

Figure 2.5: Scanning electron micrograph of nano-scaled metallic copper structures, prepared by thermolysis of Cu amalgams at 200 °C in vacuum.

Single crystal investigations

Single crystals of the copper amalgams were selected under a binocular, and specimens with well-shaped faces were glued on top of a glass fiber with cyanacrylate glue. They were centered either on the one-circle goniometer of a diffractometer system IPDS 1 (Stoe & Cie., Darmstadt, Germany)

equipped with graphite-monochromatised Ag-Kα radiation (fine-focus X-ray tube) and imaging plate detector, or on the goniometer of a D8 Venture diffractometer system (Bruker AXS, Karlsruhe, Germany) with fixed-κ geometry, Göbel mirror optics, MoKα radiation (rotating anode) and a Photon II CPAD detector. After checking crystal quality and crystal metrics, data collection was performed in either φ scans (Cu_3Hg, IPDS 1) or combined φ and ω scans (Cu_7Hg_6, D8), in both cases data of the accesible part of an entire Ewald sphere was collected. Data were corrected for Lorentz and polarisation effects with the diffractometer software packages[50,51]. Absorption corrections were performed carefully on the basis of optimised indexed crystal faces (Cu_3Hg[44,45,50]) or on the basis of multiply measured symmetry equivalents (Cu_7Hg_6[51]). Structure solution for Cu_3Hg was performed with direct methods[46] in space group $P6_3/mmc$ as indicated by extinction conditions together with statistics on E^2-1. Structure refinement was performed with full-matrix least-squares cycles[46] on F^2. Both atoms were treated with anisotropic displacement tensors. Further information can be obtained from Fachinformationszentrum Karlsruhe, 76344 Eggenstein-Leopoldshafen, Germany (fax +49 (0)7247 808 666; e-mail: crysdata@fiz-karlsruhe.de; http://www.fiz-informationsdienste.de/en/DB/icsd/depot_anforderung.html) on quoting the deposition number CSD-433425.

Powder diffractometry

For powder diffraction, the amalgam samples were prepared by grinding together with diamond powder for both optical dilution due to high absorption coefficients and mechanical reasons as the amalgams are rather ductile. The powders were sealed in glass capillaries ($\varnothing$ = 0.3 mm) and data collection was performed on a diffractometer system STADI P (Stoe & Cie., Darmstadt, Germany) equipped with Ge-monochromatised MoKα1 radiation and Mythen 2K detector in parafocussing Debye-Scherrer geometry. For better comparison of the recorded diffraction patterns with calculated patterns based on single crystal data from literature, they were converted to Cu-Kα1 wavelength.

2.1.7 EDX spectroscopy

EDX spectra were collected on an electron microscope system JSM-6500F (Jeol, Freising, Germany) with field emission source and EDX detector at 25 kV.

Acknowledgments: We thank Wolfgang Schnick from Ludwig-Maximilians-Universität München for generous funding. We also thank Christian Minke from LMU München for EDX measurements and SEM imaging. Florian Kraus from Philipps-Universität Marburg kindly provided samples of UI_4 for the electro-crystallization experiments.

References

[1] R.Bharti, K. K. Wadhwani, A. P. Tikku, A. Chandra, Dental amalgam: an update. *J. Conserv. Dent.* **2010**, *13*, 204-208, DOI 10.4103/0972-0707.73380.

[2] R. L. Sakaguchi, J. M. Powers, *Craig's Restorative Dental Materials*, 13th Ed., Mosby: St. Louis, Missouri, USA, 2011; ISBN 978-0323081085.

[3] S. Bonsor, G. Pearson, *A clinical guide to applied dental materials.*, 1st Ed., Churchill Livingstone: London, Great Britain, 2012; ISBN 978-0702031588.

[4] R. J. Mitchell, T. Okabe, Setting reactions in dental amalgam. Part 1: Phases and microstructures between one hour and one week. *Crit. Rev. Oral Biol. Med.* **1996**, *7*, 12-22, DOI 10.1177/10454411960070010101.

[5] R. J. Mitchell, T. Okabe, Setting reactions in dental amalgam. Part 2: The kinetics of amalgamation. *Crit. Rev. Oral Biol. Med.* **1996**, *7*, 23-25, DOI 10.1177/10454411960070010201.

[6] D. R. Beech, High copper alloys for dental amalgam. *Int. Dent. J* **1982**, *32*, 240-251.

[7] P. Städtler, Dental amalgam. I: Conventional and non-gamma-2 amalgams. *Int. J. Clin. Pharmacol. Ther. Toxicol.* **1991**, *29*, 161-163.

[8] H. -T. Chu, The use of amalgam as filling material in dentistry in ancient china. *Chinese Med. J.* **1958**, *76*, 553-555.

[9] A. Czarnetzki, S. Ehrhardt, Re-dating the chinese amalgam filling of teeth in europe. *Int. J. Anthropol.* **1990**, *5*, 325-332.

[10] S. M. Newman, Amalgam alternatives: what can compete? *J. Am. Dent. Assoc.* **1991**, *122*, 67-71, DOI 10.14219/jada.archive.1991.0246.

[11] *Binary alloy phase diagrams*; Massalski, T.B., Okamoto H., Subramanian, P.R., Eds.; ASM International: Materials Park, Ohio, USA, 1990; ISBN 978-0871704030.

[12] T. Lindahl, S. Westman, The structure of the rhombohedral gamma brass like phase in the copper-mercury system. *Acta Chem. Scand.* **1969**, *23*, 1181-1190.

[13] H. J. Bernhardt, K. Schmetzer, Belendorffite, a new copper amalgam dimorphous with kolymite. *Neues Jahrb. Mineral. Monatsh.* **1992**, *1992*, 18-21.

[14] E. A. Markova, N. M. Chernitsova, N. M. Borodaev, S. Yu, L. S. Dubakina, O. E. Yushko-Zakharova, The new mineral kolymite, Cu_7Hg_6. *Int. Geol. Rev.* **1982**, *24*, 233-237, DOI 10.1080/00206818209452397.

[15] M. M. Carnasciali, G. A. Costa, Cu_xHg_y: a puzzling compound. *J. Alloys Compd.* **2001**, *317-318*, 491-496, DOI 10.1016/S0925-8388(00)01376-1.

[16] C. Hoch, A. Simon, Cs_2Hg_{27}. the mercury-richest amalgam with close relationship to the Bergman phases. *Z. Anorg. Allg. Chem.* **2008**, *634*, 853-856, DOI 10.1002/zaac.200700535.

[17] E. Biehl, H. J. Deiseroth, Darstellung, Strukturchemie und Magnetismus der Amalgame MHg_{11} (*M*: K, Rb, Ba, Sr). *Z. Anorg. Allg. Chem.* **1999**, *625*, 1073-1080, DOI 10.1002/(SICI)1521-3749(199907)625:7<1073::AID-ZAAC1073>3.0.CO;2-V.

[18] C. Hoch, A. Simon, Tetramethylammoniumamalgam $[N(CH_3)_4]Hg_8$. *Z. Anorg. Allg. Chem.* **2006**, *632*, 2288-2294, DOI 10.1002/zaac.200600163.

[19] F. Tambornino, C. Hoch, Bad metal behaviour in the new Hg-rich amalgam KHg_6 with polar metallic bonding. *J. Alloys Compd.* **2015**, *818*, 299-304, DOI 10.1016/j.jallcom.2014.08.173.

[20] S. K. Lahiri, J. Angilello, M. Natan, Precise lattice parameter determination of $PtHg_4$. *J. Appl. Crystallogr.* **1982**, *15*, 100-101, DOI 10.1107/S0021889882011443.

[21] E. Biehl, H. J. Deiseroth, K_2Hg_7 und Rb_2Hg_7, zwei Vertreter eines neuen Strukturtyps binärer intermetallischer Verbindungen. *Z. Anorg. Allg. Chem.* **1999**, *625*, 1337-1342, DOI 10.1002/(SICI)1521-3749(199908)625:8<1337::AID-ZAAC1337>3.0.CO;2-W.

[22] F. Tambornino, *Electrolytic synthesis and structural chemistry of intermetallic phases with polar metal-metal bonding*; PhD thesis, LMU München, Germany, 2016.

[23] F. Merlo, M. L. Fornasini, Crystal structure of the $R_{11}Hg_{45}$ compounds (R = La, Ce, Pr, Nd, Sm, Gd, U). *J. Less-Common Met.* **1976**, *44*, 259-265, DOI 10.1016/0022-5088(79)90173-5.

[24] A. Iandelli, A. Palenzona, Su alcuni composti intermetallici dell'europio con zinco, cadmio e mercurio. *Atti Accad. Nazl. Lincei, Rend., Classe Sci. Fis. Mat. Nat.* **1964**, *37*, 165-168.

[25] C. Hoch, A. Simon, $Na_{11}Hg_{52}$: Komplexität in einem polaren Metall. *Angew. Chem* **2012**, *124*, 3316-3319, DOI 10.1002/ange.201108064; Hoch, C.; Simon, A. $Na_{11}Hg_{52}$: Complexity in a polar metal. *Angew. Chem. Int. Ed.* **2012**, *51*, 3262-3265, DOI 10.1002/anie.201108064.

[26] P. Rahlfs, Die Kristallstruktur des Ni_3Sn (Mg_3Cd-Typ = Überstruktur der hexagonal dichtesten Kugelpackung). *Metallwirtschaft* **1937**, *16*, 343-345.

[27] A. L. Lyubimtsev, A. I. Baranov, A. Fischer, L. Kloo, B. A. Popovkin, The structures and bonding of Ni_3Sn. *J. Alloys Compd.* **2002**, *340*, 167-172, DOI 10.1016/S0925-8388(02)00047-6.

[28] F. Lihl, H. Krinbauer, Untersuchung binärer metallischer Systeme mit Hilfe des Amalgamverfahrens. Das System Nickel-Zinn. *Monatsh. Chem.* **1955**, *86*, 745-751, DOI 10.1007/BF00902566.

[29] M. Mantina, A. C. Chamberlin, R. Valero, C. J. Cramer, D. G. Truhlar, Consistent van der Waals radii for the whole main group. *J. Phys. Chem.* **2009**, *113*, 5806-5812, DOI: 10.1021/jp8111556

[30] S. Xiahan, D. Kui, Y. Hengqiang, An ordered structure of Cu_3Sn in Cu-Sn alloy investigated by transmission electron microscopy. *J. Alloys Compd.* **2009**, *469*, 129-136, DOI 10.1016/j.jallcom.2008.01.107.

[31] Y. Watanabe, Y. Murakumi, S. Kachi, Martensitic and massive transformations and phase diagram in $Ni_{3-x}M_xSn$ (M = Cu, Mn) alloys. *J. Jap. Inst. Met.* **1981**, *45*m 551-558, DOI 10.2320/jinstmet1952.45.6_551.

[32] J. Köhler, M. -H. Whangbo, Late transition metal anions acting as p-metal elements. *Solid State Sci.* **2008**, *10*, 444-449, DOI 10.1016/j.solidstatesciences.2007.12.001.

[33] C. S. Barrett, The structure of mercury at low temperature. *Acta Crystallogr.* **1957**, *10*, 58-60, DOI 10.1107/S0365110X57000134.

[34] S. Deng, A. Simon, J. Köhler, Supraleitung und chemische Bindung in Quecksilber. *Angew. Chem.* **1998**, *110*, 664-666, DOI 10.1002/(SICI)1521-3757(19980302)110:5<664::AID-ANGE664>3.0.CO;2-8; Deng, S.; Simon, A.; Köhler, J. Superconductivity and chemical bonding in mercury. *Angew. Chem. Int. Ed.* **1998**, *37*, 640-643, DOI 10.1002/(SICI)1521-3773(19980316)37:5<640::AID-ANIE640>3.0.CO;2-G.

[35] E. Zintl, A. Schneider, Röntgenanalyse der Lithium-Amalgame. *Z. Elektrochem. Angew. Phys. Chem.* **1935**, *41*, 771-774, DOI 10.1002/bbpc.19350411105.

[36] G. Bruzzone, F. Merlo, The strontium-mercury system. *J. Less-Common Met.* **1974**, *35*, 153-157. DOI 10.1016/0022-5088(74)90154-4.

[37] G. Bruzzone, A. F. Ruggiero, Struttura di alcuni composti intermetallici dell'ittrio. - I. Composti con Cu, Ag, Au, Zn, Cd, Hg. *Atti Accad. Nazl. Lincei, Rend., Classe Sci. Fis. Mat. Nat.* **1962**, *33*, 312-314.

[38] E. Laube, H. N. Nowotny, Die Kristallstrukturen von ScHg, $ScHg_3$, YCd, YHg und YHg_3. *Monatsh. Chem.* **1963**, *94*, 851-858, DOI 10.1007/BF00902359.

[39] G. Bruzzone, F. Merlo, The lanthanum-mercury system. *J. Less-Common Met.* **1976**, *44*, 259-265, DOI 10.1016/0022-5088(76)90140-5.

[40] G. L. Olcese, Sul comportamento magnetico del cerio nei composti intermetallici. II. I sistemi Ce-Zn, Ce-Cd Ce-Hg. *Atti Accad. Nazl. Lincei, Rend., Classe Sci. Fis. Mat. Nat.* **1963**, *35*, 48-52.

[41] A. Palenzona, MX_3 intermetallic phase of the rare earths with Hg, In, Tl, Pb. *J. Less-Common Met.* **1966**, *10*, 290-292, DOI 10.1016/0022-5088(66)90031-2.

[42] R. Ferro, The crystal structures of $ThHg_3$, $ThIn_3$, $ThTl_3$, $ThSn_3$ and $ThPb_3$. *Acta Crystallogr.* **1958**, *11*, 737-738, DOI 10.1107/S0365110X5800195X.

[43] R. E. Rundle, A. S. Wilson, The structures of some metal compounds of uranium. *Acta Crystallogr.* **1949**, *2*, 148-150, DOI 10.1107/S0365110X49000400.

[44] Stoe & Cie., *X-SHAPE v. 2.07*, Darmstadt, Germany, 2005.

[45] Stoe & Cie., *X-RED v. 1.31*, Darmstadt, Germany, 2005.

[46] G. M. Sheldrick, A short history of SHELX. *Acta Crystallogr.* **2008**, *A64*, 112-122, DOI 10.1107/S0108767307043930.

[47] L. M. Gelato, E. Parthé, Structure Tidy - a computer program to standardize crystal structure data. *J. Appl. Crystallog.* **1987**, *20*, 139-143, DOI 10.1107/S0021889887086965.

[48] F. Tambornino, C. Hoch, The Hg-richest europium amalgam, $Eu_{10}Hg_{55}$. *Z. Anorg. Allg. Chem.* **2015**, *641*, 537-542, DOI 10.1002/zaac.201400561.

[49] F. Tambornino, J. Sappl, F. Pultar, T. M. Cong, S. Hübner, T. Giftthaler, C. Hoch, Electrocrystallization - a synthetic method for intermetallic phases with polar metal-metal bonding. *Inorg. Chem.* **2016**, *55*, 11551-11559, DOI 10.1021/acs.inorgchem.6b02068.

[50] Stoe & Cie., *X-AREA v. 1.39*, Darmstadt, Germany, 2006.

[51] Bruker AXS, *APEX 3 v. 2016.5-0*, Karlsruhe, Germany, 2016.

2.2 Facile One-Step Syntheses of Several Complex Ionic Lithium Gallates from LiGa as Intermetallic Precursor

Jonathan Sappl, Felix Jung and Constantin Hoch

Department Chemie, Ludwig-Maximilians-Universität München, Butenandtstraße 5-13 (D), D-81377 München, Germany, Phone: +49 (0)89 2180-77421, Fax: +49 (0)89 2180-77440

published in: *Chem. Mater.* **32** (2020) 866-873. DOI: 10.1021/acs.chemmater.9b04540.

2.2.1 Abstract

We have employed the intermetallic phase LiGa as a precursor for the preparation of $LiGaO_2$, $LiGaS_2$, $LiGa_5O_8$ and Li_3GaN_2, presenting a new and convenient way to synthesize these compounds. They have high potential for application in optical and electrochemical devices, but their reported standard syntheses require sophisticated high-temperature solid-state preparation methods. With LiGa-based precursor routes, oxo-, thio- and nitridogallates can be obtained in simple one-step reactions at comparatively mild conditions. $LiGaO_2$ and $LiGaS_2$ were revisited in terms of crystal structure, ion conductivity and calculated electronic structure. $LiGa_5O_8$ and Li_3GaN_2 were found as byproducts and are of potential interest for applications themselves. The use of intermetallic phases as precursor materials is in general a valuable yet widely underestimated pathway for simple preparative access to functional materials.

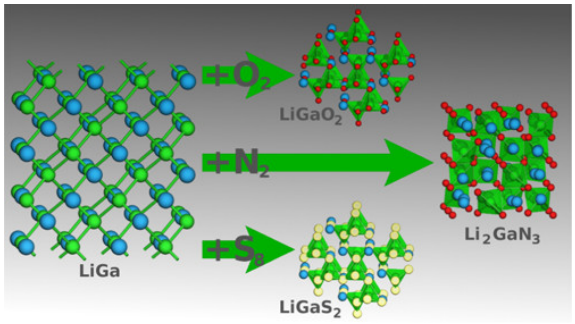

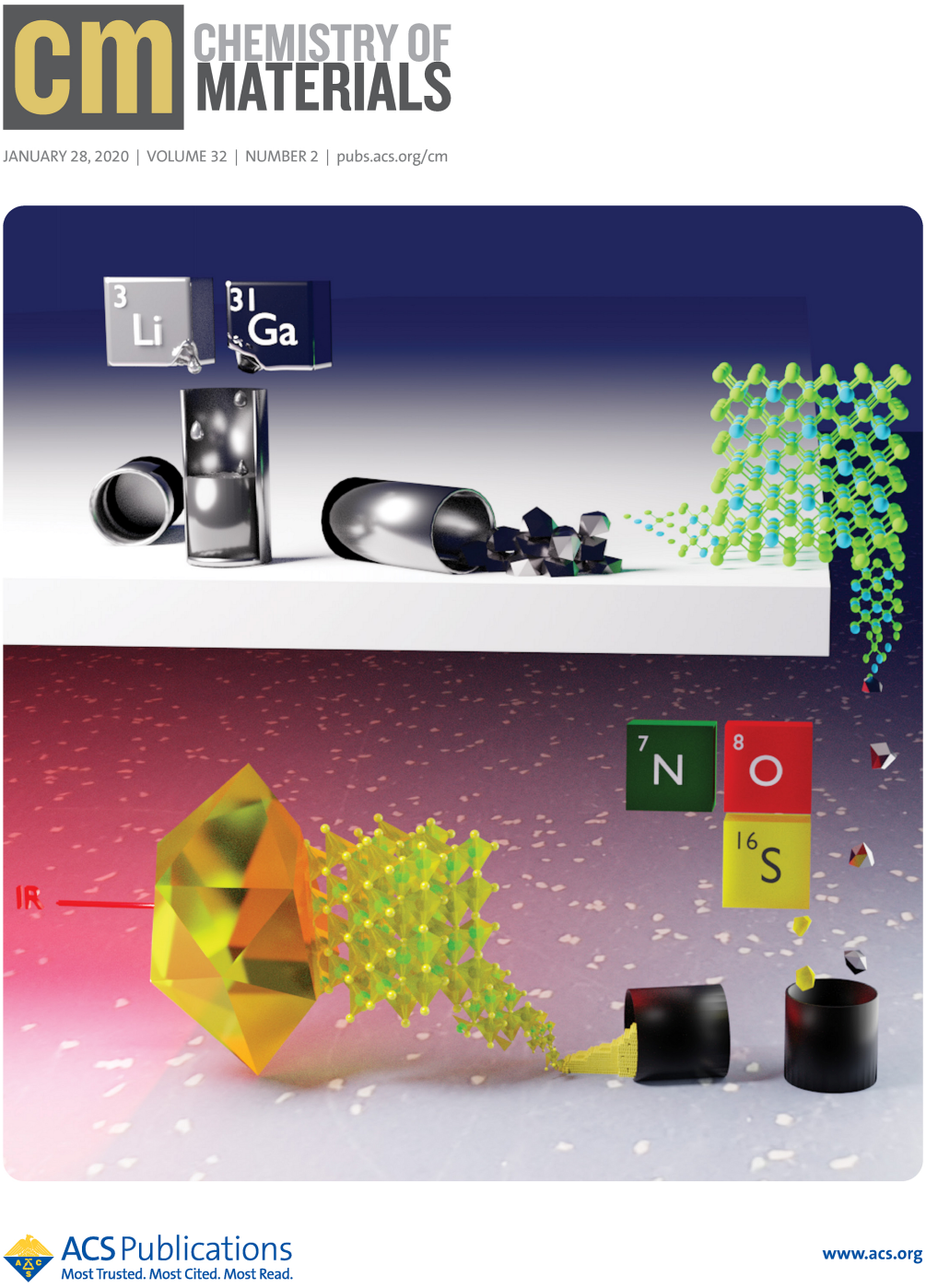

Figure 2.6: Illustrated cover in Chemistry of Materials based on the publication: Facile one-step syntheses of several complex ionic lithium gallates from LiGa as intermetallic precursor.

2.2.2 Introduction

Modern materials science is not only concerned with the search for new high performance materials. Simplification and improvement of synthesis protocols for well-known materials is likewise of crucial importance. As an example, ternary oxidic materials can be prepared by solid state reaction of the binary oxides, however, this affords long reaction times and high temperatures. Other, more modern synthetic approaches consist in combustion syntheses, sol-gel methods, precipitation from homogeneous solution, or reactive precursor routes. They all have in common that the required reaction temperatures are lower and the reactions are much faster. This is realized by adding enthalpic processes (combustion and precursor routes) and/or by reducing the diffusion lengths (sol-gel and precipitation routes). The precursor routes include many different synthetic strategies. Starting compounds can be thermodynamically metastable modifications, gas-evolving compounds, or any compound that shows a decomposition reaction at synthesis comditions. Also phase transitions may be regarded as exothermic and irreversible decompositions within this context. This decomposition helps shifting the equilibrium towards product formation and also adds extra reaction enthalpy.

The employment of intermetallic phases as reactive precursors, however obvious and universal, is comparatively rarely used. Some materials which have come into focus recently strike the eye of intermetallic chemists in this respect, as the included metal atoms and their stoichiometric ratios directly point towards reactive intermetallic phases which consequently could be employed as precursors for the respective syntheses. A look into the current literature reveals for example structures with multiple metallic cations and sulfide anions to be promising optical materials. Recently, new infrared nonlinear optical materials with composition AHgSnQ_4; A = Sr, Ba; Q = S, Se; have been reported on, which are of high interest in the field of laser technology.[1] Here, the amalgams AHg are available and highly reactive,[2–4] Hg and Sn form a homogeneous liquid 1:1 mixture above ca. 150 °C,[5] and also the binary ASn Zintl compounds are available and highly reactive.[6,7] Even the ternary AHgSn compounds are known[8] and could be taken directly for a reaction with sulfur or selenium. Another example is $AgGaGeS_4$, again a promising nonlinear optical material for frequency-shifting of lasers to mid-IR.[9] The compounds AgGa[10] and Ag_2Ga[11] are available and could be taken as a basis for precursor-based reactions. Of course there are many examples for interesting materials apart from optical applications which could be prepared starting from fitting intermetallics, but this has only scarcely be done. One of the reported examples for successful empolyment of an intermetallic precursor with high complexity is the preparation of the luminescent material $Sr_{0.99}Eu_{0.01}AlSiN_3$ based on $Sr_{0.992}Eu_{0.008}(Al_{0.5},Si_{0.5})_2$ as a precursor.[12]

From the high reactivities of intermetallic phases occuring within our recent studies on the Li–Ga system[13], application of the respective binary phases as intermetallic precursors stood to reason. We focused especially on LiGa because the 1:1 ratio of Li and Ga can be used as a basis for a number of compounds, see Table 2.7. Some of them are in discussion or already in use as optical or electrofunctional materials.

Table 2.7: Ternary compounds $LiGaX_n$ containing Li and Ga in a ratio of 1:1. All of them can in principle be obtained by reacting LiGa with elemental *X*. Li_3GaN_2,[14,15] the only known ternary Li- and Ga-containing nitride, is not listed here because of the ratio 3:1.

Chalcogenides	Halides	Intermetallics	Other
$LiGaO_2$[16]	$LiGaCl_3$[17]	$LiGaMg_2$[18]	$LiGaH_4$[19]
$LiGaS_2$[20]	$LiGaCl_4$[21]	LiGaSi[22]	
$LiGaSe_2$[23]	$LiGaBr_3$[24]	$LiGaSi_{0.8}$[22]	
$LiGaTe_2$[25]	$LiGaBr_4$[24]	LiGaGe[26]	
	$LiGaI_3$[17]	$LiGaAg_2$[27]	
	$LiGaI_4$[17]	LiGaPd[28]	
		LiGaPt[28]	
		LiGaIr[28]	

The simple intermetallic phase LiGa was first reported by Zintl and Brauer in 1933.[29] It is isostructural to NaTl, and like this it behaves as a metal and is best described as an ordered variant of a bcc packing and not as a Zintl phase with electron transfer according to Li^+Ga^- as many textbooks do. Topologically, the crystal structure can be described alternatively as two interpenetrating diamond networks, one formed by Ga and the other by Li atoms. In Figure 2.7 both the diamond network and the bcc substructure are indicated, by green Ga–Ga bonds and by a bcc subcell in red, respectively. LiGa is highly reactive under oxidizing conditions, hence our investigations were focused on the formation of ternary oxides, sulfides and nitrides starting from LiGa. The lithium gallate $LiGaO_2$ with 1:1 ratio of Li and Ga was introduced by Marezio in 1965.[16] It was first obtained from a high-temperature solid state reaction of Li_2CO_3 and Ga_2O_3. The hereby obtained wurtzite-analogous polymorph was adressed as β-$LiGaO_2$. It was topic of numerous studies on optical and piezoelectric studies due to its polar space group symmetry (β-$NaFeO_2$ type, space group $Pna2_1$). Subsequently, several high-pressure modifications were discovered: hexagonal α-$LiGaO_2$ (space group $R\bar{3}m$, Delafossite structure type)[30], tetragonal γ-$LiGaO_2$ (space group $I4/m$, $FeLiO_2$ structure type)[31] and cubic δ-$LiGaO_2$ (space group $Fm\bar{3}m$, NaCl structure type with statistical Ga/Li disorder)[31]. With a reported band gap of 5 eV, β-$LiGaO_2$ is a high band gap representative of the class of I-III-VI_2 semiconductors.[32] Applications for $LiGaO_2$ in discussion include substrates for the epitaxial growth of nonpolar GaN and ZnO[33,34], or piezoelectric (due to its polar space group symmetry and high electromechanical coupling constant)[35] and optoelectronic applications[36,37]. It has also been mentioned that lithium gallate itself could serve as a solid-state precursor for the formation of highly crystalline GaN by metathesis under high N_2 pressure.[38] $LiGaS_2$ was first mentioned in 1947 as $Li_2[Ga_2S_4]$, but no structural data were given.[39] Its crystal structure type belongs to the family of wurtzite ordered variants as does the structure of the isostructural β-$LiGaO_2$, and lattice parameters were reported by Hoppe in 1965.[40] The first precise structural study was conducted by Leal-Gonzalez, preparing $LiGaS_2$ by heating an equimolar mixture of gallium oxide and lithium carbonate in a stream of purified dry hydrogen sulfide gas – a highly challenging preparation method.[20] Large single-crystals of $LiGaS_2$ are prepared through the Bridgman-Stockbarger technique with mixtures of elemental Li, Ga, and S in a glassy carbon crucible in a sealed silica ampoule filled with argon. Although this technique works quite well,

high reaction temperatures are required, and the resulting high sulfur gas pressure may rupture the sealed ampoules and thus necessitates careful handling, as stated by the authors.[41] The availability of large single crystals enabled optical measurements. $LiGaS_2$ is reported to form optically negative biaxial crystals, with an average index of refraction of 2.1 in the IR region and transparency ranges at a level of 5 cm^{-1} of 0.32-11.6 μm.[25] With these properties, $LiGaS_2$ is a promising material for direct down-conversion of laser wavelengths to mid-IR.[42] $LiGaO_2$ and $LiGaS_2$ are two prominent examples for lithium- and gallium-containing materials with high applicational interest. Their reported preparations, however, are challenging, time- and energy-consuming and require high safety precautions. We show how simple syntheses at comparatively low temperatures can be realized with LiGa as an intermetallic precursor. We have focused on the preparation of $LiGaO_2$ and $LiGaS_2$ but also studied the formation of the spinel phase $LiGa_5O_8$ and the nitrides Li_3GaN_2 and GaN.

2.2.3 Results and discussion

LiGa as a precursor

LiGa crystallizes with the NaTl structure type in a cubic metric with space group $Fd\overline{3}m$ (no. 227, a = 6.207(7) Å).[29] It is reported that LiGa shows a phase width,[5] leading to small deviations in the lattice parameter. Starting from the elements sealed in tantalum ampoules under inert gas, LiGa can easily be prepared as it melts congruently. Different batches of LiGa were used in the further described precursor syntheses, and they differed slightly in lattice parameters (e. g. see Figure 2.8, batch A: a = 6.2050(1) Å; batch B: a = 6.2344(3) Å, lattice parameters refined from powder XRD data). We conducted ICP-OES (inductively coupled plasma optical emission spectrometry) measurements that showed lithium contents of 50.4 mol-% (batch A) and 55.8 mol-% (batch B), respectively. As the metallic radii of Ga and Li differ with Ga_{rm} = 1.441 Å and Li_{rm} = 1.564 Å.[43], a slight excess of Li in batch B explains the larger unit cell parameter and is probably due to weighing uncertainties at sample preparation. Although the individual precursor batches exhibit these differences in lattice parameters and composition, the formed products ($LiGaO_2$ as well as $LiGaS_2$) were obtained identically and independent of the chosen precursor batch, as deducted from lattice parameter and occupation factor refinement. This is in good agreement with expectations since their ionic structure would not allow for a phase width. Excess Li in the precursor can be expected to react with the crucible material (corundum) used in oxidation or sulfurization reactions and was never observed in a byphase (e. g. $LiCO_3$ or Li_2S) in the X-ray powder diagrams. The reaction products can thus be obtained as phase-pure materials on a powder XRD basis, independent of the exact composition of the precursor.

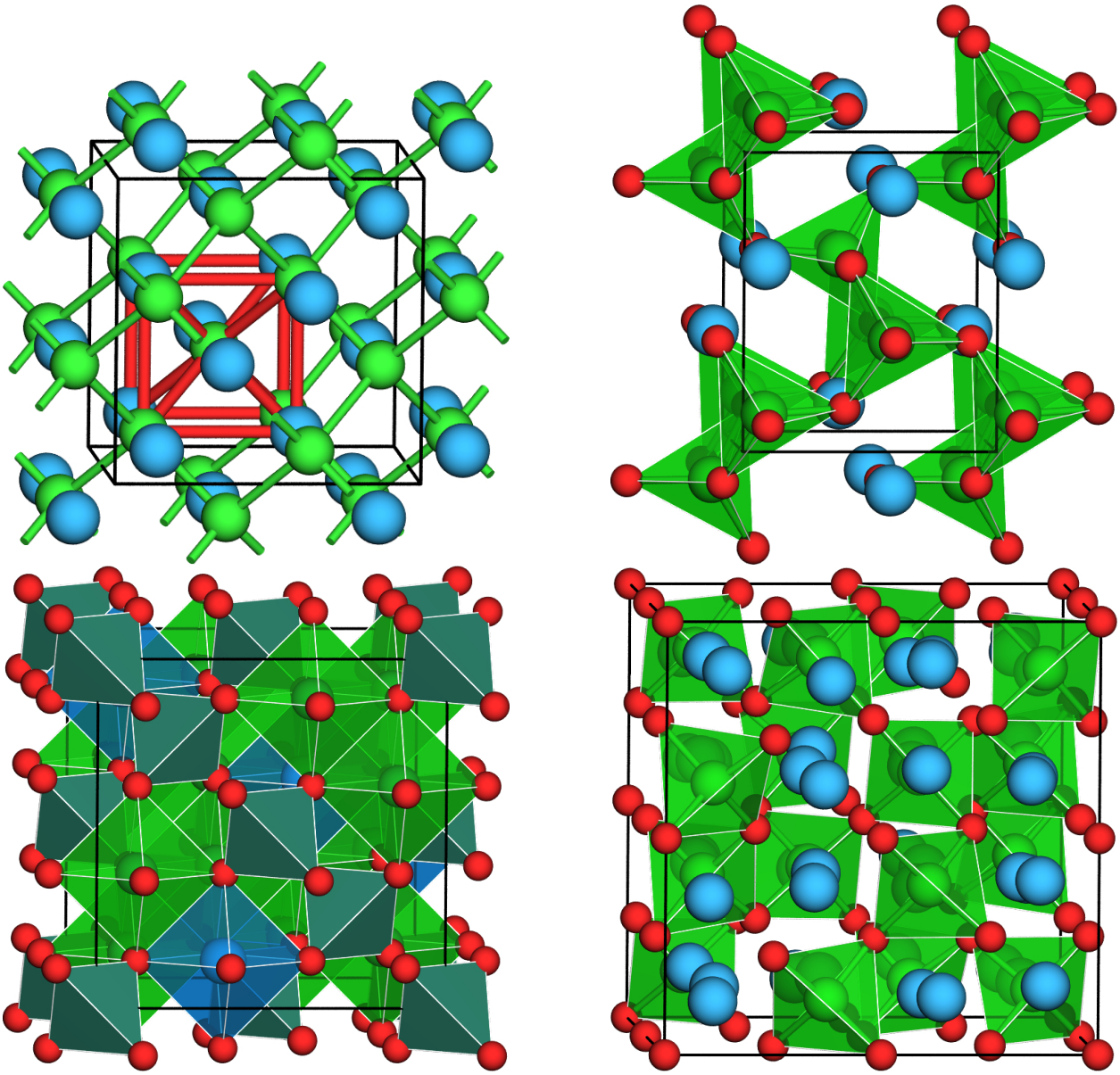

Figure 2.7: Crystal structures of LiGa (upper left) $LiGaO_2$ and the isotypical $LiGaS_2$ (upper right), $LiGa_5O_8$ (lower left) and Li_3GaN_2 (lower right). Li atoms in blue, Ga atoms in green, O, S and N atoms in red. $[GaX_4]$ coordination polyhedra are drawn in light green. For LiGa, both the diamond-like Ga network and the colored bcc topology have been emphasized. For $LiGa_5O_8$ $[GaO_4]$ tetrahedra are drawn as dark green, $[GaO_6]$ octahedra as transparent light green and $[LiO_6]$ octahedra as transparent blue polyhedra.

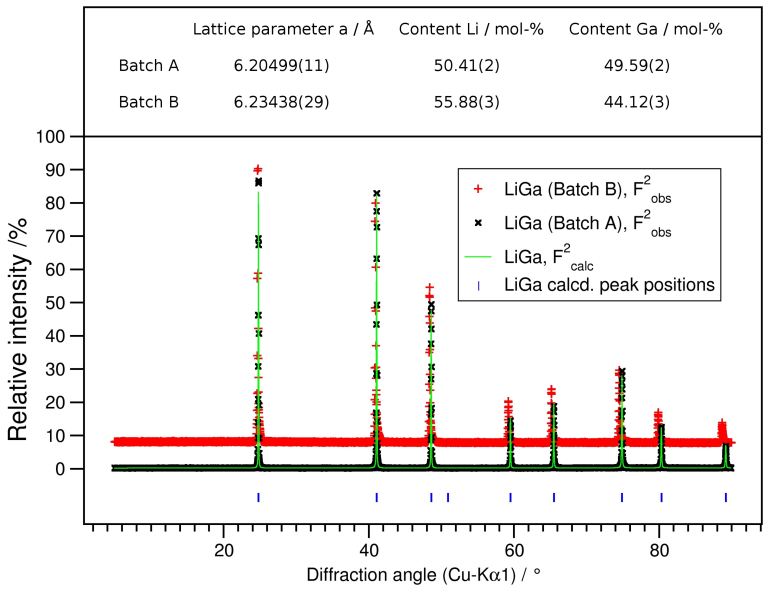

Figure 2.8: Graphical results of Rietveld refinements of two batches of LiGa. At high diffraction angle shifts of the peak positions become obvious, pointing to a larger unit cell parameter *a* for LiGa in batch B. The refined lattice parameters and ICP-OES analysis results are given in the inset above.

$LiGaS_2$ and $LiGaO_2$

By mixing LiGa and sulfur in a glassy carbon crucible and heating to 800 °C for 24 h in an evacuated quartz ampoule, pure $LiGaS_2$ was obtained (Figure 2.11). $LiGaS_2$ has originally been reported as brown-red crystals[20], however, we interpret this color as being caused by a small amount of impurities, probably polysulfides, since later reports applying improved synthesis protocols described the obtained product as light yellow in color[44]. Our product was obtained as an off-white powder, which can be taken as an optical indicator for purity. $LiGaS_2$ is known to crystallize in orthorhombic metric with space group $Pna2_1$ (no. 33, a = 6.519(6) Å, b = 7.872(7) Å, c = 6.238(4) Å).[20] Based on Rietveld refinement, the lattice parameters of our product were determined to be a = 6.51384(12) Å, b = 7.86316(15) Å, c = 6.21786(12) Å (for further details see Table 2.8), which is very close to the reported values. The crystal structure can be described as a hexagonal closest packing of S atoms with one half of the tetrahedral voids occupied by Ga and the other half occupied by Li, see Figure 2.7. Band gaps reported for $LiGaS_2$ in literature differ quite significantly. In 2009, a calculated band gap of 3.28 eV and a measured band gap of 4.15 eV were reported,[45] while previous transmission measurements state values of 3.76 eV[44] or 3.62 eV (based on measurements and extrapolation, respectively).[46] Our own DFT calculations applying modified Becke-Johnson potentials yielded a value of $E_g \geq$ 4.2 eV for the direct band gap in the center of the first Brillouin zone (Γ point), see Figure 2.10. Although $LiGaS_2$ is quite well reviewed with respect to optical properties due to the non-centrosymmetric space group, only few studies are available with respect to its ion conductivity. We therefore conducted electrochemical impedance spectroscopy at room temperature on samples of $LiGaS_2$ prepared by the above mentioned route. As expected, the measured conductivity of σ

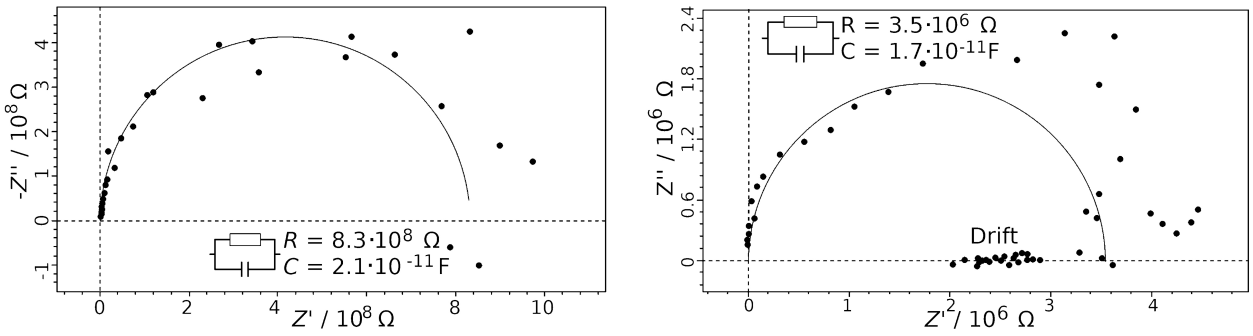

Figure 2.9: Nyquist plots of the electrochemical impedance spectroscopy measurements on $LiGaO_2$ (left) and $LiGaS_2$ (right) powder pellets. The data points were fitted with a parallel setting of resistance and capacitor. With $\sigma = \frac{d}{AR}$ (d = electrode distance, A = powder pellet surface, R = resistance) conductivities of about $5{\cdot}10^{-8}$ and $3{\cdot}10^{-7}$ S·cm^{-1} were calculated for $LiGaO_2$ and $LiGaS_2$, respectively.

$= 3.1 \cdot 10^{-7}$ S cm^{-1} is rather poor (see Figure 2.9). Lithium thiometalates are a highly vivid research field today with respect to solid state electrolytes, and the materials with the highest ion conductivities (e. g. 12 mS·cm^{-1} for $Li_{10}GeP_2S_{12}$)[46] belong to this class of Wurtzite-related sulfidic materials.[48,49] The relatively modest properties of $LiGaS_2$ with this respect may be considerably enhanced by introducing defects. These can be created by substitution of Ga^{3+} by Ge^{4+}, as both mixed crystal series $LiGa_{1-x}Ge_x$ and the stoichiometric compound LiGaGe exist and can easily be prepared either from the elements or from LiGa by reaction with Ge. First orientating experiments for the synthesis of LiGaGe from LiGa have been performed. It has been found that in a region of 0.1 to about max. 10 at.-% Ge a mixed crystal series $LiGa_{1-x}Ge_x$ isostructural to LiGa with statistical Ga/Ge disorder can be obtained, however, when weighing equimolar LiGa:Ge ratios an ordered variant with lowered symmetry occurs (rhombohedral, space group $P6_2mc$, own structure type).[26] LiGaGe may then be further utilized as a new precursor as described above. Using LiGa as a precursor for $LiGaS_2$ without optimising ion conducting properties by including Ge allows to obtain phase pure $LiGaS_2$ powder samples in gram scale and in comparatively short time, which then can further be processed. The Bridgman-Stockbarger technique stated above to be suitable for the production of single crystals has severe safety issues when starting from the elements Li, Ga and S due to pressure build-up. Starting from pure $LiGaS_2$ powder would resolve the safety issues. The powder may be produced in large batches, can be stored and handled in air. With further optimized synthesis parameters, reduction of the reaction temperature to lower costs and time of the process seems feasible.

$LiGaO_2$ is known to crystallize isotypically to $LiGaS_2$ (space group $Pna2_1$, β-$NaFeO_2$ structure type) with the lattice parameters a = 5.402(1) Å, b = 6.372(1) Å and c = 5.007(1) Å.[16] The lattice parameters obtained from Rietveld refinement for our samples are very close: a = 5.40247(7) Å, b = 6.37374(8) Å, c = 5.00859(6) (for further details see Table 2.8). The oxidation reaction in air took several days to complete. When oxidizing LiGa for a shorter period, the samples may contain minor amounts of byphases such as $LiGa_5O_8$ (see below). Electrochemical impedance spectroscopy

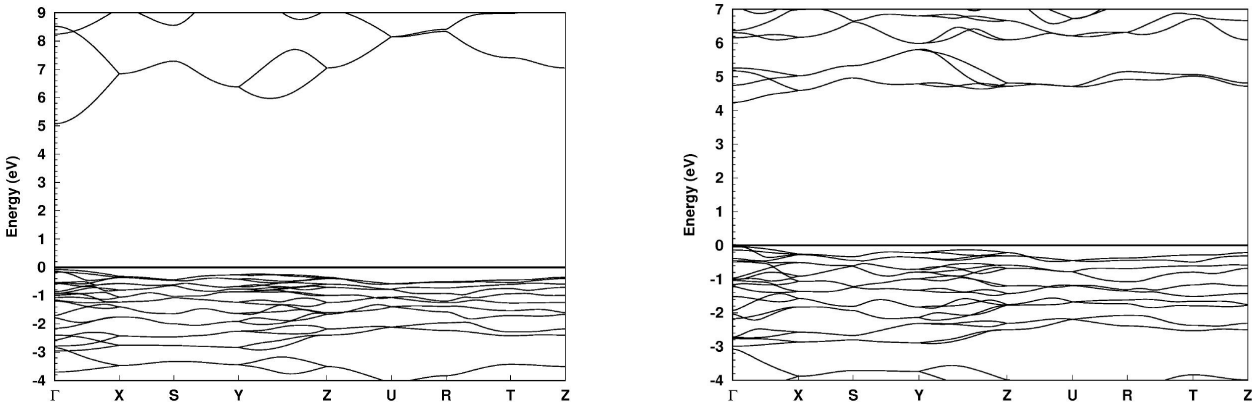

Figure 2.10: Band structures calculated for $LiGaO_2$ (left) and $LiGaS_2$ (right). DFT calculations have been performed wih modified Becke-Johnson potentials for a more realistic modelling of the band gap.

on pure $LiGaO_2$ samples shows an ion conductivity of $\sigma = 5 \cdot 10^{-8}$ S cm^{-1} (see Figure 2.9). All measurements were conducted at room temperature. As expected, the ion conductivity is lower than for $LiGaS_2$, and the electronic contribution to the overall conductivity is small with ca. 18%, as expected for a high-band gap material. As stated above for $LiGaS_2$, improving the ion conductivity may be achieved by defect creation using LiGaGe instead of LiGa as precursor material. The band gap of lithium gallate was first reported to be 5 eV[32] (unclear whether calculated or measured) and was later calculated to be 3.2 eV[50] or 5.6 eV[51]. Our own DFT calculations resulted in a direct band gap of 5.1 eV, see Figure 2.10, with the lowest band above E_F at the Γ point having *s* character. The flat bands below E_F show the typical signature for a solid with high covalent bonding contributions. In 2014, the optical band gap energy of a $LiGaO_2$ single crystal was found to be 5.26 eV,[52] in very good agreement with our DFT calculations. In general, the band gap of an oxide should be higher than that of a sulfide of the same structure type, and comparison of the reported band gap of 5.26 eV ($LiGaO_2$) to the one of $LiGaS_2$ (4.15 eV, 3.76 eV or 3.62 eV) as well as the ones from our DFT calculations shows this condition to be fulfilled. It is also clearly visible from the DFT calculations how the bands in an isostructural sulfide overall are much flatter then for the respective oxide. $LiGaO_2$ is usually produced by using Li_2CO_3 and Ga_2O_3 powders in a solid state reaction, employing a small excess of Li_2CO_3 to compensate for losses due to evaporation. The reaction temperature is reported to be 1200 °C.[52] Using LiGa as a precursor allows for a significant reduction in reaction temperature and guarantees full conversion of the reactant. The colorless powder is stable in air and may be used as starting material for the Czochralski method to gain large single crystals.

$LiGa_5O_8$

During explorative optimization of $LiGaO_2$ synthesis parameters, the formation of $LiGa_5O_8$ as a byproduct was observed for shorter exposition of LiGa to air (see Figure 2.11). This spinel-type phase also is of interest regarding ion conductivity. $LiGa_5O_8$ was first reported on in 1963.[53] Its

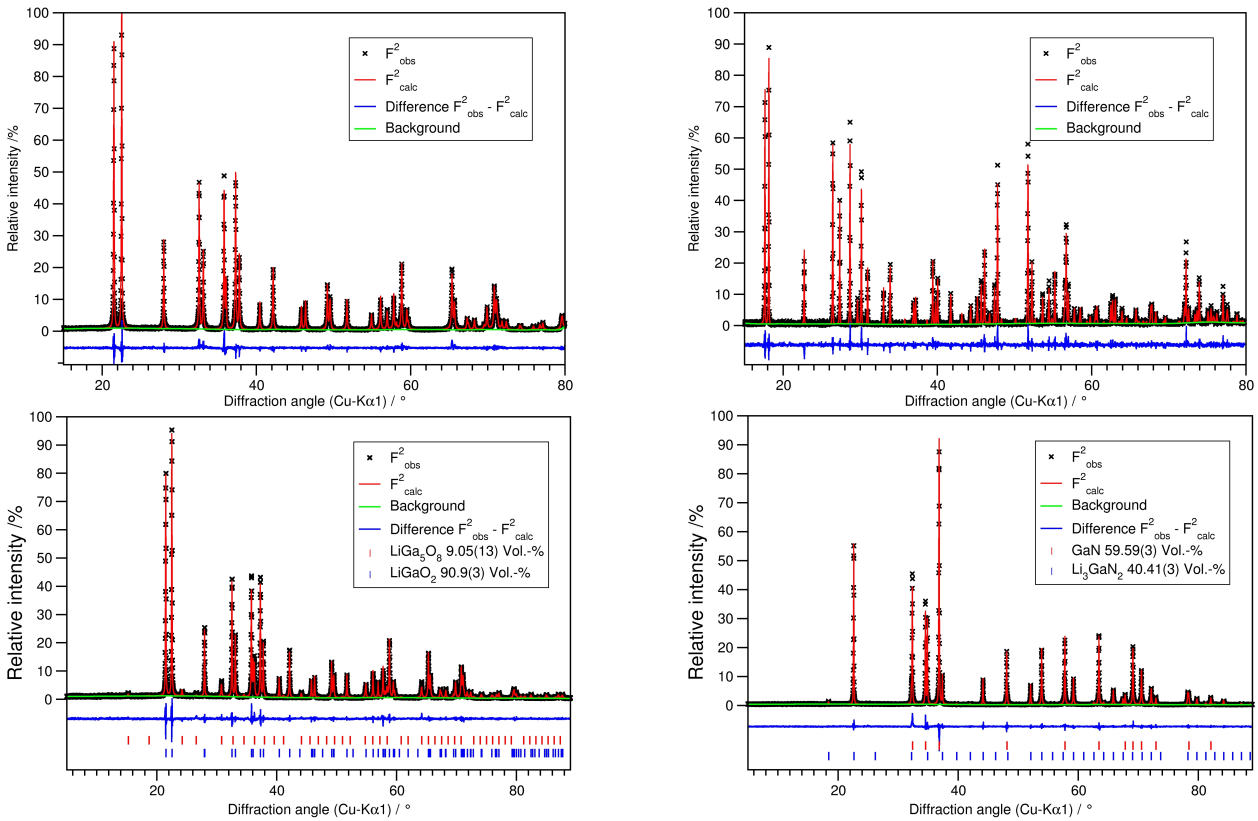

Figure 2.11: Graphical results of Rietveld refinements of $LiGaO_2$ (upper left) and $LiGaS_2$ samples (upper right), of a sample of $LiGaO_2$ containing about 9% of the spinel phase $LiGa_5O_8$ (lower left) and of a nitrification product mixture of GaN and Li_3GaN_2 in a 3:2 ratio (lower right). Further detail is given in Table 2.8.

crystal structure is an ordered variant of the spinel type according to the notation $(LiGa)Ga_4O_8$ with Li on octahedral and Ga both on tetrahedral and octahedral positions, see Figure 2.7. The importance of spinels as rigid and temperature-stable host lattices for electroactive materials has often been stated,[54,55] and spinels have been the basis of intensive research on new electroactive materials for many years. $LiGa_5O_8$ is a promising candidate for solid state electrolytes or, by exchange of Ga for a redox-active element, as a cathode material, and even applicability as an anode material can be discussed. A mixed crystal series in which Ga can be exchanged for Al to a certain amount has been demonstrated as well,[53] and an analogous mixed crystal series with the redox-active Fe^{3+} which has an ionic radius very similar to the one of Al^{3+} is very probable. As we focused on materials with a Li:Ga ratio of 1:1, we did not follow the idea of optimizing the reaction conditions towards the synthesis of pure $LiGa_5O_8$, however, this may be easily done by either taking the highly reactive intermetallic phase $LiGa_6$ or a mixture of $LiGa_6$ with LiGa resulting in a Li:Ga ratio of 1:5 as starting material. The principal accessibility of spinel-type materials from the respective intermetallic precursor materials has already been demonstrated on the examples of $(Co/Ni)Al_2O_4$ and $SnMg_2O_4$.[56,57]

GaN and Li_3GaN_2

Nitrides can also be obtained from intermetallic precursors, and there are multiple ways at choice: reaction with streaming nitrogen or ammonia at elevated temperatures,[58,59] high-pressure reactions in nitrogen- or ammonia-filled autoclaves,[60,61] eventually under solvothermal conditions,[62,63] conversion with reactive azides or nitrides,[64,65] or synthesis in a hot isostatic press under nitrogen atmosphere.[66,67] LiGa was nitridized in a hot isostatic press (HIP) at 300 bar nitrogen pressure and 800 °C for 5 h, resulting in an off-white powder consisting of GaN and Li_3GaN_2 in a 3:2 ratio according to Rietveld refinements (see Figure 2.11). Products and product ratios may be influenced by reaction conditions and by reaction pathways: alternative routes may yield other ratios or phase-pure products. The formation of Li_3GaN_2 was first reported starting from Li_3Ga as an intermetallic precursor in nitrogen atmosphere[14], or from lithium amide and gallium nitride under solvothermal conditions in a nitrogen-filled autoclave.[15] It cystallizes in an ordered variant of the anti-CaF_2 structure type according to $(Li_3Ga)N_2$ with Ga and Li sharing the tetrahedral voids in an fcc nitride anion packing (see Figure 2.7), and like the above mentioned $LiGaO_2$ and $LiGaS_2$ may be of interest as solid lithium ion electrolyte in an optimized form with respect to doping and vacancy control. Furthermore, Li_3GaN_2 has been proposed as a valuable nutrient in ammonothermal preparations of GaN single crystals.[68] Today, no further ternary Li–Ga nitridic compounds are known, but the application of intermetallic precursor materials in combination with the above mentioned plethora of nitridization methods can help in exploring the ternary system Li–Ga–N on a rational and comprehensive basis.

2.2.4 Experimental

Preparation of LiGa was conceptualized according to the Li-Ga phase diagram by Sangster and Pelton.[71] All handling was performed in an argon-filled glovebox to exclude moisture and oxygen (Unilab, MBraun, Garching, Germany; $O_2 \leq 1$ ppm; $H_2O \leq 1$ ppm). Equimolar mixtures of elemental gallium (14.50 mmol, 1010.9 mg; smart elements, 99.999 %) and lithium (14.47 mmol, 100.4 mg; Max-Planck-Institut für Festkörperforschung, Stuttgart, Germany, multiply distilled) were reacted in weld-sealed tantalum ampoules. The ampoules were heated to 1073 K under vacuum for 1 h and then cooled to room-temperature. The resulting products consisted of bright metallic crystalline reguli. LiGa is reactive towards air and moisture.

For the preparation of $LiGaO_2$, LiGa (1.30 mmol, 100 mg) was finely ground under inert atmosphere and subsequently placed in corundum crucible which then was heated to 1073 K in air in a muffle furnace for 8 days, resulting in a colorless phase-pure powder. $LiGaS_2$ was synthesized by mixing LiGa (3.55 mmol, 272.0 mg) and sulfur (7.80 mmol, 250.2 mg). The mixture was filled into a glassy carbon crucible and sealed under vacuum in a quartz glass ampoule to prevent sulfur sublimating off prior to reacting with LiGa. The ampoule was heated to 1073 K with a rate of 40 K/h, held for 24 h and subsequently cooled to RT with a rate of 40 K/h. The product was a phase-pure white powder.

Table 2.8: Results of the Rietveld refinements of $LiGaO_2$, $LiGaS_2$, GaN, Li_3GaN_2 and $LiGa_5O_8$ (see also Figure 2.11).

Refined composition		$LiGaO_2$	$LiGaS_2$	GaN	Li_3GaN_2	$LiGa_5O_8$
Crystal system		orthorhombic	orthorhombic	hexagonal	cubic	cubic
Space group		$Pna2_1$, No. 33	$Pna2_1$, No. 33	$P6_3mc$, No. 186	$Ia\bar{3}$, No. 206	$P4_332$, No. 212
Formula units	Z	4	4	2	16	4
Lattice parameters / Å, Å^3	a	5.40247(7)	6.51384(12)	3.19114(8)	9.6183(2)	8.1996(3)
	b	6.37374(8)	7.86316(15)			
	c	5.00859(6)	6.21786(12)	5.18767(8)		
	V	172.466(4)	318.474(10)	45.750(2)	889.80(5)	551.29(5)
Radiation, wavelength / Å		— Cu-Kα_1, 1.540560 —				
Data collection range 2ϑ / °		— 5.0 - 90.0 —				
Step size / °		— 0.015 —				
Data points		— 5667 —				
Background function		— Chebyshev —				
Background param.		19	19	11	11	12
Peak shape function		— Pearson VII —		— Finger-Cox-Jephcoat —		
R values / %	R_P	7.779	15.703	9.680	9.680	8.927
	R_{wP}	10.786	24.127	13.647	13.647	11.869
	R_F	1.985	2.662	2.433	2.433	8.132
	R_{Bragg}	3.111	2.450	7.834	7.834	7.917
	GooF	1.075	1.011	0.922	0.922	1.196
Software		— EXPO version 1.17.08 [69] —		— GSAS-II version 4181 [70] —		
Phase	Site	Wyckoff site	x	y	z	U_{iso}
$LiGaO_2$	Ga1	4a	0.0824(2)	0.1269(5)	0.0011(4)	0.0021(8)
	Li1	4a	0.412(3)	0.140(6)	0.463(4)	0.011(4)
	O1	4a	0.4055(12)	0.147(2)	0.8925(7)	0.007(3)
	O2	4a	0.0650(12)	0.119(2)	0.3669(6)	0.007(3)
$LiGaS_2$	Ga1	4a	0.0732(5)	0.1259(16)	0.000(9)	0.010(9)
	Li1	4a	0.412(7)	0.122(19)	0.475(12)	0.015(17)
	S1	4a	0.4072(14)	0.135(2)	0.8838(12)	0.012(2)
	S2	4a	0.0659(14)	0.115(2)	0.3645(12)	0.012(2)
Li_3GaN_2	Ga1	16c	0.1162(2)	x	x	0.0025(12)
	Li1	48e	0.146(6)	0.369(4)	0.129(6)	0.013(7)
	N1	8a	0	0	0	0.03(7)
	N2	24d	0.2229(15)	0	1/4	0.03(7)
$LiGa_5O_8$	Ga1	12d	1/8	0.3744(17)	$-y$+1/4	0.0083(4)
	Ga2	8c	−0.0018(14)	x	x	0.0083(4)
	Li1	4b	5/8	5/8	5/8	0.005(5)
	O1	8c	0.381(6)	x	x	0.0060(15)
	O2	24e	0.1032(25)	0.1030(29)	0.3491(22)	0.0060(15)

Li_3GaN_2 and GaN were obtained as a product mixture from reactions in a hot isostatic press (HIP). LiGa (1.10 mmol, 84.6 mg) was filled into a tungsten crucible under argon. The crucible was placed in the HIP and the reaction chamber was filled with 10 bar nitrogen. It was then heated to 1073 K (300 K/h) under a nitrogen pressure of 300 bar for 5 h. The product was a powder of white color. Nitridation reactions were performed with the use of a HIP of the type AIP6-30H-PED-Ce (American Isostatic Presses Inc., Columbus, Ohio, USA), with a maximum working pressure of 30000 psi. The pressure was delivered by a compressor (type DLE 5-30-2 (MAXIMATOR GmbH, Nordhausen, Germany)).

For X-ray powder diffraction (PXRD) measurements, samples were sealed in glass capillaries with an inner diameter of 0.3 mm and a wall thickness of 0.01 mm (Hilgenberg GmbH, Malsfeld Germany) under argon. Data were collected on a STOE STADI P diffractometer system (Stoe & Cie, Darmstadt, Germany, Cu-$K_{\alpha 1}$ radiation, Ge(111) monochromator, Mythen-1K detector (Dectris, Baden-Dättiswil, Switzerland)) in parafocusing Debye-Scherrer geometry. Phase identification was performed by comparing recorded diffraction patterns with patterns calculated from single crystal data. Rietveld refinements were performed with the literature models serving as starting values. The program packages EXPO[69] and GSAS-II[70] were used to refine all atomic fractional coordinates and isotropic thermal displacement parameters, as well as mixed Li/Ga occupations in LiGa (see Figures 2.8 and 2.11).

Electrochemical impedance spectroscopy (EIS) and galvanostatic polarization measurements were performed with an Ivium compactstat.h (Ivium Technologies, Eindhoven, Netherlands, 24 bit instrument) using a two-electrode setup and a home-built impedance cell kept under air during all measurements. The applied rms AC voltage was 100 mV. The impedance spectra were analyzed with the RelaxIS3 software by rhd instruments. The samples were compacted to a pellet of 1 to 2 mm thickness and 5 mm diameter by uniaxial cold pressing (500 MPa). The pellets were sandwiched between graphite foil (Alfa Aesar, 0.127 mm thick, 99.99 % (metals basis)) to improve the contact with the measuring cells.

Density functional theory (DFT) calculations were performed for the electronic structures of $LiGaO_2$ and $LiGaS_2$. The structure relaxation based on the refined crystal structure models was carried out with the Vienna ab-initio simulation package (VASP).[72–74] The electron exchange interaction was calculated with modified Becke-Johnson potentials (Meta-GGA-functinal)[75–77] for a more realistic approximation of band gaps and also with generalized gradient approximation (GGA)[78,79] for comparison. The Brillouin zone was scanned with k-meshes of $10 \cdot 8 \cdot 10$ for $LiGaO_2$ and $8 \cdot 7 \cdot 9$ for $LiGaS_2$ following the method of Monkhorst and Pack.[80]

Inductively coupled plasma optical emission spectrometry (ICP-OES) was performed on LiGa samples to monitor the Li:Ga ratio. All samples were measured on a Varian Vista rl CCD simultaneous ICP-AES (Varian Inc., Palo Alto, California, USA) with the emission band wavelength of Ga = 294,363 nm and Li = 670,783 nm.

Conclusion

The application of intermetallic precursors for the synthesis of complex ionic materials is widely underestimated. Several reports on their use for oxidic materials can be found in literature, however, the great benefit of intermetallics as starting compounds has never been comprehensively recognized, especially with regard to non-oxidic materials, such as nitrides, sulfides or halogenides. In all cases where the pure elements are moderately reactive, high reactions temperatures are necessary for product formation starting from the elements. Long process times result from solid state reactions. Both factors combine to costly and energy-consumig processes. In comparison, the use of reactive intermetallic precursors brings along a number of benefits: (1) low-melting intermetallic phases or suitable eutectic mixtures create a liquid phase, enhancing mobility and reducing reaction duration considerably, (2) intermetallic phases with low-lying decomposition or phase transition temperatures reduce activation enthalpies, (3) intermetallic phases (rather than solid solutions or multi-phase alloys) exhibit defined interatomic ratios which in the utmost cases can be chosen fitting to those present in the desired products, (4) intermetallic precursors do not create high gas pressures in initial reaction steps. Other beneficial effects can result from Zintl phases which in general show much higher reactivities than their constituting elements. Furthermore, many intermetallic phases are brittle and can much more easily be ground to fine powders than pure metals, resulting in homogeneous starting mixtures.

Illustraded by the example of LiGa, an easily accessible intermetallic phase, we could show that a diverse spectrum of interesting products can be targetted, and the comparison with reported literature syntheses is especially striking for $LiGaO_2$, $LiGaS_2$ and $LiGa_5O_8$ when it comes to reaction conditions. Among the products of the reactions of LiGa with air, sulfur and nitrogen are several materials of potential interest for applications in various fields. With these examples for the convenient synthesis of ternary chalcogenides and nitrides we intended to give further examples for the prospects of using reactive intermetallic precursors in modern preparative inorganic chemistry.

References

[1] Y. Guo, F. Liang, Z. Li, W. Xing, Z.-s. Lin, J. Yao, A.Mar, Y Wu, AHgSnQ_4 (A = Sr, Ba; Q = S, Se): A Series of Hg-Based Infrared Nonlinear-Optical Materials with Strong Second-Harmonic-Generation Response and Good Phase Matchability. *Inorg. Chem.* (2019) **58** 10390-10398, DOI: 10.1021/acs.inorgchem.9b01572.

[2] G. Bruzzone, F. Merlo, The strontium-mercury system. *J. Less-Common Met.* (1974) **35** 153-157, DOI: 10.1016/0022-5088(74)90154-4.

[3] R. Ferro, The crystal structures of SrCd, BaCd, SrHg and BaHg. *Acta Crystallogr.* (1954) **7** 781, DOI: 10.1107/s0365110x5400240x.

[4] G. Bruzzone, F Merlo, The barium-mercury system. *J. Less-Common Met.* (1975) **39** 271-276, DOI: 10.1016/0022-5088(75)90201-5.

[5] *Binary Alloy Phase Diagrams*, 2nd ed.; T. B. Massalski, H. Okamoto, P. R. Subramanian, Eds.; ASM International: Materials Park, Ohio, USA, 1990.

[6] F. Merlo, M. L. Fornasini, CrB-type equiatomic compounds of europium, ytterbium and alkaline-earth metals with Si, Ge, Sn, Pb. *J. Less-Common Met.* (1967) **13** 603-610, DOI: 10.1016/0022-5088(67)90105-1.

[7] W. Rieger, E. Parthé, Alkaline earth silicides, germanides and stannides with CrB structure type. *Acta Crystallogr.* (1967) **22** 919-922, DOI: 10.1107/s0365110x67001793.

[8] F. Merlo, M. Pani, M. L. Fornasini, RMX compounds formed by alkaline earths, europium and ytterbium III. Ternary phases with M = Mg, Hg and X = Si, Ge, Sn, Pb. *J. Alloys Compd.* (1993) **196** 145-148, DOI: 10.1016/0925-8388(93)90585-b.

[9] W. Huang, Z. He, B. Zhao, S. Zhu, B. Chen, Y. Wu, Effect of Thermal Annealing Treatment and Defect Analysis on $AgGaGeS_4$ Single Crystals. *Inorg. Chem.* (2019) **58** 10846-10855, DOI: 10.1021/acs.inorgchem.9b01162.

[10] P. Feschotte, P. Bass, Y. Nakamura, Un nouveau composé intermétallique très timide: AgGa. *J. Less-Common Met.* (1991) **171** 157-162, DOI: 10.1016/0022-5088(91)90272-6.

[11] A. E. Gunnæs, A. Olsen, P. T. Zagierski, B. Klewe, O. B. Karlsen, A. Aasen, Crystal structure determination of Ag_2Ga by single crystal X-ray diffraction. *Z. für Kristallogr.—Cryst. Mater.* (1998) **213** 639-644, DOI: 10.1524/zkri.1998.213.12.639.

[12] H. Watanabe, N. Kijima, Synthesis of $Sr_{0.99}Eu_{0.01}AlSiN_3$ from Intermetallic Precursor. *J. Ceram. Soc. Jpn.* (2009) **117** 115-119, DOI: 10.2109/jcersj2.117.115.

[13] J. Sappl, C. Hoch, Synthesis and Crystal Structure of three new Lithium Gallides. *Z. Krist. Suppl.* (2019) **39** 91.

[14] R. Juza, F. Hund, Die ternären Nitride Li_3AlN_2 und Li_3GaN_2. 17. Mitteilung über Metallamide und Metallnitride. *Z. Anorg. Chem.* (1948) **257** 13-25, DOI: 10.1002/zaac.19482570102.

[15] G. Goglio, A. Denis, E. Gaudin, C. Labrugère, D. Foy, A. Largeteau, Solvothermal Processes for Nitride Synthesis: Examples of Li_3GaN_2 and Graphitic C_3N_4 Elaboration. *Z. Naturforschung B* (2008) **63** 730-738, DOI: 10.1515/znb-2008-0621.

[16] M. Marezio, The crystal structure of $LiGaO_2$. *Acta Crystallogr.* (1965) **18** 481-484, DOI: 10.1107/s0365110x65001068.

[17] W. Hönle, G. Miller, A. Simon, Preparation, crystal structures, and electronic properties of $LiGaCl_3$ and $LiGaI_3$. *J. Solid State Chem.* (1988) **75** 147-155, DOI: 10.1016/0022-4596(88)90312-x.

[18] V. Kinshibalo, E. Melnik, O. Zmii, An investigation of the ternary Mg-Li-(Ga, Ge, In, Tl, Pb) systems. *Russ. Metall.* (1979) **4** 192-196.

[19] J. F. Herbst, L. G. Hector, W. Wolf, Ab initio thermodynamic and elastic properties of $AGaH_4$ hydrides (A = Li, Na, K, Rb, and Cs). *Phys. Rev. B: Condens. Matter Mater. Phys.* (2010) **82** 024110, DOI: 10.1103/physrevb.82.024110.

[20] J. Leal-Gonzalez, S. A. Melibary, A. J. Smith, Structure of lithium gallium sulfide, $LiGaS_2$. *Acta Crystallogr., Sect. C: Cryst. Struct. Commun.* (1990) **46** 2017-2019, DOI: 10.1107/s0108270190002165.

[21] W. Hönle, B. Hettich, A. Simon, Darstellung und Kristallstrukturen von $LiGaCl_4$ und $LiGaI_4$/ Preparation and Crystal Structure of $LiGaCL_4$ and $LiGaI_4$. *Z. Naturforsch., B: J. Chem. Sci.* (1987) **420** 248-250, DOI: 10.1515/znb-1987-0222.

[22] H. Nowotny, F. Holub, Untersuchungen an metallischen Systemen mit Flußspatphasen. *Monatsh. Chem.* (1960) **91** 877-887, DOI: 10.1007/bf00929560.

[23] K. Kuriyama, T. Nozaki, Single-crystal growth and characterization of $LiGaSe_2$. *J. Appl. Phys.* (1981) **52** 6441-6443, DOI: 10.1063/1.328553.

[24] W. Hönle, A. Simon, Darstellung und Kristallstrukturen von $LiGaBr_4$ und $LiGaBr_3$/ Preparation and Crystal Structure of $LiGaBr_4$ and $LiGaBr_3$. *Z. Naturforsch., B: J. Chem. Sci.* (1986) **41** 1391-1398, DOI: 10.1515/znb-1986-1113.

[25] L. Isaenko, A. Yelisseyev, S. Lobanov, A. Titov, V. Petrov, J.-J. Zondy, P. Krinitsin, A. Merkulov, V. Vedenyapin, J. Smirnova, Growth and properties of $LiGaX_2$ (X = S, Se, Te) single crystals for nonlinear optical applications in the mid-IR. *Cryst. Res. Technol.* (2003) **380** 379-387, DOI: 10.1002/crat.200310047.

[26] W. Bockelmann, H. Jacobs, H.-U. Schuster, Notizen: Die Kristallstruktur der Verbindung LiGaGe. *Z. Naturforsch., B: Anorg. Chem., Org. Chem., Biochem., Biophys., Biol.* (1970) **25** 1305-1306, DOI: 10.1515/znb-1970-1120.

[27] G. Dmytriv, I. Tarasiuk, V. Pavlyuk, Li-Ag-Ga system. *Visn. Lviv. Derzh. Univ., Ser. Khim.* (2014) **55** 29-36.

[28] A. Czybulka, A. Petersen, H.-U. Schuster, Lithium-platinmetall-Al(Ga, In)-legierungen: Neue farbige ternäre intermetallische phasen. *J. Less-Common Met.* (1990) **161** 303-312, DOI: 10.1016/0022-5088(90)90041-h.

[29] E. Zintl, G. Brauer, Über die Valenzelektronenregel und die Atomradien unedler Metalle in Legierungen. *Z. Phys. Chem. B* (1933) **20** 245-271, DOI: 10.1515/zpch-1933-2023.

[30] M. Marezio, J. P. Remeika, High pressure phase of $LiGaO_2$. *J. Phys. Chem. Solids* (1965) **26** 1277-1280, DOI: 10.1016/0022-3697(65)90108-3.

[31] L. Lei, T. Irifune, T. Shinmei, H. Ohfuji, L. Fang, Cation order-disorder phase transitions in $LiGaO_2$: Observation of the pathways of ternary wurtzite under high pressure. *J. Appl. Phys.* (2010) **108** 083531, DOI: 10.1063/1.3487976.

[32] P. Knoll, H. Kuzmany, Nonlinear-optical properties and signs of the Raman tensor for $LiGaO_2$. *Phys. Rev. B: Condens. Matter Mater. Phys.* (1984) **29** 2221-2226, DOI: 10.1103/physrevb.29.2221.

[33] M. M. C. Chou, D.-R. Hang, C. Chen, Y.-H. Liao, Epitaxial growth of nonpolar m-plane ZnO (10-10) on large-size $LiGaO_2$ (100) substrates. *Thin Solid Films* (2011) **519** 3627-3631, DOI: 10.1016/j.tsf.2011.01.343.

[34] P. Waltereit, O. Brandt, A. Trampert, H. T. Grahn, J. Menniger, M. Ramsteiner, M. Reiche, K. H. Ploog, Nitride semiconductors free of electrostatic fields for efficient white light-emitting diodes. *Nature* (2000) **406** 865-868, DOI: 10.1038/35022529.

[35] S. Kück, S. Hartung, Comparative study of the spectroscopic properties of Cr^{4+}-doped $LiAlO_2$ and $LiGaO_2$. *Chem. Phys.* (1999) **240** 387-401, DOI: 10.1016/s0301-0104(98)00390-5.

[36] A. Boonchun, W. R. L. Lambrecht, First-principles study of the elasticity, piezoelectricity, and vibrational modes in $LiGaO_2$ compared with ZnO and GaN. *Phys. Rev. B: Condens. Matter Mater. Phys.* (2010) **81** 235214, DOI: 10.1103/physrevb.81.235214.

[37] H. Kabelka, H. Kuzmany, P. Krempl, Raman scattering of $LiGaO_2$. *Solid State Commun.* (1978) **27** 1159-1162, DOI: 10.1016/0038-1098(78)91133-x.

[38] L. Lei, D. He, Synthesis of GaN Crystals Through Solid-State Metathesis Reaction Under High Pressure. *Cryst. Growth Des.* (2009) **9** 1264-1266, DOI: 10.1021/cg801017h.

[39] B. Ivanov-Emin, Y. Rabovik, Chemistry of gallium. III. Thiogallates of alkali metals. *J. Gen. Chem. USSR* (1947) **17** 1247-1252.

[40] R. Hoppe, Ternary alkali metal oxides. *Bull. Soc. Chim. Fr.* (1965) **1965** 1115-1121.

[41] V. V. Atuchin, L. I. Isaenko, V. G. Kesler, S. I. Lobanov, Core level photoelectron spectroscopy of $LiGaS_2$ and Ga-S bonding in complex sulfides. *J. Alloys Compd.* (2010) **497** 244-248, DOI: 10.1016/j.jallcom.2010.03.020.

[42] V. Petrov, A. Yelisseyev, L. Isaenko, S. Lobanov, A. Titov, J.-J. Zondy, Second harmonic generation and optical parametric amplification in the mid-IR with orthorhombic biaxial crystals $LiGaS_2$ and $LiGaSe_2$. *Appl. Phys. B* (2004) **78** 543-546, DOI: 10.1007/s00340-004-1463-0.

[43] M. Trömel, Metallradien, Ionenradien und Wertigkeiten fester metallischer Elemente/Metallradien, Ionenradien und Wertigkeiten fester metallischer Elemente. *Z. Naturforschung B* (2000) **55**, 243-247, DOI: 10.1515/znb-2000-3-403.

[44] Z. Kish, V. Lostshack, E. Peresh, E. Semrad, Properties of lithium gallium sulfide ($LiGaS_2$) crystals. *Inorg. Mater.* (1989) **25** 1659-1662.

[45] V. V. Atuchin, L. I. Isaenko, V. G. Kesler, S. Lobanov, H. Huang, Z. S. Lin, Electronic structure of $LiGaS_2$. *Solid State Commun.* (2009) **149** 572-575, DOI: 10.1016/j.ssc.2008.12.048.

[46] A. Eifler, V. Riede, J. Brückner, S. Weise, V. Krämer, G. Lippold, W. Schmitz, K. Bente, W. Grill, Band Gap Energies and Lattice Vibrations of the Lithium Ternary Compounds $LiInSe_2$, $LiInS_2$, $LiGaSe_2$ and $LiGaS_2$. *Jpn. J. Appl. Phys.* (2000) **39** 279, DOI: 10.7567/jjaps.39s1.279.

[47] N. Kamaya, K. Homma, Y. Yamakawa, M. Hirayama, R. Kanno, M. Yonemura, T. Kamiyama, Y. Kato, S. Hama, K. Kawamoto, A. Mitsui, A lithium superionic conductor. *Nat. Mater.* (2011) **10** 682-686, DOI: 10.1038/nmat3066.

[48] A. Kuhn, O. Gerbig, C. Zhu, F. Falkenberg, J. Maier, B. V. Lotsch, A new ultrafast superionic Li-conductor: ion dynamics in $Li_{11}Si_2PS_{12}$ and comparison with other tetragonal LGPS-type electrolytes. *Phys. Chem. Chem. Phys.* (2014) **16** 14669-14674, DOI: 10.1039/c4cp02046d.

[49] T. Holzmann, L. M. Schoop, M. N. Ali, I. Moudrakovski, G. Gregori, J. Maier, R. J. Cava, B. V. Lotsch, $Li_{0.6}[Li_{0.2}Sn_{0.8}S_2]$ – a layered lithium superionic conductor. *Energy Environ. Sci.* (2016) **9** 2578-2585, DOI: 10.1039/c6ee00633g.

[50] A. Jain, S. P. Ong, G. Hautier, W. Chen, W. D. Richards, S. Dacek, S. Cholia, D. Gunter, D. Skinner, G. Ceder, K. A. Persson, Commentary: The Materials Project: A materials genome approach to accelerating materials innovation. *APL Mater.* (2013) **1** 011002, DOI: 10.1063/1.4812323.

[51] N. W. Johnson, J. A. McLeod, A. Moewes, The electronic structure of lithium metagallate. *J. Phys.: Condens. Matter* (2011) **23** 445501, DOI: 10.1088/0953-8984/23/44/445501.

[52] C. Chen, C.-A. Li, S.-H. Yu, M. M. C. Chou, Growth and characterization of $LiGaO_2$ single crystal. *J. Cryst. Growth* (2014) **402** 325-329, DOI: 10.1016/j.jcrysgro.2014.06.040.

[53] J. Joubert, M. Brunel, A. Waintal, A. Durif, Etude cristallographique du gallate de lithium et de sa solution solide avec l'aluminate. *C. R. Hebd. Seances Acad. Sci.* (1963) **256** 5324-5326.

[54] A. Kraytsberg, Y. Ein-Eli, Higher, Stronger, Better... A Review of 5 Volt Cathode Materials for Advanced Lithium-Ion Batteries. *Adv. Energy Mater.* (2012) **2** 922-939, DOI: 10.1002/aenm.201200068.

[55] M. M. Thackeray, L. A. de Picciotto, A. de Kock, P. J. Johnson, V. A. Nicholas, K. T. Adendorff, Spinel electrodes for lithium batteries—A review. *J. Power Sources* (1987) **21** 1-8, DOI: 10.1016/0378-7753(87)80071-x.

[56] T. P. Yadav, R. S. Tiwari, O. N. Srivastava, N. K. Mukhopadhyay, Evolution of a Nanocrystalline $(Co,Ni)Al_2O_4$ Spinel Phase from Quasicrystalline Precursor. *Int. J. Appl. Ceram. Technol.* (2008) **5** 449-457, DOI: 10.1111/j.1744-7402.2008.02243.x.

[57] A.-M. Azad, Novel synthesis of high phase-purity Mg_2SnO_4 from metallic precursors via powder metallurgy route. *Mater. Res. Bull.* (2001) **36** 755-765, DOI: 10.1016/s0025-5408(01)00533-5.

[58] T. E. O'Connor, Synthesis of boron nitride. *J. Am. Chem. Soc.* (1962) **84** 1753-1754, DOI: 10.1021/ja00868a065.

[59] T. Nakagawa, H. Matsuoka, M. Sawa, K. Idehara, M. Katsura, Preparation of lanthanide nitrides by carbothermic reduction using ammonia. *J. Nucl. Mater.* (1997) **247** 147-150, DOI: 10.1016/s0022-3115(97)00037-8.

[60] H. Jehn, P. Ettmayer, The molybdenum–nitrogen phase diagram. *J. Less-Common Met.* (1978) **58** 85-98, DOI: 10.1016/0022-5088(78)90073-5.

[61] A. Leineweber, H. Jacobs, S. Hull, Ordering of Nitrogen in Nickel Nitride Ni_3N Determined by Neutron Diffraction. *Inorg. Chem.* (2001) **40** 5818-5822, DOI: 10.1021/ic0104860.

[62] A. Denis, G. Goglio, G. Demazeau, Gallium nitride bulk crystal growth processes: a review. *Mater. Sci. Eng., R* (2006) **50** 167-194, DOI: 10.1016/j.mser.2005.11.001.

[63] J. Häusler, L. Neudert, M. Mallmann, R. Niklaus, A.-C. L. Kimmel, N. S. A. Alt, E. Schlücker, O. Oeckler, W. Schnick, Ammonothermal Synthesis of Novel Nitrides: Case Study on $CaGaSiN_3$. *Chem.—Eur. J.* (2016) **23** 2583-2590, DOI: 10.1002/chem.201605344.

[64] A. L. Hector, I. P. Parkin, Sodium azide as a reagent for solid state metathesis preparations of refractory metal nitrides. *Polyhedron* (1995) **14** 913-917, DOI: 10.1016/0277-5387(94)00314-5.

[65] E. G. Gillan, R. B. Kaner, Rapid solid-state synthesis of refractory nitrides. *Inorg. Chem.* (1994) **33** 5693-5700, DOI: 10.1021/ic00103a015.

[66] T. Nakagawa, T. Arakawa, K. Sako, N. Tomioka, T. A. Yamamoto, T. Kusunose, K. Niihara, K. Kamiya, T. Numazawa, Magnetocaloric effects of ferromagnetic erbium mononitride. *J. Alloys Compd.* (2006) **408–412** 191-195, DOI: 10.1016/j.jallcom.2005.04.061.

[67] J. W. McMurray, J. O. Kiggans, G. W. Helmreich, K. A. Terrani, Production of near-full density uranium nitride microspheres with a hot isostatic press. *J. Am. Ceram. Soc.* (2018) **101** 4492-4497, DOI: 10.1111/jace.15766.

[68] H. Bao, B. Song, H. Li, G. Wang, W. Wang, W. Wang, X. Chen, GaN Single Crystals: Growth Mechanism and Temperature-Modulated Growth Using Li_3N *Flux*. *Cryst. Growth Des.* (2009) **9** 611-615, DOI: 10.1021/cg800925t.

[69] A. Altomare, C. Cuocci, C. Giacovazzo, A. Moliterni, R. Rizzi, N. Corriero, A. Falcicchio, EXPO2013: a kit of tools for phasing crystal structures from powder data. *J. Appl. Crystallogr.* (2013) **46** 1231-1235, DOI: 10.1107/s0021889813013113.

[70] B. H. Toby, R. B. Von Dreele, GSAS-II: the genesis of a modern open-source all purpose crystallography software package. *J. Appl. Crystallogr.* (2013) **46** 544-549, DOI: 10.1107/s0021889813003531.

[71] J. Sangster, A. D. Pelton, The Ga-Li (Gallium-Lithium) System. *J. Phase Equilib.* (1991) **12** 33-36, DOI: 10.1007/bf02663670.

[72] G. Kresse, J. Hafner, Ab initio molecular dynamics for liquid metals. *Phys. Rev. B: Condens. Matter Mater. Phys.* (1993) **47** 558-561, DOI: 10.1103/physrevb.47.558.

[73] G. Kresse, J. Hafner, Ab initio molecular-dynamics simulation of the liquid-metal–amorphous-semiconductor transition in germanium. *Phys. Rev. B: Condens. Matter Mater. Phys.* (1994) **49** 14251-14269, DOI: 10.1103/physrevb.49.14251.

[74] G. Kresse, J. Furthmüller, Efficiency of ab-initio total energy calculations for metals and semiconductors using a plane-wave basis set. *Comput. Mater. Sci.* (1996) **6** 15-50, DOI: 10.1016/0927-0256(96)00008-0.

[75] A. D. Becke, E. R. Johnson, A simple effective potential for exchange. *J. Chem. Phys.* (2006) **124** 221101, DOI: 10.1063/1.2213970.

[76] F. Tran, P. Blaha, Accurate Band Gaps of Semiconductors and Insulators with a Semilocal Exchange-Correlation Potential. *Phys. Rev. Lett.* (2009) **102** 226401, DOI: 10.1103/physrevlett.102.226401.

[77] J. A. Camargo-Martínez, R. Baquero, Performance of the modified Becke-Johnson potential for semiconductors. *Phys. Rev. B: Condens. Matter Mater. Phys.* (2012) **86** 195106, DOI: 10.1103/physrevb.86.195106.

[78] J. P. Perdew, K. Burke, M. Ernzerhof, Generalized Gradient Approximation Made Simple. *Phys. Rev. Lett.* (1996) **77** 3865-3868, DOI: 10.1103/physrevlett.77.3865.

[79] J. P. Perdew, K. Burke, M. Ernzerhof, Generalized Gradient Approximation Made Simple [Phys. Rev. Lett. 77, 3865 (1996)]. *Phys. Rev. Lett.* (1997) **78** 1396, DOI: 10.1103/physrevlett.78.1396.

[80] H. J. Monkhorst, J. D. Pack, Special points for Brillouin-zone integrations. *Phys. Rev. B: Solid State* (1976) **13** 5188-5192, DOI: 10.1103/physrevb.13.5188.

2.3 Synthesis and Crystal Structure of Three Ga-rich Lithium Gallides, $LiGa_6$, $Li_{11}Ga_{24}$ and $LiGa_2$

Jonathan Sappl and Constantin Hoch

Department Chemie, Ludwig-Maximilians-Universität München, Butenandtstraße 5-13 (D), D-81377 München, Germany, Phone: +49 (0)89 2180-77421, Fax: +49 (0)89 2180-77440

published in: *Inorg. Chem.* **59** (2020) 6566–6580. DOI: 10.1021/acs.inorgchem.0c00674.

2.3.1 Abstract

Three new binary phases have been synthesized in the Ga-rich part of the Li-Ga system: $LiGa_6$, $Li_{11}Ga_{24}$ and $LiGa_2$. Their crystal structures and the respective phase formation conditions have been investigated with X-ray single crystal structure refinements, Rietveld refinements of X-ray powder diffraction data and thermal analyses. They complete the Ga-rich part of the Li–Ga phase diagram together with the reported phases $Li_{6-x}Ga_{14}$ with $2 \leq x \leq 3$ and $LiGa_{3.42}$. The compositions of two of the new gallides, $LiGa_6$ and $LiGa_2$, had been predicted in previous thermoanalytical studies but their crystal structures remained unknown. All three new binary main group compounds adopt new structure types. $LiGa_6$ crystallizes with the trigonal space group $R\bar{3}c$ (No. 167, a = 6.1851(8) Å, c = 23.467(4) Å), $Li_{11}Ga_{24}$ crystallizes with the hexagonal space group $P6_3mc$ (No. 186, a = 13.7700(19) Å, c = 23.250(5) Å), and $LiGa_2$ with the orthorhombic space group $Cmce$ (No. 64, a = 8.51953(4) Å, b = 14.44163(7) Å, c = 15.29226(7) Å). All phases form air- and moisture-sensitive crystals of bright metallic luster. They can be synthesized starting from the pure elements and taking into accout their incongruent melting behavior by adequate tempering sequences derived from differential scanning calorimetry (DSC) studies of the system. Lithium gallides do not form electron-precise Zintl phases. The electronic structures of these polar intermetallic phases combine ionic, covalent and metallic bonding contributions and have been analyzed by density functional theory (DFT) calculations in the cases of $LiGa_6$ and $LiGa_2$. Measurements of the specific electronic resistivities have also been performed and prove the metallic behavior.

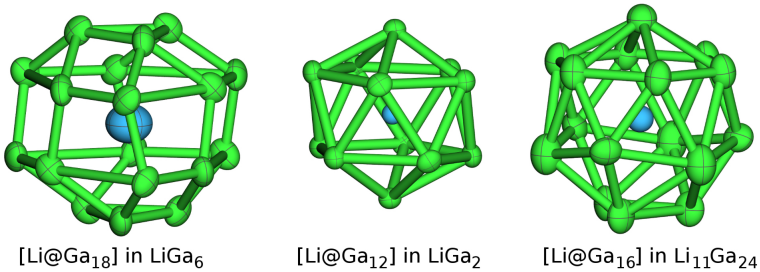

2.3.2 Introduction

The binary intermetallic system Li–Ga contains several phases, some of which have attracted attention in the context of research on alternative anode materials for lithium ion batteries. For example, Li_2Ga has a theoretical capacity of ca. 750 $mAhg^{-1}$ [1], which is about twice the capacity of graphite, the most widely spread anode material today. Furthermore, lithium gallides may be of interest in the field of solid state lithium ion conductors: Today, the solid electrolytes with highest lithium ion mobilities are thiogermanates and gallates[2,3] which mostly are synthesized from the elements at high temperatures. Using intermetallic lithium gallides as precursor materials can improve phase purity and reduce reaction temperatures and durations. Some examples for the benefit of employing intermetallic phases as precursors in syntheses of ionic functional materials have already been demonstrated.[4–6] Despite this interest in the system Li–Ga structural information especially on Ga-rich phases is scarce and some of the phase compositions reported in the literature phase diagrams are subject of debate. With this we thought it purposeful to have a closer look on the Ga-rich part of the Li–Ga phase diagram and to combine methods from preparative solid state chemistry, thermochemical analyses and X-ray crystallography to elucidate formation conditions and crystal structures in this field.

LiGa was the first phase introduced in the Li-Ga system. In 1933 Zintl and Brauer[7] reported phase formation and crystal structure. It crystallizes with the NaTl structure type, and its phase formation, crystallographic details, crystal growth, chemical substitution behavior, phase width and temperature-induced phase transitions was intensively studied.[8–15] A first phase diagram was published about 40 years later when Thümmel and Klemm performed detailed thermoanalytic studies and as a result predicted Li-rich phases with compositions Li_3Ga_2 and Li_2Ga in 1970.[16] The phase diagram was amended by thermoanalytic studies performed in 1973 by Yatsenko[11] who suggested the existence of a Ga-rich phase with composition $LiGa_4$ and confirmed the thermic effects pointing towards Li_3Ga_2, however, the respective X-ray powder diffraction studies mentioned in the manuscript were never published. In 1977, crystal structures of Li_3Ga_2 and Li_2Ga were presented.[17] Additional Ga-rich phases $LiGa_2$ and $LiGa_3$ were suggested by Yatsenko in 1977[18] but could not be structurally verified, and Belin and Ling attributed the related thermal effects to the newly described crystal structure of $Li_{6-x}Ga_{14}$.[19,20] In $Li_{6-x}Ga_{14}$ with x = 3 the lithium positions are only half occupied, and this composition is close to $LiGa_3$ whereas in the phase Li_6Ga_{14} all Li positions would be fully occu-

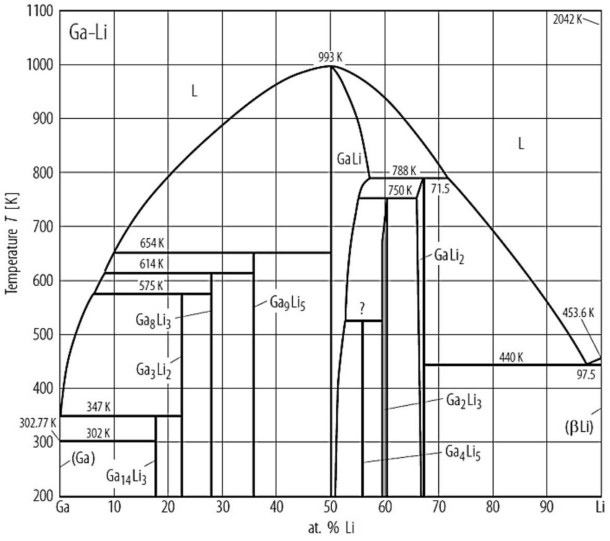

Figure 2.12: Phase Diagram of the binary system Li–Ga as published in literature.[27]

Table 2.9: Optimized synthesis conditions for $LiGa_6$, $LiGa_2$ and $Li_{11}Ga_{24}$, with T_{max} being the maximum reaction temperature, T_{temp} and t_{temp} the tempering temperature and time and $\dot{T}\uparrow$ and $\dot{T}\downarrow$ the heating and cooling rates, respectively. All samples were held for one hour at T_{max} prior to cooling.

Phase	m(Li) [mg (mmol)]	m(Ga) [mg (mmol)]	$\frac{n(Ga)}{n(Li)}$	T_{max} [K]	$\dot{T}\uparrow$ [K/h]	$\dot{T}\downarrow$ [K/h]	T_{temp} [K]	t_{temp} [d]
$LiGa_6$	15.5 (2.2)	942.2 (13.5)	6.1	1073	200	max[1)]	—	—
$LiGa_2$	23.0 (3.3)	459.6 (6.6)	2.0	1073	200	max[1)]	583	62
$Li_{11}Ga_{24}$	46.6 (6.7)	935.9 (13.4)	2.0	1073	200	max[1)]	523	3

[1)]: Rapid cooling of the ampule in ice water

pied, resulting in a composition close to $LiGa_2$. Phase width and Li distribution in $Li_{6-x}Ga_{14}$ was finally elucidated by electrochemical intercalation experiments combined with neutron diffraction structure determination by Belin in 1990.[21] The value for x seems to be limited to $2 \leq x \leq 3$. In 1981 Stöhr und Schäfer added Li_5Ga_4 to the list of Li-rich binary lithium gallides, based on single crystal studies.[22] In 1984 Belin reported the crystal structure of $LiGa_{3.42}$.[23] Four years later, Belin revisited the phase diagram Li–Ga with modern thermoanalytic tools and predicted four new phases ($LiGa_6$, Li_2Ga_7, Li_3Ga_8 and Li_5Ga_9) by analyzing the observed thermal effects with Tamman diagrams.[24] Li_2Ga_7 corresponds to the phase $Li_{6-x}Ga_{14}$ with $x = 2$. The results of all hitherto gathered studies on the Li-Ga system were evaluated and compiled in a new phase diagram by Sangster and Pelton,[25] who decided to include the following phases ond the basis of the available data: Li_3Ga_{14}, $LiGa_2$, LiGa, Li_5Ga_4, Li_3Ga_2, and Li_2Ga. The phase $LiGa_6$ detected in thermoanalytical work by Belin[24] never was observed in other studies and therefore was neglected, and also the phase $LiGa_{3.42}$ (being different from $Li_{6-x}Ga_{14}$ with $x = 2$) by the same author[23] which previously had found entrance in the Li–Ga phase diagram from 1989 established by van der Lugt[26] had been left out.

The most recent phase diagram[27] in literature is shown in Figure 2.12 and contains the phases Li_3Ga_{14}, Li_2Ga_3, Li_3Ga_8, Li_5Ga_9, LiGa, Li_5Ga_4, Li_3Ga_2 and Li_2Ga. The Li-rich part of the system seems in good agreement with all thermoanalytical studies, and all phases are structurally described, whereas the Ga-rich part still contains many unclear effects and structurally unknown phases.

2.3.3 Experimental section

Synthesis

All phases were synthesized from the pure elements (Ga: smart elements, 99.999%; Li: doubly distilled). The elements were weighed in an argon-filled glovebox (Unilab, MBraun, Garching, Germany, with $p(O_2)$ and $p(H_2O) < 1$ ppm), sealed in tantalum ampules by arc-welding and heated in tube furnaces inside argon-filled quartz protection tubes to prevent oxidation of the ampules. The products all showed bright metallic luster and were isolated from the ampules in argon atmosphere as they are senstive towards air and moisture. Representative parts of the products were ground

in agate mortars and sealed in glass capillaries for X-ray powder diffraction measurements. In some cases, the reaction products were ductile and therefore diluted with diamond powder. For the preparation of suitable single crystals, a part of the reaction product was brought to air under dried paraffin oil and examined under a stereo microscope. For single crystal experiments, xenomorphic fractions of the reguli were selected and sealed in oil-filled capillaries. The individual preparation details for $LiGa_6$, $LiGa_2$ and $Li_{11}Ga_{24}$ with synthesis conditions optimized according to the results of thermoanalytical investigations are compiled in Table 2.9.

Powder X-ray Diffraction

Samples for X-ray powder diffraction measurements were prepared in an argon-filled glovebox. The powder samples were ground in agate mortars, in cases of ductile samples under addition of diamond powder (Sigma Aldrich, $\leq$1 μm synthetic monocrystalline powder). The hygroscopic samples were sealed in glass capillaries ($\varnothing$ = 0.3 mm, Hilgenberg, Malsberg, Germany). Measurements were performed in parafocussing Debye-Scherrer geometry on a STADI P diffractometer system (Stoe & Cie GmbH, Darmstadt, Germany) with Ge-111-monochromatized CuKα1 radiation. Intensities were collected with a Mythen detector (Dectris, Baden-Dättiswil, Switzerland). For phase identification, the detected diffraction patterns were compared to patterns calculated from single crystal data, and Rietveld refinements on $LiGa_6$ were performed employing the progam Topas academical[28] with fundamental parameter approach and a double Voigt model compensating size-strain effects. Phase fractions are given in weight-%. The Rietveld refinement was performed prior to single crystal investigations, therefore the starting values were not taken from the single crystal structure model but from the results of a structure solution by charge flipping methods implemented in Topas academical. The space group was corrected from $R3c$ to $R\bar{3}c$ in the final refinement after symmetry checking with the algorithms com-

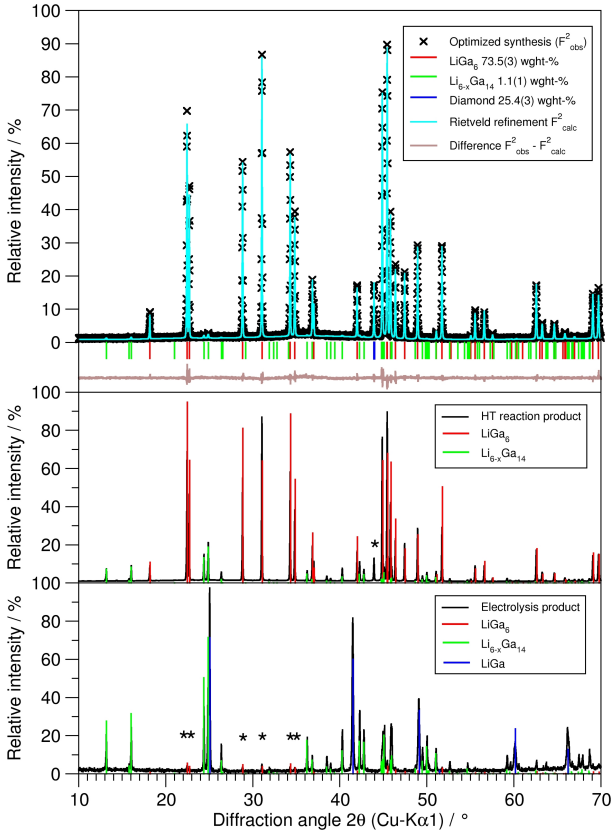

Figure 2.13: Powder X-ray diffraction patterns of $LiGa_6$. Bottom: first appearance as a byphase together with LiGa in an attempt to synthesize $Li_{6-x}Ga_{14}$ in an electrocrystallization process (strongest $LiGa_6$ reflections marked by asterisks), center: $LiGa_6$ as main product next to $Li_{6-x}Ga_{14}$ in a conventional HT synthesis in tantalum ampules (diamond reflection marked by an asterisk), top: Rietveld refinement of an optimized synthesis yielding $LiGa_6$ in high purity. Diamond was used in order to facilitate grinding of the ductile material.

piled in the PLATON package.[29].

Absorption effects were taken into account by calculating the linear absorption coefficient of $LiGa_6$, the packing density and the refined weight percentage of the phase. The background was modelled with shifted Chebychev functions, the profiles with LeBail-Jouanneaux functions. Details on the refinement are given in Table 2.10, and a graphical representation of the results is shown in Figure 2.13.

All other Rietveld refinements were performed with the program GSAS-II[30] with modeling of the background by a Chebychev function with typically 10 to 15 parameters. The peak functions were modeled by mixing of Lorentzian and Gaussian profile functions and introducing an asymmetry parameter. Phase fractions from these refinements are given in atom-%.

Single crystal X-ray diffraction

Inside an argon-filled glovebox, a small portion of the air- and moisture-sensitive reaction products was covered with paraffin oil dried over K metal and subsequently brought to air. Suitable specimens for single crystal X-ray structure analysis were selected under a stereo microscope and sealed in paraffin-filled capillaries ($\varnothing = 0.1$ mm, Hilgenberg, Malsberg, Germany). The crystals were mounted on a three-circle diffractometer system D8 QUEST (Bruker, AXS, Karlsruhe, Germany) equipped with Göbel mirror optics, an air-cooled microfocus X-ray tube with MoKα radiation and a CCD detector Photon II. After quality checking and determination of the orientation matrix on the basis of a set of preliminary exposure frames intensity data of at least one half of the Ewald sphere were collected at room temperature (ϕ and ω scans) and subsequently corrected for Lorentz, polarization and absorption effects on the basis of indexed crystal faces.[31,32] Structure solution was performed with direct methods for $LiGa_2$ and $Li_{11}Ga_{24}$,[?] whereas the starting parameters for structure refinement of $LiGa_6$ were taken from Rietveld refinement (see Table 2.10). Structure refinements on F^2 were performed with full-matrix least-squares cycles and anisotropic treatment of all atoms.[?]

Table 2.10: Results of a Rietveld refinement on $LiGa_6$, structure solution was performed by charge flipping.[28] Graphical refinement results are shown in Figure 2.13.

Composition		$LiGa_6$
Crystal system		trigonal
Space group		$R\bar{3}c$, No. 167
Formula units	Z	6
Latt. param. / Å, Å^3	a	6.18743(8)
	c	23.4704(3)
	V	778.165(9)
Radiation		Cu-Kα1
Wavelength / Å	λ	1.54060
Data range / ^{o}	2ϑ	5.0 – 92.77
Step size / ^{o}	$\Delta 2\vartheta$	0.015
Abs. coeff. / mm^{-1}	μ	33.267
Data points		5852
Backgrd. function		shifted Chebyshev
Backgrd. param.		18
Struct. param.		47
R values / %	R_P	5.890
	R_{wP}	7.944
	R_{exp}	7.929
	R_I	1.534
GooF		1.002

Differential scanning calorimetry (DSC)

Prereacted samples for DSC measurements (typically 40–70 mg) were sealed in small tantalum ampules (∅: 5 mm) by arc-welding under argon and, for better footing and thermal contact, placed in Pt crucibles. The measurements were performed on a STA 449 F5 Jupiter (Netzsch, Selb, Germany) with a DSC Sensor type S. Data were collected from room temperature to 1073 K in most cases, heating and cooling was repeated twice at least. Data evaluation was performed with the Netzsch software package Proton.[34]

DFT calculations

Calculations of the electronic structures were performed with DFT methods for $LiGa_6$, $LiGa_2$ and, for comparison, also for LiGa and an ordered model of $Li_{6-x}Ga_{14}$ with all Li positions fully occupied, resulting in the composition 'Li_6Ga_{14}'. The calculations of the densities of states (DOS) were performed with the program package Wien2K[35] ($LiGa_6$, 'Li_6Ga_{14}' and LiGa) or with the VASP package[36] ($LiGa_2$). Parameters for the calculations of the electronic structures are compiled in Table 2.11.

Table 2.11: Details on the calculations of the electronic structures of $LiGa_6$, 'Li_6Ga_{14}', $LiGa_2$ and LiGa, see also Figure 2.23. $R_{mt}{\cdot}K_{max}$ was set to 8 in all cases. Muffin-tin radii were set to 2.36 Å (Ga) and 2.30 Å (Li), the separation energy was set to −6 Ry.

Phase	Program	Functionals	Monkhorst-Pack grid[39]
$LiGa_6$	WIEN2k[35]	GGA-PBE[37,38]	13x13x13
'Li_6Ga_{14}'	WIEN2k[35]	GGA-PBE[37,38]	7x7x7
$LiGa_2$	VASP[36]	meta-GGA, Becke-Johnson[40]	10x8x10
LiGa	WIEN2k[35]	GGA-PBE[37,38]	13x13x13

Electric conductivity measurements

The powdered compounds were cold-pressed to pellets of 1 mm thickness and 4 mm diameter inside an argon-filled glovebox. Contacts were fixed with conducting silver varnish in a standard four-point van-der-Pauw geometry. Temperature-dependent resisitivity measurements were carried out in a home-built susceptometer with He cryostat.[41]

2.3.4 Results and Discussion

Crystal structure of $LiGa_6$

Traces of $LiGa_6$ were first observed as a byphase in the product mixture of samples aimed at the preparation of $Li_{6-x}Ga_{14}$. Until now, $LiGa_6$ is the Ga-richest phase in the Li–Ga system. We observed its formation during electrolysis of a solution of LiI in N,N-Dimethylformamide (DMF) at a liquid Ga cathode. This electrocrystallization method previously had proven successful for the synthesis of intermetallics.[42] Next to reflections belonging to $Li_{6-x}Ga_{14}$ and LiGa weak reflections were found in the respective X-ray powder diagrams which could not be indexed with any of the known Li–Ga phases (see Figure 2.13). Higher contents of the new, unknown phase were obtained in subsequent thermochemical syntheses of $Li_{6-x}Ga_{14}$ from the elements in tantalum ampules (see Table 2.9). Single crystals suitable for structure analysis were isolated from one of these samples. By optimizing the reaction conditions and with the knowledge of the actual composition, phase-pure samples (on the basis of powder diffraction patterns) could be synthesized. In order to avoid the occurrence of Ga-poorer impurities, a small excess of Ga ($\approx 2\%$) was used in syntheses (see Tab. 2.9), resulting in a very thin film of liquid Ga covering the single crystals. The poor value of R_{int} (see Table 2.12) results from the difficulty of accounting for this Ga film during absorption correction.

Prior to our studies, $LiGa_6$ was observed only once in thermoanalytical studies[24], and its peritectic decomposition temperature was given as 347 K. We found the decomposition to occur at 353 K (see Table 2.15). Tempering stoichiometric mixtures after heating to melt and fast cooling below this temperature for longer times (see Table 2.9) yielded samples with only minor impurities (see Figure 2.13).

For single crystal structure analysis a xenomorphic fragment was centered on a Bruker D8 Quest diffractometer (Bruker AXS, Karlsruhe, Germany) and the intensities of a full Ewald sphere were collected in combined ω and φ scans using MoKα radiation. After correction with respect to Lorentz, polarisation and absorption effects (multi-scan),[32] the extinction conditions *hkl*: only observed for -*h*+*k*+*l*=3*n* and 0*kl*, *h*0*l* and 00*l*: only observed for *l*=2*n* together with the Wilson statistics pointed towards space group $R\bar{3}c$. The structure model derived from a powder structure solution performed with the charge flipping algorithm[28] and subsequent Rietveld refinement (see Table 2.10 and Figure 2.13) was taken as starting parameters for the single crystal structure refinement with anisotropic treatment of all thermal displacement parameters. The reverse/obverse twin law was taken into account but did not yield a meaningful volume fraction for the obverse case within the standard deviation. No twin refinement therefore was considered in the final refinement cycles.

$LiGa_6$ crystallizes with a new structure type in the trigonal space group $R\bar{3}c$ (No. 167) with a = 6.1851(8) Å, c = 23.467(4) Å and Z = 6. For further details on crystallographic parameters, data collection and refinement see Table 2.12. Standardized atomic parameters together with equivalent isotropic thermal displacement parameters are compiled in Table 2.13.

Table 2.12: Crystallographic data and details on data collection and treatment, structure solution and refinement of $LiGa_6$, $LiGa_2$ and $Li_{11}Ga_{24}$ as results from single crystal X-ray diffraction. All measurements were performed at room temperature.

Empiric composition		$LiGa_6$	$LiGa_2$	$Li_{11}Ga_{24.05(4)}$
Crystal system		trigonal	orthorhombic	hexagonal
Space group		$R\bar{3}c$ (No. 167)	$Cmce$ (No. 64)	$P6_3mc$ (No. 186)
Lattice parameters /Å, Å^3	a	6.1851(8)	8.5167(7)	13.7700(19)
	b		14.4826(11)	
	c	23.467(4)	15.2959(14)	23.250(5)
	V	777.5(2)	1886.7(3)	3817.9(13)
Formula units	Z	6	36	6
Calculated density /g · cm^{-3}	ρ	5.450	4.638	4.587
Absorption coefficient /mm^{-1}	μ	30.563	25.192	25.018
Diffractometer		—D8 Quest, Bruker AXS—		
Radiation, wavelength /Å	λ	—MoKα, 0.71073—		
Corrections		—Lorentz, polarization, absorption (multi-scan) [32]—		
Data range /°	$\vartheta_{min/max}$	4.2 / 25.0	2.7 / 25.0	2.4 / 32.5
Index range	$h_{min/max}$	−7 / 7	−10 / 10	−20 / 20
	$k_{min/max}$	−7 / 7	−17 / 17	−20 / 20
	$l_{min/max}$	−27 / 26	−18 / 18	−35 / 35
No. of observed reflections		3847	26542	157015
No. of independent reflections		158	890	5109
No. of indep. refl. with ($I \geq 2\sigma(I)$)		149	888	4554
R_{int} / R_σ		0.1054 / 0.0272	0.0334 / 0.0114	0.0489 / 0.0131
F(000)		1134	2340	4842
Structure solution		none*)	—direct methods [33]—	
Structure refinement		—full-matrix least squares on F^2 [33]—		
No. of l. s. parameters		12	59	206
No. of constraints/restraints		0/0	0/0	0/1
R values (for $I \geq 2\sigma(I)$)	R_1	0.0264	0.1065	0.0277
	wR_2	0.0587	0.2630	0.0545
R values (all data)	R_1	0.0281	0.1065	0.0339
	wR_2	0.0594	0.2630	0.0566
GooF on F^2		1.214	1.293	1.083
Residual electron density /e$^-$·Å^{-3}	$\rho^{e^-}_{min/max}$	−0.58 / 0.75	−1.96 / 1.71	−1.77 / 1.72
Depository number		CSD-433408	CSD-1988079	CSD-1988064

*) Starting values for refinement were taken from the results of a Rietveld refinement, see Table 2.10.

Table 2.13: Standardized fractional atomic coordinates[46], occupation factors, Wyckoff letters, site symmetry and (equivalent) isotropic thermal displacement parameters $U_{\mathrm{iso/equiv}}$ (in Å^2) for $LiGa_6$, $Li_{11}Ga_{24}$ and $LiGa_2$. All standard deviations are given in units of the last digits in parentheses.

Atom	Occupation factor	Wyckoff letter	Site symmetry	x	y	z	$U_{\mathrm{iso/equiv}}$
			$LiGa_6$				
Li1	1	6*a*	32	0	0	1/4	0.0177(7)
Ga1	1	36*f*	1	0.05878(16)	0.27982(16)	0.13533(3)	0.037(7)
			$LiGa_2$				
Li1	1	16*g*	1	0.289(6)	0.239(4)	0.090(3)	0.012(11)
Li2	1	4*a*	2/*m*..	0	0	0	0.020(15)
Li3	1	8*f*	*m*..	0	0.016(9)	0.276(8)	0.05(3)
Li4	1	8*e*	.2.	1/4	0.401(12)	1/4	0.07(4)
Ga1	1	8*f*	*m*..	0	0.1647(4)	0.0223(3)	0.0097(13)
Ga2	1	16*g*	1	0.1575(4)	0.0581(2)	0.1294(2)	0.0114(10)
Ga3	1	8*f*	*m*..	0	0.3982(4)	0.3606(3)	0.0108(13)
Ga4	1	16*g*	1	0.2368(4)	0.4184(2)	0.0382(2)	0.0110(10)
Ga5	1	8*f*	*m*..	0	0.3270(4)	0.0871(3)	0.0105(14)
Ga6	1	8*f*	*m*..	0	0.2617(4)	0.2476(4)	0.0155(13)
Ga7	1	8*e*	.2.	1/4	0.1630(4)	1/4	0.0180(14)
			$Li_{11}Ga_{24}$				
Li1	1	12*d*	1	0.050(2)	0.339(2)	0.2466(9)	0.022(4)
Li2	1	12*d*	1	0.341(3)	0.046(3)	0.3716(13)	0.052(9)
Li3	1	6*c*	.*m*.	0.1335(13)	$-x$	0.4558(14)	0.018(6)
Li4	1	6*c*	.*m*.	0.4512(12)	$-x$	0.1922(12)	0.024(6)
Li5	1	6*c*	.*m*.	0.5394(15)	$-x$	0.4266(16)	0.040(9)
Li6	1	6*c*	.*m*.	0.552(2)	$-x$	0.055(6)	0.014(2)
Li7	1	6*c*	.*m*.	0.7880(8)	$-x$	0.062(4)	0.040(4)
Li8	1	6*c*	.*m*.	0.869(2)	$-x$	0.169(3)	0.057(13)
Li9	1	2*b*	3*m*.	1/3	2/3	0.3785(11)	0.007(4)
Li10	1	2*a*	3*m*.	0	0	0.0000(14)	0.019(6)
Li11	1	2*b*	3*m*.	1/3	2/3	0.24661(12)	0.007(5)
Ga11	1	6*c*	.*m*.	0.20919(10)	$-x$	0.35330(10)	0.0170(4)
Ga12	1	6*c*	.*m*.	0.26929(10)	$-x$	0.26246(10)	0.0176(5)
Ga13	0.650(3)	6*c*	.*m*.	0.45059(18)	$-x$	0.3341(2)	0.0239(8)
Ga14	1	12*d*	1	0.14416(14)	0.48072(13)	0.44674(7)	0.0175(3)
Ga15	0.573(6)	2*b*	3*m*.	1/3	2/3	0.5067(3)	0.0175(13)
Ga21	1	6*c*	.*m*.	0.73030(9)	$-x$	0.36116(9)	0.0141(4)
Ga22	1	6*c*	.*m*.	0.79077(9)	$-x$	0.27127(9)	0.0146(4)
Ga23	0.650(3)	6*c*	.*m*.	0.5489(2)	$-x$	0.2908(2)	0.0194(7)
Ga24	1	12*d*	1	0.47918(12)	0.14379(13)	0.17809(7)	0.0154(3)
Ga25	0.573(6)	2*b*	3*m*.	1/3	2/3	0.6182(4)	0.0292(19)
Ga1	0.80(2)	2*b*	3*m*.	1/3	2/3	0.1171(2)	0.0158(14)
Ga2	0.94(2)	2*b*	3*m*.	1/3	2/3	0.0085(2)	0.0201(13)
Ga3	1	6*c*	.*m*.	0.89496(10)	$-x$	0.28920(12)	0.0280(5)
Ga4	0.778(11)	6*c*	.*m*.	0.06143(12)	$-x$	0.23225(14)	0.0182(9)
Ga5	0.921(12)	6*c*	.*m*.	0.93761(12)	$-x$	0.39326(13)	0.0255(8)
Ga6	1	6*c*	.*m*.	0.10598(10)	$-x$	0.32990(13)	0.0295(6)
Ga8	0.087(5)	6*c*	.*m*.	0.4351(8)	$-x$	0.0582(17)	0.037(5)
Ga1A	0.860(2)	6*c*	.*m*.	0.76485(11)	$-x$	0.46682(11)	0.0130(4)
Ga2A	1	6*c*	.*m*.	0.23497(12)	$-x$	0.15875(11)	0.0238(5)
Ga3A	1	12*d*	1	0.02377(14)	0.36496(15)	0.00524(7)	0.0210(3)
Ga4A	0.860(2)	12*d*	1	0.02519(15)	0.36588(15)	0.11818(7)	0.0151(3)
Ga5A	0.860(2)	6*c*	.*m*.	0.12573(11)	$-x$	0.15010(11)	0.0161(5)
Ga6A	0.860(2)	6*c*	.*m*.	0.87425(12)	$-x$	0.47473(10)	0.0155(5)
Ga7A	0.860(2)	12*d*	1	0.18963(9)	0.00474(10)	0.06178(12)	0.0159(2)
Ga1B	0.140(2)	6*c*	.*m*.	0.7906(4)	$-x$	0.4615(3)	0.0130(4)
Ga2B	0.070(9)	12*d*	1	0.1450(10)	0.4803(10)	0.0612(17)	0.028(2)
Ga2C	0.070(9)	12*d*	1	0.1778(11)	0.5049(11)	0.0692(8)	0.028(2)
Ga4B	0.140(2)	12*d*	1	0.0084(5)	0.3172(6)	0.1274(3)	0.0151(3)
Ga7B	0.140(2)	12*d*	1	0.1733(9)	0.0080(8)	0.0740(4)	0.0159(2)

The crystal structure contains one crystallographic site for Li with point symmetry 32 and a single Ga site with point symmetry 1. The Ga atoms form cages with 18 vertices around the Li atoms, see Figure 2.14. The Li-centered [Ga_{18}] polyhedron is a hexagonal prism with both hexagonal faces augmented by triangles (elongated triangular gyrobicupola, Johnson polyhedron J_{36}). In the structure of $LiGa_6$, this polyhedron has point symmetry 32, whereas its ideal shape would have point symmetry $\bar{3}2/m1$ (= D_{3d}). The distortions allow for a variation of the Ga–Ga distances (see also Figure 2.19) over a rather large range: The distance between the two different hexagons is shortest with 2.508(1) Å, the distances between the capping triangles and the hexagons are 2.589(1) Å. Within the triangles the Ga atoms have a distance of 2.739(1) Å, and within one hexagon two very different Ga–Ga distances (2.739(1) and 3.691(1) Å) can be found. The diagonals of the square faces of the hexagonal prism are rather long with 3.983(1) and 4.106 Å. In the squares between the hexagons and the triangles one diagonal appears rather short with 2.829(1) Å and the other one very long with 4.517(1) Å. Li–Ga distances range from 2.8786(8) to 3.8062(8) Å and thus are larger than the sum of the metallic radii (1.52 Å for Li and 1.35 Å for Ga).[29] The shortest distance between two Li atoms is 5.2961(6) Å. The rhombohedral packing of the [Li@Ga_{18}] polyhedra is not space filling. Small empty interstices in the shape of [Ga_{12}] polyhedra constructed from an oblate octahedron with two triangular caps complete the packing. In Figure 2.14 as projection of the unit cell, the two Ga polyhedra types and their space filling packing are shown. Details of the [Ga_{18}] polyhedron can be found in Figure 2.15.

The 18-vertex Johnson polyhedron J_{36}, an elongated triangular gyrobicupola, is to our knowledge unique: *Pearson Data Base*[59] lists 4688 entries belonging to 3016 different compounds adopting 821 different structure types in which at least one of the atoms shows coordination number 18. For all these only two types of coordination polyhedra are listed: the eight equatorial capped pentagonal prism (2896 entries) and the sixcapped hexagonal prism (958 entries). The most prominent representatives are the $CaCu_5$ structure type (six-capped hexagonal prism Ca@[Cu_{18}]), the PbFCl structure type (eight equatorial capped pentagonal prism Cl@[$Pb_6F_4Cl_8$]), the TiNiSi structure type (eight equatorial capped pentagonal prism Ti@[$Ti_6Ni_6Si_6$]), the ZrNiAl structure type (eight equatorial capped pentagonal prism Zr@[$Zr_6Ni_6Al_6$]) and the Ce_2O_2S structure type (eight equatorial capped pentagonal prism S@[$Ce_6O_6S_6$]).

The crystal structure of $LiGa_6$ can, in an alternative description, be rationalized by a net representation. Perpendicular to the trigonal c axis, the crystal structure can be cut into perfectly flat nets at heights $z \approx 0.135 + n/12$ for the Ga and $1/4 + m/6$ for the Li atoms (with $n = 1 - 11$ and $m = 1 - 5$), see Figure 2.14. In order to describe the whole structure only one type of Ga and one type of Li net are sufficient. The hexagonal Li nets are stacked in a doubled cubic ...ABCABC... periodicity within one unit cell. The Ga nets consist of six- and three-membered rings in a distorted Kagomé-type arrangement with all six-membered rings equal but two different sizes for the three-membered rings occur. The six-membered rings form the hexagonal prism when stacked according to aa' or bb' and the large triangles form the augmenting triangular faces when stacked according to a'b or ab'. The trigonal prisms of the empty [Ga_{12}] polyhedra are the consequence of aa' or bb'

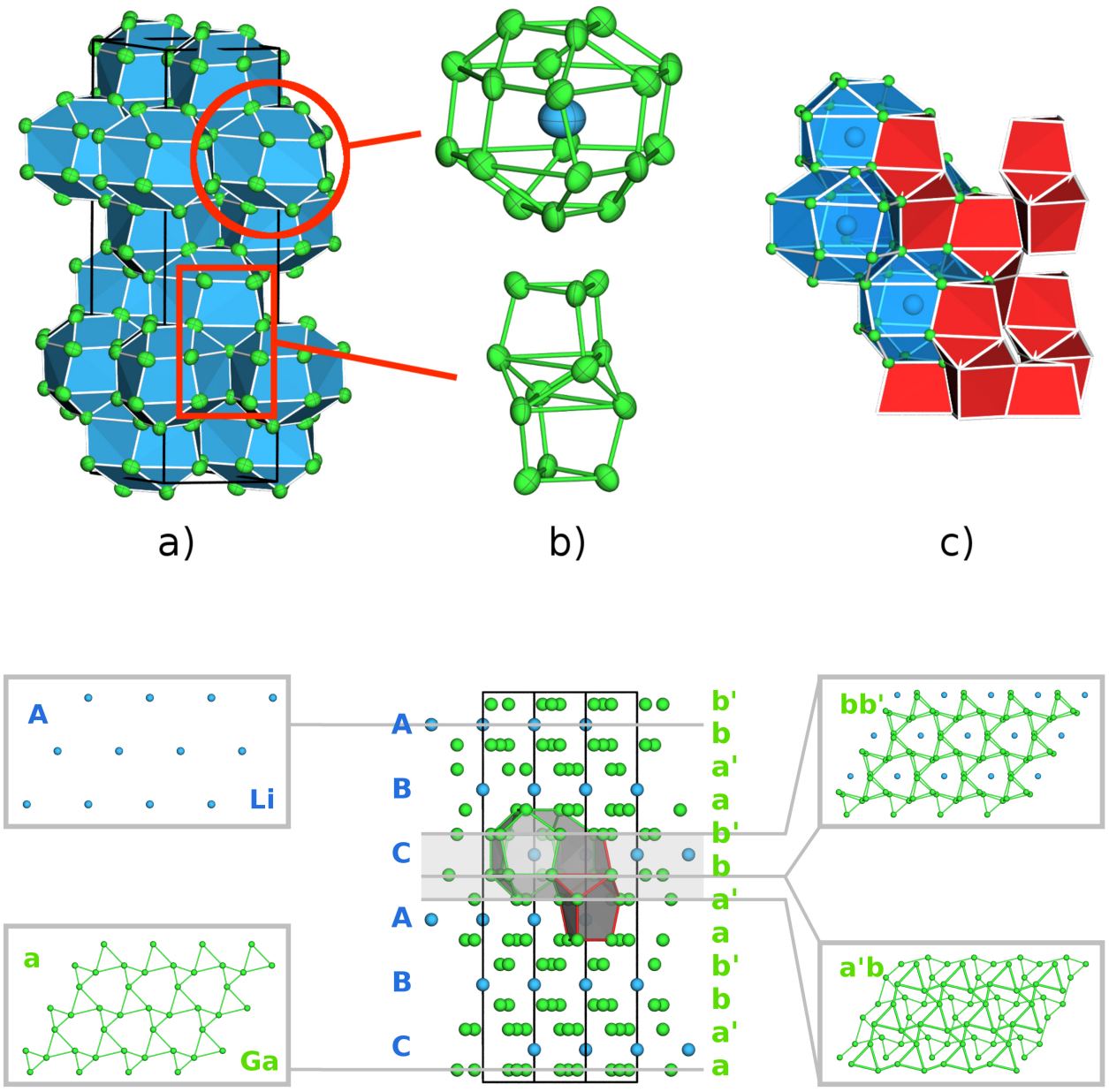

Figure 2.14: Crystal structure of $LiGa_6$. Ga: green, Li: blue. All atoms are depicted with their anisotropic thermal ellipsoids drawn at a probability level of 99%. Upper part: a) projection of the trigonal unit cell with c pointing upwards, b) coordination of Li in a $[Ga_{18}]$ polyhedron (top) and empty $[Ga_{12}]$ polyhedra (bottom) which together form a space filling packing c). Lower part: The packing of the atoms can be represented by one type of Ga and one type of Li nets and their stacking perpendicular to c with the stacking sequence aa'bb' for the Ga nets and ABC for the Li nets. The individual nets have the z coordinates $\approx 0.135 + n/12$ (Ga atoms) and $1/4 + m/6$, respectively.

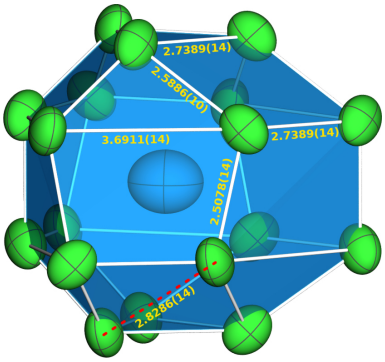

Atom 1	Atom 2	distance
Li(1)	Li(1)	5.2961(6)
	Ga(1)	2.8786(8)
		3.1206(8)
		3.8062(8)
Ga(1)	Ga(1)	2.5078(14)
		2.5886(10)
		2.7389(14)
		2.8286(14)
		3.6911(14)

Figure 2.15: Selected interatomar distances in $LiGa_6$ in Å. All standard deviations are given in parentheses in units of the last digit. [$LiGa_{18}$] polyhedron in $LiGa_6$ with interatomic distances in Å. Ga: green ellipsoids, Li: blue ellipsoid. All ellipsoids are drawn at a 99% probability level.

stacking, the oblate octahedra accordingly from an a'b or ab' stacking. Distances of layers aa and bb are larger than distances of layers a'b and ab'. The octahedra are formed by larger triangles, the prisms include the small triangles. The two sequences are mixed to result in a ...aa'bb'... stacking, tripled within one crystallographic translational period along *c*, see Figure 2.14. With this, the crystal structure of $LiGa_6$ can be constructed from two types of nets, one containing all Li atoms and adopting a cubic stacking periodicity, the other containing all Ga atoms and adopting a hexagonal stacking periodicity. Combining them in the simplest way requires a rhombohedral structure with doubled cubic and a tripled hexagonal periodicity as least common multiple.

Crystal structure of $LiGa_2$

$LiGa_2$ was first observed in rapidly cooled samples with composition Li:Ga = 1:3 as a minority phase together with $LiGa_{3.42}$ and Li_3Ga_{14}. To increase volume fraction and crystal quality for this phase, the sample was tempered below its peritectic decomposition point of 603 K (cf. Table 2.9, Table 2.15, Figure 2.16 and Figure 2.21).

A phase with composition $LiGa_2$ was first proposed by Yatsenko[18] as a result of thermoanalytical studies, however, it has been neglected in the newest phase diagram (see Figure 2.12) and the phase Li_5Ga_9 seemingly was included instead.[27] $LiGa_2$ adopts a new structure type with orthorhombic metric in space group *Cmce* (No. 64) and lattice parameters $a = 8.5167(7)$ Å, $b = 14.4826(11)$ Å, $c = 15.2959(14)$ Å with $Z = 36$.

It has been observed on many specimens that $LiGa_2$ forms epitaxial intergrowth crystals together with the Ga-richer phase $Li_{6-x}Ga_{14}$. This is due to very similar unit cell metrics: $Li_{6-x}Ga_{14}$ crystallizes with space group $R\bar{3}m$ and lattice parameters $a = 8.4626(1)$ and $c = 16.8470(3)$ Å,[19] whereas the orthorhombic *C*-centered metric of $LiGa_2$ can be transformed in a pseudo-hexagonal primitive cell with $a_{\psi\text{hexP}} = a_{\text{orthoC}} = 8.520$ Å and also $a_{\psi\text{hexP}} = \frac{1}{2}\cdot(a \times b_{\text{orthoC}}) = 8.384$ Å, with $c_{\psi\text{hex}} = c_{\text{orthoC}} = 15.292$ Å and $\gamma_{\psi\text{hex}} = 120.5^{\circ}$. The mean pseudo-hexagonal *a* parameter would

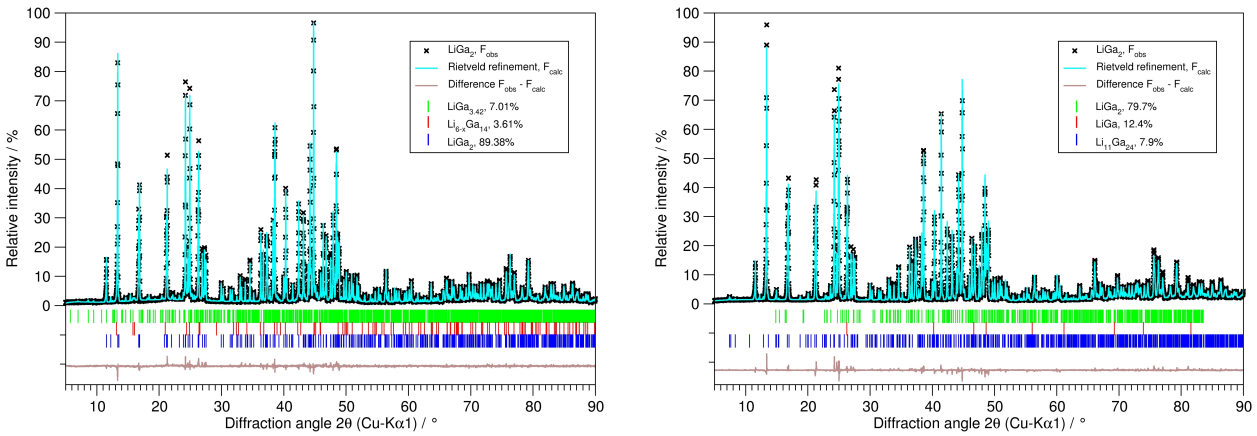

Figure 2.16: Left: Rietveld refinement of a powder sample with highest $LiGa_2$ content after optimizing the synthetic parameters. Right: Rietveld refinement of a powder sample with $LiGa_2$ as the main component and $Li_{11}Ga_{24}$ as byphase.

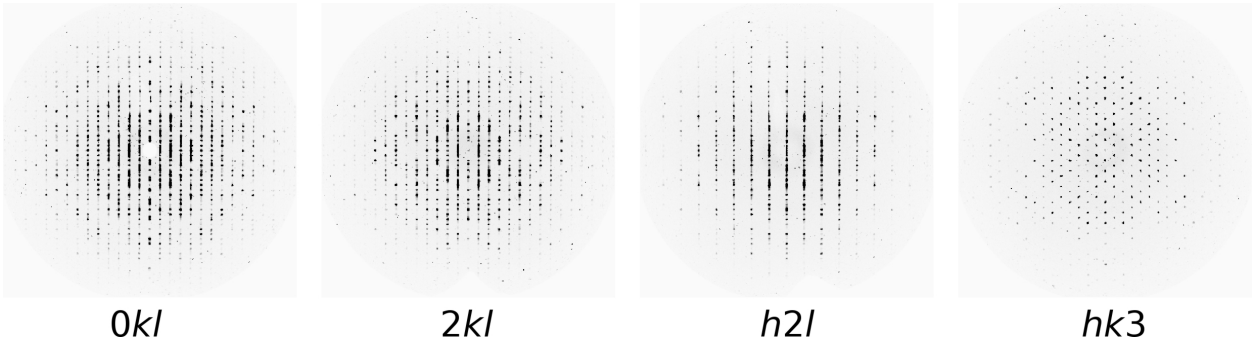

Figure 2.17: Selected diffraction patterns of $LiGa_2$. The diffuse intensities along l can be explained with epitaxial intergrowth of $LiGa_2$ with $Li_{6-x}Ga_{14}$ due to similar metrics (see text). In the $hk3$ pattern the pseudo-hexagonal metric becomes obvious.

be 8.452 Å which differs only by 0.1% from the one of $Li_{6-x}Ga_{14}$, and the distortion of $\gamma_{\psi hex}$ from an ideal 120° angle also is very small. The consequence is a two-dimensional statistical intergrowth of slabs of both phases with randomly varying thicknesses. This two-dimensional disorder causes diffuse streaks along l in the diffraction patterns and a clearly visible pseudo-hexagonal a^*b^* plane, see Figure 2.17.

A large number of observed weak intensities which should be systematically absent are caused by the presence of the second phase $Li_{6-x}Ga_{14}$. As a consequence, several flaws in the refinement of the $LiGa_2$ model (see Table 2.12) result, together with poor values for $R1$ and especially for $wR2$, whereas the values for R_{int} and R_σ are rather good. In Rietveld refinements including the impurity phases this problem can be overcome, see Figure 2.22 (Sample D), where the structural parameters from the single crystal model were taken as starting values. Results of the Rietveld refinement of $LiGa_2$ from a sample containing a mixture of ca. 1:1 LiGa and $LiGa_2$ and very minor traces of $Li_{6-x}Ga_{14}$ is presented in Table 2.14.

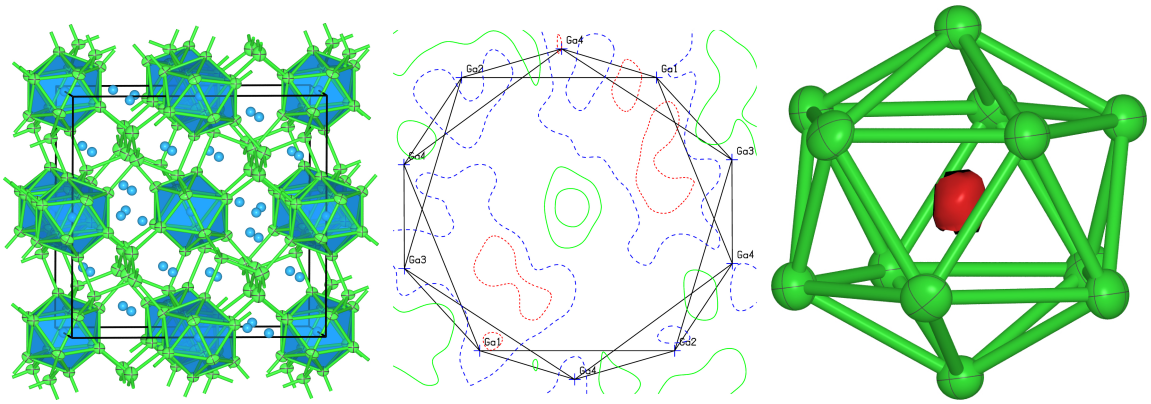

Figure 2.18: Crystal structure of $LiGa_2$. Left: unit cell with b pointing upwards and c to the right. Icosahedra [Li@Ga_{12}] centered by Li are drawn as blue polyhedra, Ga atoms are shown as green ellipsoids with 99% probability level, Li atoms are drawn as blue spheres. Center and right: Two representations of the difference electron density map (red) in the center of the [Li@Ga_{12}] icosahedron attributed to atomic position of Li2.[29,44,45] Two-dimensional plot with isolines drawn for electron density of 1 $e^-/Å^3$, and plot of a 3D hypersurface of the electron density at a level of 2.0 $e^-/Å^3$

We attempted to solve the epitaxial intergrowth problem by tempering the samples at a temperature below the peritectic decomposition temperature of $LiGa_2$ and above the one of $Li_{6-x}Ga_{14}$ (603 and 573 K, respectively, see Table 2.15). This reduced the $Li_{6-x}Ga_{14}$ content considerably, however, its decomposition remained incomplete, most probably due to kinetic effects. The structural model we present here could be established from the tempered single crystalline samples with sufficient accuracy to allow for a discussion of geometric details. The precision of the model from Rietveld refinement is only slightly higher than the one from single crystal data and to achieve convergence all Ga atoms and all Li atoms were refined with one common isotropic displacement parameter per atom type.

Only Ga atoms could be refined with anisotropic treatment of the thermal displacement parameters while the lithium atomic positions were all described with isotropic thermal displacement parameters.

The crystal structure of $LiGa_2$ is built from four crystallographic Li sites and a Ga network consisting of seven crystallographic sites arranged in [Ga_{12}] icosahedra with point symmetry $2/m$ interconnected by tetravalent Ga atoms, forming either planar zigzag chains or single Ga atoms interconnecting the chains and the icosahedra. The different Lithium sites either center the [Li@Ga_{12}] icosahedra or fill interstices of the Ga network, see Figure 2.18. The [Li@Ga_{12}] icosahedra show exo-bonding from all vertices and are arranged in

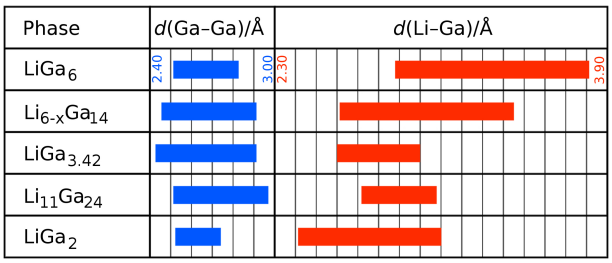

Figure 2.19: Interatomic distances in Ga-rich lithium gallides as results from single crystal refinements. Data for $Li_{6-x}Ga_{14}$ and for $LiGa_{3.42}$ were taken from literature.[19,23]

a fcc topology. This underlying pseudo-cubic metric can be discerned in the orthorhombic unit cell when doubling the *a* axis: the pseudo-cubic fcc cell has the axes $a_{\psi\mathrm{cub}} = 2a_{\mathrm{ortho}} = 17.008$ Å, and the deviation of the three pseudo-cubic axes is at maximum 9% from the mean value of 15.588Å.

The interatomic Ga–Ga distances differ beween the atoms belonging to [Ga_{12}] icosahedra, the zigzag-chains and the single Ga atoms linking the icosahedra and the zigzag chains. The shortest contacts are the Ga–Ga distances between the single Ga atom (Ga5, see Table 2.13) and the icosahedron consisting of sites Ga1–Ga4 with 2.520 to 2.550 Å, followed by the Ga–Ga distances within the zigzag chain (Ga6, Ga7) with 2.564 Å, and the longest contacts occur within the icosahedra (2.616 to 2.739 Å). Contacts between the single Ga5 atom and the icosahedron (2.626 Å) as well as between the zigzag chain and the icosahedron (2.623) lie in the intermediate range for Ga–Ga distances in intermetallic gallides with high covalent bonding contributions, see also Figure 2.19.

The interatomic Ga–Ga distances differ beween the atoms belonging to [Ga_{12}] icosahedra, the zigzag-chains and the single Ga atoms linking the icosahedra and the zigzag chains. The shortest contacts are the Ga–Ga distances between the single Ga atom (Ga5, see Table 2.13) and the icosahedron consisting of sites Ga1–Ga4 with 2.520 to 2.550 Å, followed by the Ga–Ga distances within the zigzag chain (Ga6, Ga7) with 2.564 Å, and the longest contacts occur within the icosahedra (2.616 to 2.739 Å). Contacts between the single Ga5 atom and the icosahedron (2.626 Å) as well as between the zigzag chain and the icosahedron (2.623) lie in the intermediate range for Ga–Ga distances in intermetallic gallides with high covalent bonding contributions, see also Figure 2.19.

A unique feature of the crystal structure of $LiGa_2$ is the centering of a [Li@Ga_{12}] icosahedron by a Li atom. This has not been observed so far and leads to unexpectedly short distances between Li2 and the surrounding Ga

Table 2.14: Results of a Rietveld refinement on $LiGa_2$ from a sample consisting of a ca. 1:1 mixture of LiGa and $LiGa_2$. Graphical refinement results are shown in Figure 2.22 as Sample D.

Composition		$LiGa_2$
Crystal system		orthorhombic
Space group		*Cmce*, No. 64
Formula units	Z	36
Lattice parameters / Å, Å^3	a	8.5192(4)
	b	14.4380(7)
	c	15.2901(7)
	V	1880.7(3)
Radiation		Cu-Kα1
Wavelength / Å	λ	1.54060
Data range / °	2ϑ	5.0 – 90.0
Step size / °	$\Delta 2\vartheta$	0.015
Absorption coefficient / mm^{-1}	μ	25.2
Data points		5667
Background function		shifted Chebyshev
Background parameters		11
Structural parameters		52
R values / %	R_{P}	10.69
	R_{wP}	14.98
	R_{exp}	13.76
	R_{I}	4.86
GooF		1.093

Atom	Wyck.	x	y	z	U_{iso}
Li1	16*g*	0.324(8)	0.202(6)	0.111(4)	0.119(2)
Li2	4*a*	0	0	0	0.119
Li3	8*f*	0	-0.089(8)	0.193(7)	0.119
Li4	8*e*	1/4	0.389(7)	1/4	0.119
Ga1	8*f*	0	0.1652(3)	0.0219(3)	0.109(2)
Ga2	16*g*	0.1596(4)	0.0575(2)	0.1307(2)	0.109
Ga3	8*f*	0	0.3981(4)	0.3613(3)	0.109
Ga4	16*g*	0.2358(4)	0.4192(2)	0.0383(2)	0.109
Ga5	8*f*	0	0.3271(4)	0.0869(3)	0.109
Ga6	8*f*	0	0.2603(3)	0.2465(3)	0.109
Ga7	8*e*	1/4	0.1636(3)	1/4	0.109

atoms Ga1–Ga4 with 2.405 – 2.600 Å (see Figure 2.19 for comparison). This value is shorter than the sum of the atomic radii (1.52 and 1.35 Å for Li and Ga, respectively),[29] and Li2 can be regarded to have a considerable cationic character from analysis of the electronic structure (see below). The Li–Ga distances for Li1, Li3 and Li4, located in the Ga network, are in the normally observed range between 2.7 and 3.1 Å. In order to check whether the presence of Li2 inside the icosahedron is real or an artefact caused by effects of the epitaxial intergrowth, the difference electron density at this position has been calculated from a model into which the centering Li2 position was not included. Then, at the Li2 position a clear and sharp maximum of electron density can be detected (see Figure 2.18). The height of this maximum is in good agreement with the maxima found at the positions of the other Li positions when treated in a similar manner, hence we must attribute it to a fully occupied Li atom position.

Crystal structure of $Li_{11}Ga_{24}$

$Li_{11}Ga_{24}$ was first obtained as a byphase in samples aimed at the synthesis of pure $LiGa_2$. As the compositions of both phases are very close, $Li_{11}Ga_{24}$ was never obtained in phase-pure form but always accompanied by $LiGa_2$. The highest phase fraction was found in a sample with 7.9% $Li_{11}Ga_{24}$, together with 12.4% of LiGa and 79.7% $LiGa_2$, see Figure 2.16. From this sample, a single crystal could be prepared after a large number of tries as all Li–Ga phases look virtually the same.

$Li_{11}Ga_{24}$ may be identical with one of the phases with composition close to $LiGa_2$ detected in earlier thermoanalytic works, however, its attribution to a specific literature phase must remain unclear. $Li_{11}Ga_{24}$ crystallizes in an own structure type with the non-centrosymmetric hexagonal space group $P6_3mc$ (No. 186) and lattice parameters a = 13.7700(19) and c = 23.250(5) Å (see Table 2.12 for more crystallographic details). A data set was collected showing inversion twinning and refinement of the volume fractions resulted in a 1:1 ratio of the two domains. The crystal structure of $Li_{11}Ga_{24}$ is built from 29 Ga and 11 Li sites (see Table 2.13) and contains $[Ga_{12}]$ icosahedra as well as Li-centered Frank-Kasper $[Li@Ga_{16}]$ polyhedra with 16 vertices and 28 triangular faces (monocapped gyroelongated trigonal cupola). In $Li_{11}Ga_{24}$, other than in $LiGa_2$, the $[Ga_{12}]$ icosahedra are not centered by Li atoms.

The two crystallographically independent $[Li@Ga_{16}]$ Frank-Kasper polyhedra are built from the atomic sites Ga11–Ga15 and Ga21–25 (see Table 2.13) and are centered by Li9 and Li11, respectively. An uncapped gyroelongated triangular cupola is listed as Johnson polyhedron J_{22} and has, equal to its monocapped variant, in its ideal equilateral shape point symmetry $3m$ (= C_{3v}). In the crystal structure of $Li_{11}Ga_{24}$ it is slightly distorted but still has full point symmetry $3m$ which is also the site symmetry of the centering Li atoms, see Table 2.13. The two $[Li(9)@Ga(11\text{-}15)_{16}]$ and $[Li(11)@Ga(21\text{-}25)_{16}]$ polyhedra are topologically identical with Ga–Ga distances ranging from 2.518(3) to 2.966(3) Å and Li–Ga distances of 2.72(15) to 3.08(6) Å (see also Figure 2.19).

The [Ga_{12}] icosahedra can be grouped into two different structural motifs: one icosahedron is formed by the atomic sites Ga3–Ga6 (see Table 2.13). The Ga–Ga distances within this icosahedron range from 2.510(4) to 2.689(2) Å and are in very good agreement with distances found in other [Ga_{12}] icosahedral units but shorter than in the Li-centered icosahedra in $LiGa_2$ (2.62 to 2.74 Å, see Figure 2.19). It is connected to the Frank-Kasper [Li@Ga_{16}] polyhedra via exo bonds. The Ga–Ga distances within these exo-bonds (2.519(3) to 2.521(3) Å) are in the same range than the ones within the icosahedra. The atomic sites Ga1, Ga2 and Ga8–7B (see Table 2.13) form the second

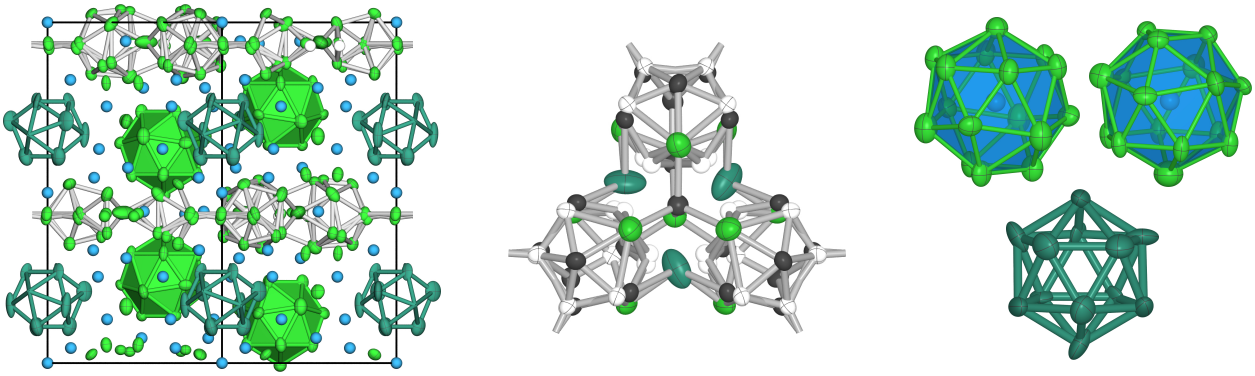

Figure 2.20: Crystal structure of $Li_{11}Ga_{24}$. Left: Projection of the unit cell along (110). [Li@Ga_{16}] Frank-Kasper polyhedra are drawn as green polyhedra, the ordered [Ga_{12}] icosahedra are shown in dark green and the disordered icosahedra triple is drawn with grey Ga–Ga bonds. Li atoms are drawn in blue. All ellipsoids are shown at a 99% probability level. Center: icosahedral triple cluster with disordered Ga atoms. Atoms with full occupation are drawn in light green, atoms with approx. 50% occupation in dark green, atoms with approx. 80% in dark grey and atoms with approx. 20% in light grey. Right: Frank Kasper polyhedra [Li@Ga_{16}]around Li9 (top left) and Li11 (top right) and the [Ga_{12}] icosahedron.

set of icosahedra which shows strong occupational disorder. This group is shown in detail in Figure 2.20. Around a [Ga_2] dumbbell positioned on the threefold axis (Ga1 and Ga2 in Table 2.13) three [Ga_{10}] fragments containing some mutually exclusive pairs of Ga split positions together with some fully occupied Ga positions form a unique cluster unit. The two mutually exclusive sets of atoms show occupation factors of 86 and 14%, thus resulting in an overall full occupation. The disordered threefold icosahedral units are interconnected by Ga–Ga bonds of 2.34 Å to sheets perpendicular to the c axis at height $z = 0.061$. Within the disordered icosahedra, Ga–Ga distances between those sites combining to one icosahedral set of atoms show values between 2.510(4) and 2.68(2) Å which is in very good agreement with those found for the ordered icosahedron described above and other icosahedral [Ga_{12}] units. As this disordered icosahedral group is connected with both the first icosahedron and the Frank-Kasper polyhedra also atomic positions in these building units are affected by occupational disorder as a consequence, see Table 2.13.

The observed disorder phenomena in $Li_{11}Ga_{24}$ may be taken as a hint to formation of a pseudo-hexagonal *drilling* of an orthorhombic structure. In order to resolve the disorder phenomena we transformed the hexagonal model to the orthorhombic C-centered metric according to

$$\begin{pmatrix} a_{\mathrm{ortho}} \\ b_{\mathrm{ortho}} \\ c_{\mathrm{ortho}} \end{pmatrix} = \begin{pmatrix} 1 & 0 & 0 \\ 1 & 2 & 0 \\ 0 & 0 & 1 \end{pmatrix} \cdot \begin{pmatrix} a^1_{\mathrm{hex}} \\ a^2_{\mathrm{hex}} \\ c_{\mathrm{hex}} \end{pmatrix}$$

resulting in a new unit cell with space group $Cmc2_1$, the direct orthorhombic subgroup of $P6_3mc$, and $a_{\mathrm{ortho}} = a_{\mathrm{hex}} = 13.77$ Å, $b_{\mathrm{ortho}} = \sqrt{3} \cdot a_{\mathrm{hex}} = 23.85$ Å and $a_{\mathrm{ortho}} = c_{\mathrm{hex}} = 23.25$ Å. However, the resulting structure model could not resolve the disorder phenomena, also further symmetry reduction to the monoclinic system did not result in an ordered model. This may be due to a small domain size with regard to the coherence length of the radiation, further studies with electron diffraction may help here.

Thermal stabilities, formation and decomposition behavior of the Ga-rich phases in the system Li–Ga

DSC studies have been performed in order to establish phase relations, stabilities and reactivities between the Ga-rich lithium gallides. In Figure 2.21 a compilation of thermal effects, the attributed phases and the stability ranges is given. The attribution of the individual thermal effects was done by comparing the thermal effects observed for five samples A–E and their respective compositions. All of them consisted of mixtures of two phases, the overall composition was determined by Rietveld refinements of the respective X-ray powder diffraction patterns, see Figure 2.22.

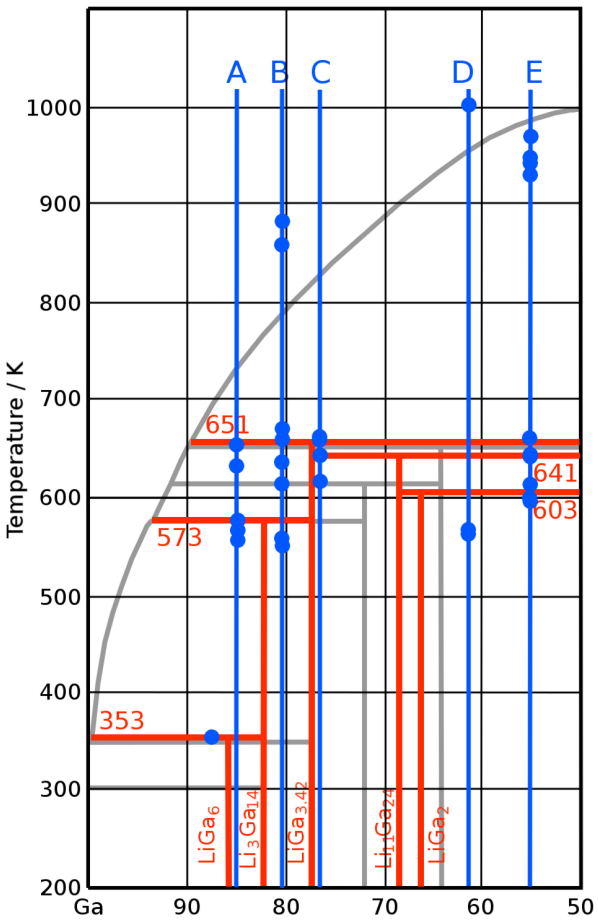

Figure 2.21: Revised phase diagram of the Ga-rich side of the system Li–Ga. Gray lines represent the most actual literature phase diagram after Predel et al[27], blue lines represent the five DSC samples with blue dots marking the individual endothermic effects registered in heating curves, red lines represent the derived stability regions of the individual phases.

Sample A consisted of a mixture of $LiGa_6$ and $Li_{6-x}Ga_{14}$ with phase fractions of 89.3(3) and 10.7(4)%, respectively, resulting in an overall composition of $LiGa_{5.7}$ when assuming x = 3 in $Li_{6-x}Ga_{14}$. $LiGa_6$ decomposes at 353 K which is very close to the reported temperature of 347 K,[24] the endothermal effect occuring at 573 K during the first heating must be caused by the decomposition of $Li_{6-x}Ga_{14}$. This decomposition temperature is attributed to a phase with tentative composition 'Li_2Ga_7' in the Belin phase diagram[24] and later to Li_3Ga_{14} in the Predel phase diagram.[27] A third endothermal effect occurs at 631 K during the first and at 651 K during the second heating. It must consequently be attributed to the decomposition of a phase that forms during the decomposition of $Li_{6-x}Ga_{14}$ which will be shown by the help of sample C to be the next Ga-poorer phase $LiGa_{3.42}$.[23]

Sample B was a mixture of 55.3(4)% $Li_{6-x}Ga_{14}$ and 44.7(5)% $LiGa_2$, resulting in an overall composition of $LiGa_{4.1}$. The heating curves show two strong effects. The decomposition of $Li_{6-x}Ga_{14}$ at a slightly lower temperature than in sample A (561 K) and the decomposition of $LiGa_{3.42}$ at 660 K, again formed as decomposition product of $Li_{6-x}Ga_{14}$. The broad and weak signal at 624 K (first heating) and 595 K (second heating) therefore must be attributed to the decomposition of $LiGa_2$.

Sample C has an overall composition of $LiGa_3$ and contains LiGa and $LiGa_{3.42}$ with phase fractions of 6.5(2) and 93.5(5)%, respectively. A single effect shows in the first heating curve at 647 K and clearly must be attributed to the decomposition of $LiGa_{3.42}$. At second heating, an additional weak signal occurs at 639 K. It belongs to the decomposition of $Li_{11}Ga_{24}$. Also the effect from decomposition of $LiGa_2$ at 605 K can be detected. Both phases must have formed by decomposition of $LiGa_{3.42}$ and reaction of the melt with LiGa.

For sample D the DSC tantalum container was loaded with lithium and gallium in a ratio of 1:1.5 and was not reacted prior to the DSC measurements. The first cycle therefore showed an exothermal reaction signal and the melting point of LiGa at 1005 K which is in rather good agreement with the literature value of 993 K.[27] The subsequent heating cycles show weak endothermal effects at 566 K which originates from the decomposition of $Li_{6-x}Ga_{14}$. This is unexpected as the sample composition and the respective stability ranges of the phases should prevent $Li_{6-x}Ga_{14}$ from forming from a thermodynamical point of view. However, strong kinetic effects can be assumed to occur in the system. We have described above the crystallographic intergrowth of $Li_{6-x}Ga_{14}$ and $LiGa_2$, and the underlying seeding effect may contribute to deviations from the thermodynamically expected phase stabilities. Similar deviations from expected behavior have been detected in samples B and C in which effects from $LiGa_2$ were observed, right outside its stability region, but always in connection with $Li_{6-x}Ga_{14}$. The composition of sample D was determined to be a mixture of LiGa and $LiGa_2$ with 49.6(7)% of LiGa and 50.4(7)% of $LiGa_2$ after the DSC measurements, resulting in an overall composition of $LiGa_{1.5}$.

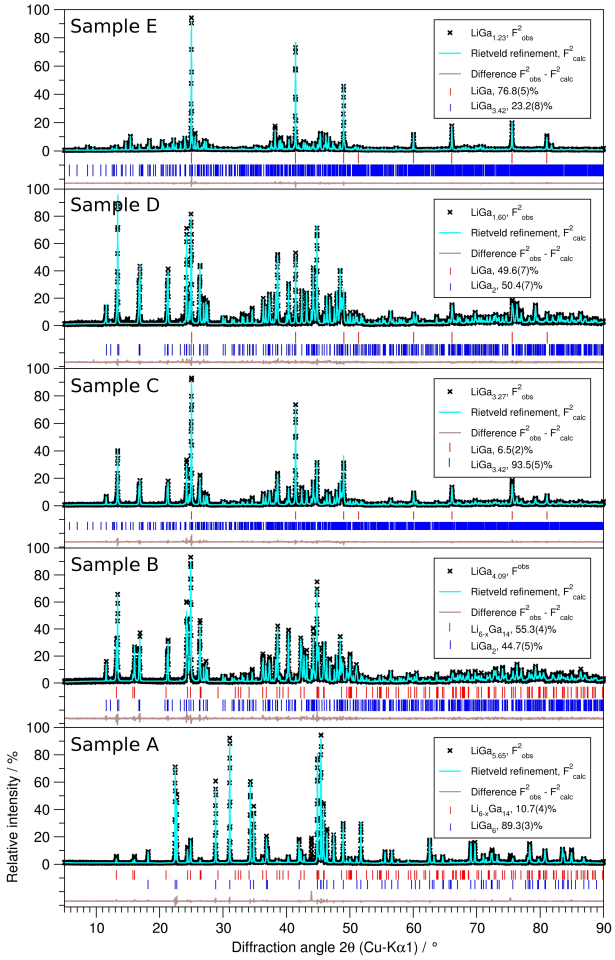

Figure 2.22: Rietveld refinements for the samples A–E to determine the elemental composition after DSC scans.

Also sample E consists of a mixture of LiGa and $LiGa_2$, but the phase fractions of 76.8(5)% LiGa and 23.2(8)% $LiGa_2$ lead to an overall composition of $LiGa_{1.2}$. On heating, the first endothermic effect at 603 K indicates the decomposition of $LiGa_2$. A very weak effect at 642 K originates from the decomposition of $Li_{11}Ga_{24}$, the decomposition product of $LiGa_2$. The strong third effect at 646 K again belongs to $LiGa_{3.42}$ formed by decomposition of $Li_{11}Ga_{24}$. Additional broad effects at around 933 to 953 K originate from crossing the liquidus curve.

Table 2.15: Decomposition temperatures and products for the Ga-rich phases of the binary system Li–Ga as detected in DSC studies. Available literature values[24] are given in parentheses for comparison. All temperatures are given in K. LiGa melts congruently at 1005 K.

Phase	$T_{Peritectic}$	Decomp. products
$LiGa_6$	353 (347)	(L) + $Li_{6-x}Ga_{14}$
$Li_{6-x}Ga_{14}$	573 (573)	(L) + $LiGa_{3.42}$
$LiGa_{3.42}$	654 (646)	(L) + LiGa
$Li_{11}Ga_{24}$	309	$LiGa_{3.42}$ + LiGa
$LiGa_2$	603	$Li_{11}Ga_{24}$ + LiGa

Electronic structures of $LiGa_6$, LiGa and 'Li_6Ga_{14}' and specific electric resistivities

On the basis of the respective single crystal structure models the electronic structures were calculated with standard DFT methods. As a result the densities of states are plotted for LiGa, $LiGa_6$, $LiGa_2$ and the hypothetical compounds 'Li_6Ga_{14}', corresponding to the crystal structure of $Li_{6-x}Ga_{14}$ with fully occupied Li positions are presented in Figure 2.23. The hypothetical structure may differ from the real one mainly in the positioning of the Fermi level. In the fully occupied model it may occur higher in energy, and its real positioning can be assumed to lie closer to or directly within the well-marked pseudo-gap.

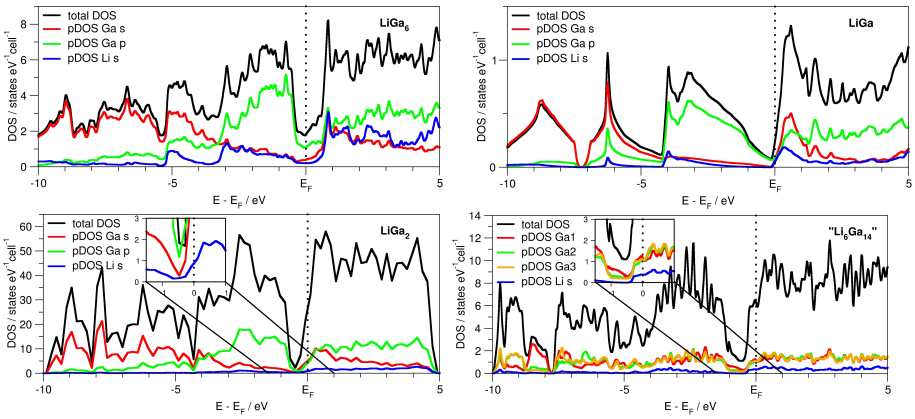

Figure 2.23: DOS curves calculated for (seen from top to bottom) $LiGa_6$, $LiGa_2$, LiGa and the hypothetical compound "Li_6Ga_{14}".

The respective plots of the density of electronic states (DOS) as a function of energy show both similarities and differences for the Ga-rich lithium compounds. All compounds show pronounced local minima of the densities of states at or close to the Fermi energy, as one would expect for intermetallic phases with high Coulombic bonding contributions. As the minima are non-zero in all cases, all lithium gallides are metals. In all cases, the states below the pseudo-gaps are dominated by Ga *p* states, the Li *s* are very low but non-zero, and the states directly above the pseudo-gap show strong mixing of Li *s*, Ga *s* and Ga *p* states. As shown for the example of 'Li_6Ga_{14}', there is no significant difference for the individual crystallographic Ga positions to be found. The bonding situations can be interpreted in the sense of non-classical Zintl behavior with $Ga^{\delta-}$ polarized Ga atoms and lithium atoms $Li^{\delta+}$. The electronic structures differ with respect to the degree of Ga *s* and *p* mixing (*sp* hybridization) and dispersion of the states, reflecting the different amounts

of covalent bonding contributions and sp^3-like bonding as in LiGa versus multi-center bonding in the cluster-containing phases $LiGa_2$, 'Li_6Ga_{14}' and $LiGa_6$. Also the density of states at the Fermi level differs: in $LiGa_6$, the Ga-richest phase, there is a significant number of occupied states found in the pseudo-gap which is only a local minimum. The deepest minima are found for LiGa and $LiGa_2$. Here, also the Li s states are lowest, pointing toward the highest positive polarization. For $Li_{6-x}Ga_{14}$, the most stable configuration seems to be achieved at x in the range of 2–3 which would mean a shift of the position of E_F inside the pseudo-gap. The DOS at Fermi level for LiGa shows rather broad dispersion of the Ga *p* bands and considerable mixing with the *s* states. This corroborates better with the structural description by a coloring variant of a bcc packing than with the textbook Zintl picture of a diamond-like [Ga^-] network embedding Li^+ cations in the interstices. This would call for a more expressed (pseudo-)band gap and very low dispersion of the *sp* states indicating strong covalent two-electron two-center bonding. The cationic character of Li in all four compounds becomees clear as in all cases the pDOS of Li s states shows a minimum at the Fermi level. However, in all cases it is non-zero. The positive polarization may be put in the sequence $LiGa_6 \leq LiGa_2 \leq$ LiGa, 'Li_6Ga_{14}', with increasing value for δ in $Li^{\delta+}$.

From cold-pressed pellets of LiGa, $LiGa_6$ and $Li_{6-x}Ga_{14}$ conductivity measurements with standard four-point van-der-Pauw geometry were performed in the temperature range of 3.5 – 300 K. The kinks in the temperature-resistivity curves for LiGa at ca. 230 K and for $Li_{6-x}Ga_{14}$ at ca. 115 and 280 K may result from contacting problems as structural transitions can be excluded. The conducting silver varnish may not be fully inert towards the Li–Ga phases. As shown in Figure 2.24, all three compounds show metallic behavior as expected from the calculations of the electronic structures. However, the respective specific resistivies differ considerably between the individual compounds. The specific resistivity of Ga is interesting as a point of reference within this context and is reported to be $1.4{\cdot}10^{-7}$ Ω·m at room temperature[47] and was determined to $2.1{\cdot}10^{-7}$ Ω·m in our measurements. This is in the same order of magnitude as found for classical semimetals (As: $2.6 \cdot 10^{-7}$ Ω·m, Sb: $4.1{\cdot}10^{-7}$ Ω·m)[47,48] or 'bad metals' (Hg: $9.6{\cdot}10^{-7}$ Ω·m)[47] and thus one order of magnitude higher than for 'good metals' such as Cu ($1.7 \cdot 10^{-8}$ Ω·m) or Ag ($1.6{\cdot}10^{-7}$ Ω·m).[49] Typical semiconductors (Si: $3.16{\cdot}10^3$ Ω·m, Ge: $4.8{\cdot}10^2$ Ω·m, GaAs: 10^8–10^{-4} Ω·m)[50,51] have much higher specific resistivities. $LiGa_6$ shows a specific resistivity of $1.9{\cdot}10^{-7}$ Ω·m at room temperature which is very close to the one of pure gallium. This corresponds with the DOS calculation results showing the highest number

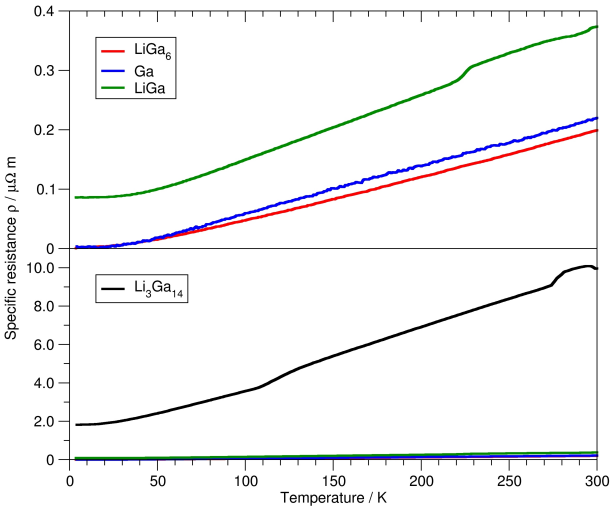

Figure 2.24: Temperature dependence of the resistivity of gallium, LiGa, $LiGa_6$ (upper part) and $Li_{6-x}Ga_{14}$ (lower part, with the three other curves in comparison heating curves shown for all cases.

of electronic states near the Fermi level in comparison to the other lithium gallides. The specific resistivity of LiGa is significantly higher with $3.7 \cdot 10^{-7}$ Ω·m, again in accordance with the calculations of the electronic structure. For $Li_{6-x}Ga_{14}$, the specific resistivity is higher by one order of magnitude and was recorded to be $9.8 \cdot 10^{-6}$ Ω·m. This corroborates the DOS interpretation of a bonding situation with a much lower free charge carrier concentration due to high ionic and covalent bonding contributions and electron localization. It would be interesting to know the specific resistivity of $LiGa_2$ as well for comparison, however, no phase-pure samples of this compound are available. All three phases show linear temperature dependence of the specific electronic resistivity over the whole temperature range. Other highly polar intermetallic phases such as e. g. amalgams of the less noble metals[52–54] show a deviation from linear temperature behavior and a resistivity saturation according to the Ioffe-Regel law.[55–57] This 'bad metal behavior'[58] occurs at very low charge carrier concentrations and very short mean free path lengths caused by strong Coulombic potentials. In Ga-rich lithium gallides the Coulombic polarity seems to be pronounced but not very high in comparison to other polar intermetallics.

2.3.5 Conclusion

The new Ga-rich lithium gallides $LiGa_6$, $Li_{11}Ga_{24}$ and $LiGa_2$ are metallic phases which do not, in contrast to many gallides of the heavier alkali metals, follow the Zintl-Klemm-Busmann concept. This concept is often broken when either electronegative elements left of the Zintl border are involved or when lithium takes the role of the electropositive element. Then, so-called non-classical Zintl phases can be observed.[60] In lithium gallides both prerequisites are fulfilled. Ga-rich gallides show $[Ga_n]^{\delta-}$ clusters with covalent Ga–Ga bonding as typical structural elements. Non-classical Zintl phases show a high electronegativity difference between the bonding partners but, in contrast to classical Zintl phases, only partial electron transfer and consequently metallic conductivity. They are therefore examples for intermetallic phases with the interesting bonding situation of 'polar metals'. The degree of Coulombic polarization varies with the Ga content as can be derived from DOS calculations and specific resistivities. A pronounced minimum of the DOS at Fermi level together with resistivities spanning over a range of two orders of magnitude shows differences in electron transfer between the individual phases and indicates low carrier concentrations.

The crystal structure of $LiGa_6$ represents a new structure type for a binary main group compound. It is built from two crystallographic sites, one for Li and one for Ga, and this simple structure contains a coordination polyhedron for Li which has to be emphasized as a new structural motif in solid state chemistry.

The two compounds $LiGa_2$ and $Li_{11}Ga_{24}$ have very close composition and some common structural features. Again, they represent new crystal structure types. The $[Ga_n]$ polyhedra occuring in these structures, however, are well-known: $[Ga_{12}]$ icosahedra and $[Ga_{16}]$ Frank-Kasper polyhedra. For $LiGa_2$ the first example of a $[Li@Ga_{12}]$ icosahedron centered by an endohedral Li atom is found. In direct comparison with the empty $[Ga_{12}]$ icosahedra in $Li_{11}Ga_{24}$ and in $Li_{6-x}Ga_{14}$ the geometric

details (d_{Ga-Ga} = 2.62–2.74 Å in $LiGa_2$, 2.51–2.67 Å in $Li_{11}Ga_{24}$ and 2.62–2.68 Å in $Li_{6-x}Ga_{14}$) show a slight enlargment of the icosahedral unit. This together with the analysis of the residual electron density present in the center of the $[Ga_{12}]$ icosahedron in $LiGa_2$ supports the interpretation of the unusual $[Li@Ga_{12}]$ situation rather than artefacts caused by the epitactic intergrowth of $LiGa_2$ with $Li_{6-x}Ga_{14}$.

From our thermochemical analyses it becomes clear that strong kinetic effects influence the thermal effects detectable in DSC studies in the Ga-rich part of the Li–Ga system. As the Ga-rich part generally shows the relevant effects at rather low temperatures, this does not come as a surprise and may be the reason for the multiple irreconceivable attempts in literature to establish the phase relations on the basis of thermoanalytical data. The combination of single crystal and powder diffraction with detailed thermochemical studies gives a clearer picture now, and the phases in the Ga-rich part of the Li–Ga phase diagram most probably can be given as $LiGa_6$, $Li_{6-x}Ga_{14}$ with $2 \leq x \leq 3$, $LiGa_{3.42}$, $Li_{11}Ga_{24}$, $LiGa_2$ and LiGa.

References

[1] J. Saint, M. Morcrette, D. Larcher, J. M. Tarascon, Exploring the Li–Ga room temperature phase diagram and the electrochemical performances of the Li_xGa_y alloys vs. Li. *Solid State Ionics* **176** (2005) 189-197, DOI: 10.1016/j.ssi.2004.05.021.

[2] A. Kuhn, O. Gerbig, C. Zhu, F. Falkenberg, J. Maier, B. V. Lotsch, A new ultrafast superionic Li-conductor: ion dynamics in $Li_{11}Si{-}2PS_{12}$ and comparison with other tetragonal LGPS-type electrolytes. *Phys. Chem. Chem. Phys.* **16** (2014) 14669-14674, DOI: 10.1039/C4CP02046D.

[3] T. Holzmann, L. M. Schoop, M. N. Ali, I. Moudrakovski, G. Gregori, J. Maier, R. Cava, B. V. Lotsch, $Li_{0.6}[Li_{0.2}Sn_{0.8}S_2]$ – a layered lithium superionic conductor. *Energy Environ. Sci.* **9** (2016) 2578-2585, DOI: 10.1039/C6EE00633G.

[4] H. Watanabe, N. Kijima, Synthesis of $Sr_{0.99}Eu_{0.01}AlSiN_3$ from intermetallic precursor. *J. Ceram. Soc. Jpn.* **117** (2009) 115-119, DOI 10.2109/jcersj2.117.115.

[5] T. P. Yadav, R. S. Tiwary, O. N. Srivastava, N. K. Mukhopadhay, Evolution of a Nanocrystalline (Co,Ni)Al_2O_4 Spinel Phase from Quasicrystalline Precursor. *Int. J. Appl. Ceram. Techn.* **5** (2008) 449-457, DOI: 10.1111/j.1744-7402.2008.02243.x.

[6] J. Sappl, F. Jung, C. Hoch, Facile One-Step Syntheses of Several Complex Ionic Lithium Gallates from LiGa as Intermetallic Precursors. *Chem. Mater.*, **32** (2020) 866-873, DOI: 10.1021/acs.chemmater.9b04540.

[7] E. Zintl, G. Brauer, Über die Valenzelektronenregel und die Atomradien unedler Metalle in Legierungen. *Z. Phys. Chem.* **B20** (1933) 245-271, DOI: 10.1515/zpch-1933-2023.

[8] G. E. Jang, I. M. Curelaru, M. P. Hentschel, Growth and characterization of large single crystals of the intermetallic compound Li-Ga (Zintl). *J. Cryst. Growth* **141** (1994) 399-403, DOI: 10.1016/0022-0248(94)90245-3.

[9] V. V. Kinzhibalo, E. V. Mel'nik, O. F. Zmiy, An investigation of the ternary Mg-Li-(Ga, Ge, In, Tl, Pb) systems. *Izv. Akad. Nauk SSSR Met.* **1979** (1979) 193-196; in Russian; Transl.: *Russ. Metall.* **1979** (1979) 192-196.

[10] W. Bockelmann, H. U. Schuster, Kristallchemische Aspekte ternärer Phasen des Lithiums mit 3B- und 4B-Elementen in elektrovalenter und nicht elektrovalenter Zusammensetzung. *Z. Anorg. Allg. Chem.* **410** (1974) 241-250, DOI: 10.1002/zaac.19744100304.

[11] S. P. Yatsenko, Peculiarities chemical interaction of Ga in binary alloys. *J. Chim. Phys.* **74** (1977) 836-843, DOI: 10.1051/jcp/1977740836.

[12] P. Eckerlin, I. Maak, A. Rabenau, Über Mischkristallbildung in den Systemen $(NH_4)_3AlF_6$-$(NH_4)_3GaF_6$ und LiAl-LiGa. *Z. Anorg. Allg. Chem.* **327** (1964) 143-146, DOI: 10.1002/zaac.19643270307.

[13] H. Nowotny, F. Holub, Untersuchungen an metallischen Systemen mit Flußspatphasen. *Monatsh. Chem.* **91** (1960) 877-887, DOI: 10.1007/BF00929560.

[14] Y. Grin, A. O. Fedorchuk, The influence of crystalline structure of phases on constitution of the (Y, Sm)-Li-Ga phase diagram. *Izv. Akad. Nauk SSSR Met.* **24** (1992) 206-209; in Russian; Transl.: *Russ. Metall.* **5** (1992) 197-200.

[15] E. Vollmar, H. Ehrenberg, M. Knapp, Low-temperature behaviour of the Zintl phases $Li_{1-x}Ga_x$ and $Li_{1-x}In_x$ with decreasing lithium content. *Z. Kristallogr. Suppl.* **S21** (2004) 112a.

[16] R. Thümmel, W. Klemm, Das Verhalten der Alkalimetalle zu den Metallen der Gruppe IIIB. *Z. Anorg. Allg. Chem.* **376** (1970) 44-63, DOI: 10.1002/zaac.19703760107.

[17] W. Müller, J. Stöhr, Die Kristallstruktur von Li_2Ga und Li_3Ga_2. *Z. Naturforsch.* **B32** (1977) 631-636, DOI: 10.1515/znb-1977-0607.

[18] S. P. Yatsenko, K. A. Chuntonov, S. I. Alyamovsky, E. N. Diyeva, *Izv. Akad. Nauk SSSR Met.* **1** (1973) 185-188.; in Russian; Transl.: *Russ. Metall.* **1** (1973) 131-133.

[19] C. Belin, R.-G. Ling, The unexpected lithium-deficient phase of Li_3Ga_7: Synthesis and X-ray structure of Li_3Ga_{14} *J. Solid State Chem.* **45** (1982) 290-292, DOI: 10.1016/0022-4596(82)90285-7.

[20] J. Stoehr, H. Schäfer, Ga-Clusterverbände im Li_3Ga_{14}. *Rev. Chim. Minér.* **19** (1982) 122-127.

[21] M. Tillard-Charbonnel, C. Belin, J. L. Soubeyroux, The lithium-gallium intermetallic system: electrochemical and neutron powder diffraction study of the lithium deficient phase Li_2Ga_7. *Eur. J. Solid State Inorg. Chem.* **27** (1990) 759-769.

[22] J. Stöhr, H. Schäfer, Darstellung und Struktur von Li_5Ga_4. *Z. Anorg. Allg. Chem.* **474** (1981) 221-225.

[23] C. Belin, Synthesis and crystal structure of the nonstoichiometric phase $LiGa_{3.42}$. *Rev. Chim. Minér.* **21** (1984) 263-272.

[24] M. Tillard-Charbonnel, C. Belin, Le système lithium–gallium. Redétermination du diagramme des équilibres de phases dans le domaine Ga–LiGa. *Compt. rend. Acad. Sci. Paris*, **306** (1988) 1161-1164.

[25] J. Sangster, A. D. Pelton, The Ga–Li (Gallium–Lithium) System. *J. Phase Equilib.* **12** (1991) 33-36, DOI: 10.1007/BF02663670.

[26] T. Itami, M. Shimoji, W. van der Lugt, Study of the Li–Ga system by differential scanning calorimetry. *J. Less Common Met.* **152** (1989) 75-86, DOI: 10.1016/0022-5088(89)90073-8.

[27] B. Predel, *Ga-Li (Gallium - Lithium)*, in: Phase Equilibria, Crystallographic and Thermodynamic Data of Binary Alloys, vol. IV/12C, (Springer, Berlin, Heidelberg) (2013), pp. 91-92.

[28] A. A. Coelho, TOPAS and TOPAS-Academic: an optimization program integrating computer algebra and crystallographic objects written in C++. *J. Appl. Cryst.* **51** (2018) 210-218, DOI: 10.1107/S1600576718000183.

[29] A. L. Spek, Single-crystal structure validation with the program PLATON. *J. Appl. Cryst.* **36** (2003) 7-13, DOI: 10.1107/S0021889802022112.

[30] B. B. Toby, R. B. Von Dreele, GSAS-II: the genesis of a modern open-source all purpose crystallography software package. *J. Appl. Cryst.* **46** (2013) 544-549, DOI: 10.1107/S0021889813003531.

[31] APEX3 V.2018.1-0, Bruker AXS Inc. (Madison, USA), (2018).

[32] SADABS V.2.03, Bruker AXS Inc. (Madison, USA), (2018).

[33] G. M. Sheldrick, A short history of SHELX. *Acta Crystallogr.* **A64** (2008) 112-122, DOI: 10.1107/S0108767307043930.

[34] Proteus - Thermal analysis Version 6.1.0, Netzsch GmbH (Selb, Germany), (2016).

[35] P. Blaha, K. Schwarz, F. Tran, R. Laskowski, G. K. H. Madsen, L. D. Marks, WIEN2k: An APW+lo program for calculating the properties of solids. *J. Chem. Phys.* **152** (2020) 074101, DOI: 10.1063/1.5143061.

[36] G. Kresse, J. Furthmüller, Efficient iterative schemes for ab initio total-energy calculations using a plane-wave basis set. *Phys. Rev. B* **54** (1996) 11169, DOI: 10.1103/PhysRevB.54.11169.

[37] J. P. Perdew, K. Burke, M. Ernzerhof, Generalized Gradient Approximation Made Simple. *Phys. Rev. Lett.* **77** (1996) 3865-3868, DOI: 10.1103/PhysRevLett.77.3865.

[38] J. P. Perdew, K. Burke, M. Ernzerhof, Generalized Gradient Approximation Made Simple (Erratum). *Phys. Rev. Lett.* **78** (1997) 1396, DOI: 10.1103/PhysRevLett.78.1396.

[39] H. J. Monkhorst, J. D. Pack, Special points for Brillouin-zone integrations. *Phys. Rev. B* **13** (1976) 5188-5192, DOI: 10.1103/PhysRevB.13.5188.

[40] A. D. Becke, E. R. Johnson, A simple effective potential for exchange. *J. Chem. Phys.* **124** (2006) 221101, DOI: 10.1063/1.2213970.

[41] M. C. Tegel, Iron pnictide superconductors. PhD thesis, LMU München, (2011). online available under https://edoc.ub.uni-muenchen.de/13019/

[42] F. Tambornino, J. Sappl, F. Pultar, T. M. Cong, S. Hübner, T. Giftthaler, C. Hoch, Electrocrystallization: A Synthetic Method for Intermetallic Phases with Polar Metal-Metal Bonding. *Inorg. Chem.* **55** (2016) 11551-11559, DOI: 10.1021/acs.inorgchem.6b02068.

[43] N. N. Greenwood, A. Earnshaw, Chemistry of the Elements, 2nd ed., Butterworth-Heinemann (Oxford, UK), (1997).

[44] V. Petricek, M. Dusek, JANA2000 V.30-01-2003, Institute of Physics, Czech Academy of Sciences (Prague, Czech Republic), (2000).

[45] L. W. Finger, M. Kroeker, B. H. Toby, DRAWxtl, an open-source computer program to produce crystal-structure drawings. *J. Appl. Cryst.* **40** (2007) 188-192, DOI: 10.1107/S0021889806051557.

[46] L. M. Gelato, E. Parthé, STRUCTURE TIDY – a computer program to standardize crystal structure data. *J. Appl. Cryst.*, **1987**, **20** (1987) 139-143, DOI: 10.1107/S0021889887086965.

[47] C. Kittel, Introduction to Solid State Physics, 8th edition, p. 149, Wiley & Sons (Hoboken, New Jersey, USA), (2005).

[48] J. Emsley, The Elements, 3rd edition, p. 26, Oxford University Press (Oxford, Great Britain), (1998).

[49] R. A. Matula, Electrical Resistivity of Copper, Gold, Palladium, and Silver. *J. Phys. Chem. Ref. Data* **8** (1979) 1147-1298, DOI: 10.1063/1.555614.

[50] M. Shur, Physics of Semiconductor Devices, p. 623, Prentice Hall (Englewood Cliffs, New Jersey, USA), (1990).

[51] R. Paul, Feldeffekttransistoren, in: Elektronische Halbleiterbauelemente, p. 377-413, Teubner-Studienskripten, Vieweg+Teubner Verlag (Wiesbaden, Germany), (1989).

[52] F. Tambornino, C. Hoch, Bad metal behaviour in the new Hg-rich amalgam KHg_6 with polar metallic bonding. *J. Alloys Compd. 618* (2015) 299-304, DOI: 10.1016/j.jallcom.2014.08.173.

[53] C. Hoch, A. Simon, $Na_{11}Hg_{52}$ - Complexity in a polar metal. *Angew. Chem.*, **2012**, *124*, 3316-3319; *Angew. Chem. Int. Ed.* **51** (2012) 3262-3265, DOI: 10.1002/anie.201108064.

[54] O. Gunnarsson, M. Calandra, J. E. Han, Saturation of electrical resistivity. *Rev. Mod. Phys.* **75** (2003) 1085-1099, DOI: 10.1103/RevModPhys.75.1085.

[55] A. F. Ioffe, A. R. Regel, Non-crystalline, amorphous and liquid electronic semiconductors. *Prog. Semicond.* **4** (1960) 237-291.

[56] N. E. Hussey, K. Takenaka, H. Takagi, Universality of the Mott–Ioffe–Regel limit in metals. *Philos. Mag.* **84** (2004) 2847-286, DOI: 10.1080/14786430410001716944.

[57] M. Calandra, O. Gunnarsson, Electrical resistivity at large temperatures: Saturation and lack thereof. *Phys. Rev.* **B 66** (2002) 205105.

[58] L. De Medici, J. Mravlje, A. Georges, Janus-Faced Inuence of Hund's Rule Coupling in Strongly Correlated Materials. *Phys. Rev. Lett.* **107** (2011) 256401, DOI: 10.1103/PhysRevLett.107.256401.

[59] P. Villars, K. Cenzual, Pearson's Crystal Data – Crystal Structure Data Base for Inorganic Compounds, Release 2017, ASM International (Materials Park, Ohio, USA), (2017).

[60] R. Nesper, Structure and chemical bonding in Zintl-phases containing lithium. *Prog. Solid St. Chem.* **20** (1990) 1-45, DOI: 10.1016/0079-6786(90)90006-2.

Chapter 3

Summary

3.1 Cu_3Hg - a New Binary Copper Amalgam

During this work a new Cu-rich amalgam (Cu_3Hg, for illustration see Fig. 3.1) was synthesized via electrocrystallization (see Chapter 2.1). The compound forms well-shaped crystals with bronze luster and with a hexagonal unit cell (space group $P6_3/mmc$, a = 5.408(4) Å, c = 4.390(3) Å) in the Ni_3Sn structure type. The exact composition is $Cu_{3.11}Hg_{0.89}$ due to some mixed occupancy of Cu on the Hg site.

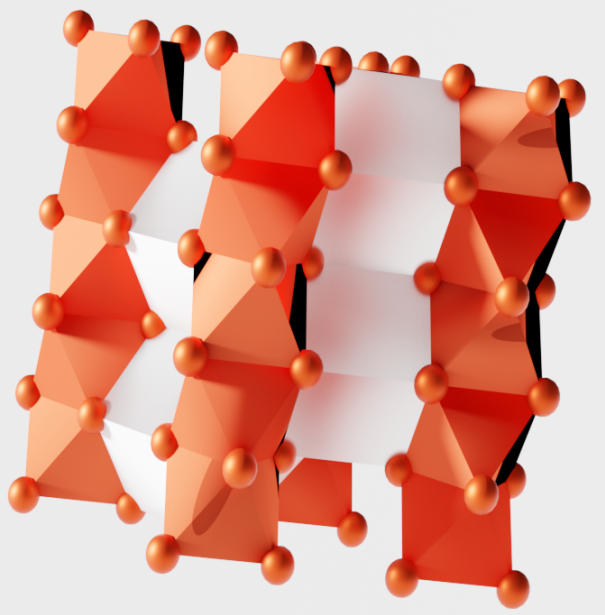

Figure 3.1: Illustration of the crystal structure of the copper amalgam Cu_3Hg. For structural details see Chapter 2.1.

Normally the Hg is located on the Ni site of the Ni_3Sn structure type, which makes Cu_3Hg the first example, were the Hg is mainly located on the Sn site. Cu_3Hg is together with the already known Cu_7Hg_6 (γ-brass structure) the only phase known in the Cu/Hg phase diagram and therefore relevant for dental amalgams. The formation of the new copper amalgam was the serendipitous outcome of a synthesis aimed at a uranium amalgam by electrocrystallization. To confirm the composition EDX (energy-dispersive X-ray spectroscopy) measurements were taken. Cu_3Hg is stable against air and moisture, but can be thermally decomposed under dynamic vacuum, resulting in nanostructured copper networks, which could be interesting in terms of catalytic applications. Furthermore, we discussed, based on the radii quotient, the possibility of other amalgams with the composition A_3Hg (A = Cr, Mn, Fe, Co and Ni). This Cu-rich amalgam may be the basis of the widely spread "copper penny proof", used to test the presence of Hg compounds in a simple qualitative inorganic analysis.

3.2 LiGa as an Intermetallic Precursor

In Chapter 2.2 the use of the intermetallic phase LiGa (illustration in Figure 3.2) as precursor for the preparation of $LiGaO_2$ (LGO), $LiGaS_2$ (LGS), $LiGa_5O_8$ and Li_3GaN_2 is shown, presenting a new way to synthesize these compounds. Especially $LiGaS_2$ is a promising material for direct down-conversion of laser wavelengths to mid-IR. Intermetallic precursors can simplify the preparation of many compounds, because they do not require fastidious control over thermochemical and stoichiometric parameters. As byproducts $LiGa_5O_8$ and Li_3GaN_2 were found, which could also be of interest for applications. The lattice parameter, calculated electronic structure and ion conductivity of $LiGaO_2$ and $LiGaS_2$ were revisited. This work shows, that the use of intermetallic precursors is a valuable yet widely underestimated pathway for simple preparative access to functional materials.

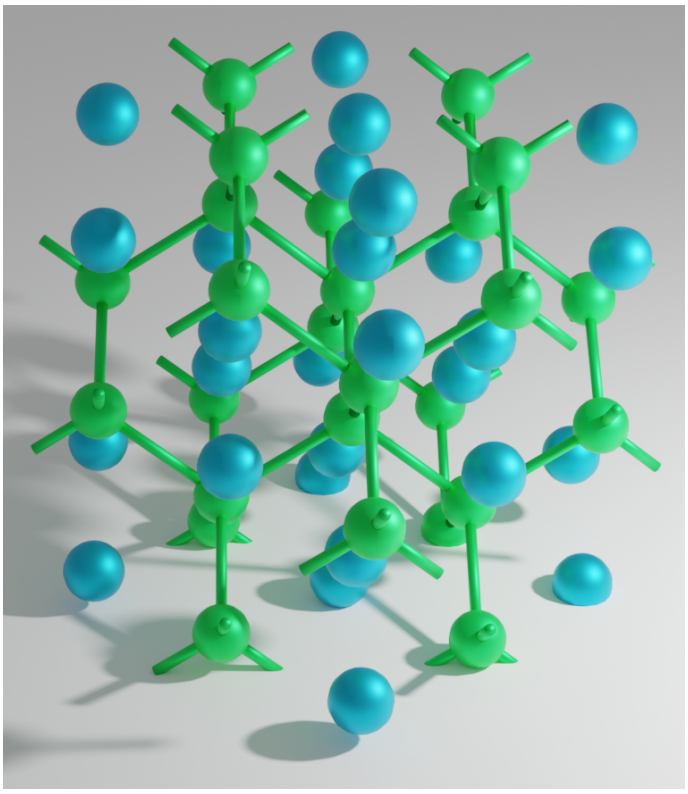

Figure 3.2: Illustration of the crystal structure of LiGa. For more details see Chapter 2.2

3.3 $LiGa_6$, $Li_{11}Ga_{24}$, and $LiGa_2$ - Three Binary Main Group Phases

During this work three new binary phases from main group elements were synthesized (see Chapter 2.3). $LiGa_6$, $Li_{11}Ga_{24}$, and $LiGa_2$ (illustration in Figure 3.3). With the help of X-ray single crystal structure refinements their structures were determined. All three compounds adopt new structure types. $LiGa_6$, the Ga-richest phase, crystallizes with the trigonal space group $R\bar{3}c$ (No. 167, a = 6.1851(8) Å, c = 23.467(4) Å), $LiGa_2$ crystallizes with the orthorhombic space group *Cmce* (No. 64 a = 8.5167(7) Å, b = 14.4826(11) Å, c = 15.2959(14) Å), and $Li_{11}Ga_{24}$ with the hexagonal space group $P6_3mc$ (No. 186, a = 13.7700(19) Å, c = 23.250(5) Å). The crystals show bright metallic luster. They are synthesized in weld-sealed Ta ampules starting from the pure elements. DSC (differential scanning calorimetry) measurements were taken to determine peritectical decomposition temperatures. The three lithium gallides can be interpreted as non-classical Zintl phases, because they do not form electron-precise Zintl phases and they combine ionic, covalent and metallic bonding contributions. The bonding situations and electronic structures, in the case of $LiGa_6$ and $LiGa_2$, have been analyzed by DFT calculations. They show typical features of polar metals (see Chapter 1). Furthermore, electronic resistivity measurements on Ga, LiGa, Li_3Ga_{14} and $LiGa_6$ have been performed.

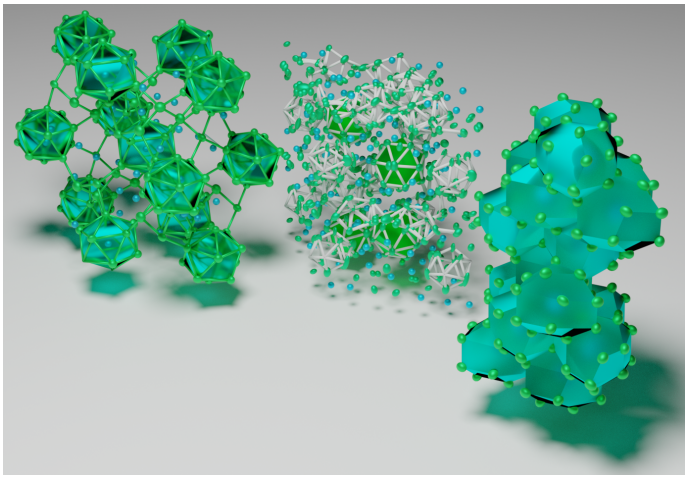

Figure 3.3: Illustration of the crystal structures of three new Li-Ga phases. From left to right: $LiGa_2$, $Li_{11}Ga_{24}$ and $LiGa_6$. For structural details see Chapter 2.3

Chapter 4

Conclusion and Outlook

Extension of the Concept of Polar Intermetallic Compounds on Ternary Phases

Based on the concept described in Chapter 1.5 we showed that the combination of Li and Ga creates compounds with a polar metal bonding. This concept can now be broadened, either by exchanging the element on the left side of the Zintl border (Ga) by In or Tl, or by adding a third element. It could also be possible to find other Ga-rich phases in the alkali metal/Ga systems, such as sodium, potassium, rubidium or cesium gallides (see Table 1.1). Electrocrystallization could be an access to new compounds which have not been synthesized in these systems before. However, these are not expected to be equally high significance in terms of polar metal bonding. Belin and Ling[1] have shown that the Ga-rich phases $Na_{22}Ga_{39}$, KGa_3, K_3Ga_{13}, $RbGa_7$ and $CsGa_7$ can be interpreted as electron-precise Zintl compounds according to Wade's electron counting procedure. The authors pinpointed that this method works perfectly for the named compounds but fails for Li_3Ga_{14}. In order to extend this chemstry to ternary compounds, we suggest to combine one element from the left side of the Zintl border (Ga), a second element chosen from alkali or alkaline earth metals with a third element which does not form classical Zintl phases (e.g. transition metal or rare-earth elements). In Table 4.1 an overview of possible combinations of potential alkali/alkaline earth metal + Ga + d10 element is given. These combinations are of great interest because of d10 elements no Zintl phases are known. For the Ca-Zn-Ga system and the Ca-Cd-Ga system there are already reports that some of these ternary compounds (see Table 4.1) can be interpreted as intermetallic compounds with polar metal bonding.[2] As mentioned, the figure could be extended by further transition metals or rare-earth elements, however, we intend to show that this limited number of elements already contains many possibilities worth looking on.

To state a proof of principle we have selected the combination Ba, Zn and Ga. Zn and Ga are known for forming an eutecticum at a low melting point ($24,67$°C, 3.87 A-%)[12], therefore it is interesting for isothermic electrocrystallization. Zinc is a d_{10} element and known to form no binary phases with Ga. There are many known phases of Ba-Ga and Ba-Zn, respectively, like $BaGa_2$[13], $BaGa_4$[14], BaZn[15] or $BaZn_2$[16]. Ba would probably form a cation or a cation-like state due to

Table 4.1: Table of potential systems for ternary Ga compounds with polar metal bonding (limited on Zn and Cd + alkali and alkaline earth metals), Yellow: Systems already known to form ternary phases with Ga, Green: no known ternary phases with Ga.

	Li	**Na**	**K**	**Rb**	**Cs**
Zn	$Li_{11.33}Zn_{2.66}Ga_{22.13}$ [3] $Li_{38}(Zn_{0.337}Ga_{0.663})_{101.06}$ [4]	$Na_{17}Zn_{11.86}Ga_{38.18}$ [5]			
Cd	$Li_{58}Cd_{16}Ga_{128}$ [6]	$Na_{35}Cd_{23.77}Ga_{56.23}$ [7]			
	Be	**Mg**	**Ca**	**Sr**	**Ba**
Zn			$Ca(Zn_{0.2}Ga_{1.8})$ [2] $Ca(Zn_{0.5}Ga_{1.5})$ [2] $Ca(Zn_{1.5}Ga_{0.5})$ [2]		
Cd			$Ca(Cd_{0.24}Ga_{1.74})$ [2] $Ca(Cd_{0.76}Ga_{1.24})$ [2] $Ca_{10.73}Cd_{1.40}Ga_{5.87}$ [2] $Ca_5(Cd_{0.76}Ga_{2.24})$ [2] $Ca(Cd_{0.696}Ga_{1.304})$ [8]	$Sr(Cd_{0.98}Ga_{1.02})$ [2] $SrCd_{1.32}Ga_{0.68}$ [9] $SrCd_2Ga_2$ [10]	$BaCd_{3.2}Ga_{0.8}$ [11]

its low electronegativity compared to the others. First experiments of reacting Ba, Zn and Ga in a 1:1:1 ratio at 700°C in sealed tantalum ampoule were performed, resulting in a compound with the probable composition 1:1:1 and an unknown byproduct. Single crystal diffraction was performed, pointing to a new structure type which can be derived from the CaB_6 structure type. A major difference is that the octahedra (containing both Ga and Zn) form double layers. Two layers of octahedra, respectively, are superimposed and linked, while the next two layers are displaced by (1/2 1/2 0) (see Figure 4.1). We expected Zn and Ga to be separated by Ba within the structure, but that is not the case. The preliminary structure model rather suggests a mixed Ga/Zn occupation. The structure yet has many unsolved problems. It is also to early to discuss this compound in terms of a polar metal bonding, however, the existence of a new phase shows the value of studies on ternary phases in the above-mentioned sense.

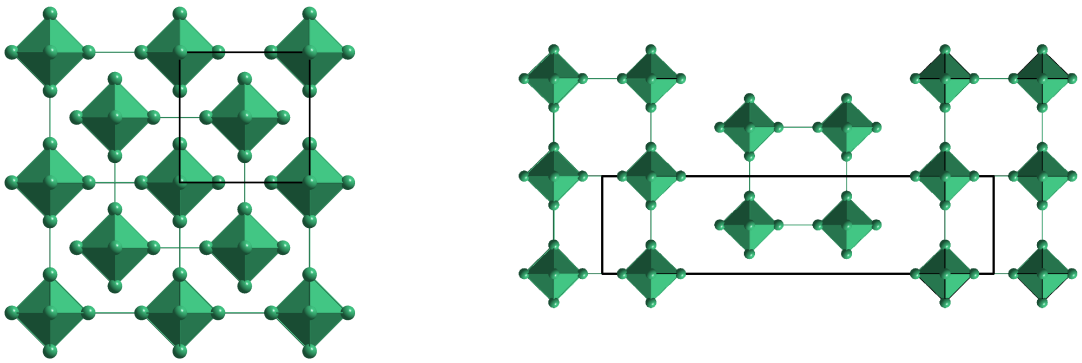

Figure 4.1: Arrangement of the octahedron in the yet not fully refined structure of "BaZnGa". Left: view along the *c* axis, Right: view along the *b* axis.

Revisiting Known Phases with Modern Crystallographic Methods

During our work on the Li-Ga system we also revisited a number of already published phases. In the case of $LiGa_{3.42}$ [17] we simplified the synthesis (which is normally obtained by reduction of Li_3Ga_{14} with cerium or barium and is now available by a simple ampule Li-Ga reaction) and measured some high-quality single crystals. We observed some discrepancies between the diffraction pattern and the reported structure model which may indicate the existence of a modulated structure. This crystallographic study is not finished yet and will extend beyond this work.

New Amalgam Phases with Transition Elements

As mentioned in Chapter 2.1.4, it is assumed that the quotient of the atomic radii is a reason for the formation of Cu_3Hg. Cu_3Hg is rather unusual in composition, since amalgams exhibiting the Ni_3Hg structure type are normally formed according to the formula AHg_3 (A = non-Hg metal). If the quotient of the atomic radii plays a major role in the formation of Cu_3Hg, the respective amalgams of Cr, Mn, Fe, Co, and Ni should also be realizable.

So far only binary amalgam systems were used for isothermic electrocrystallization. It would be interesting to use multiple non-Hg metals simultaneously, such as Na/K or Ba/Sr. This could lead to new phases with interesting properties in terms of bad metal behavior. Today, only little is known about the existence of ternary amalgams. In the alkali/alkaline earth metals Hg system only four ternary compounds known so far (Li_2MgHg [18], $Li_6Ca_{17}Hg_9$ [19], $Li_6Sr_{17}Hg_9$ [19] and $K_{29}NaHg_{48}$ [20]) In Table 4.2 an overview on feasible ternary amalgams based on alkali and alkaline earth metals is given. This matrix can further be expanded by including transition and lanthanoid metals.

Table 4.2: Table of potential systems for ternary amalgams with multiply alkali or alkaline earth metals. Grey: Binary systems, Yellow: Systems with bad scatter contrast or doubtful phase formation, Green: Possible ternary amalgams.

	Li	**Na**	**K**	**Rb**	**Cs**	**Be**	**Mg**	**Ca**	**Sr**	**Ba**
Li										
Na										
K										
Rb										
Cs										
Be										
Mg										
Ca										
Sr										
Ba										

In many ways, this work has created a basis on which to build on. It did not only show the advantages and limitations of the isothermal electrolysis, but also the diversity of binary phases which still can be found even with simple preparative techniques like thermochemical syntheses from the elements

in sealed Ta ampoules with the help of careful thermoanalytic studies. Furthermore, it has depicted the advantage of intermetallic precursors, a synthesis method which is widely underestimated. To underline this statement LiGa was used in the preparation of a number of ternary compounds, see Chapter 2.2. Now that the feasibility of this concept has been proven it can be developed even further. Starting materials that are more complex in terms of structure or even ternary starting materials could be applied. This could lead to quaternary compounds or compounds with an even higher number of different elements, typically very delicate to be obtained from conventional synthetic procedures. It has also been shown that the concept of combining an alkali metal with an element located on the left side of the Zintl border (Ga) (see Chapter 1) results in polar metal bonding and has therefore cleared the way for a systematic synthesis of these compounds.

In order to establish general structure-property relations for polar intermetallic phases, it is of high importance to gain a basis of a large number of individual compounds. Starting from a broad basis, general trends and underlying principles become visible. Today, a targetted access to phases with polar metal-metal bonding is not at hand, but with this work we have shown different feasible pathways with this aim. Future work based on our considerations which have been exemplified to be expedient and productive will lead to deeper insight into the behavior of polar metallic compounds.

References

[1] C. Belin, R. G. Ling, The Intermetallic Phases of Gallium and Alkali Metals. Interpretation of the Structures according to Wade's Electron-Counting Methods *J. Solid State Chem.* **48** (1983) 40-48, DOI: 10.1016/0022-4596(83)90057-9.

[2] W. Harms, Dissertation thesis, Polare intermetallische Phasen AM und AM_2 (A= Ca, Sr, Ba; M= Ga, In Zn, Cd, Hg, Cu, Ag, Au). Kristallchemie, chemische Bindung und Eigenschaften. Universität Freiburg/Breisgau, Germany (2008).

[3] M. Tillard-Charbonnel, A. Chahine, C. Belin, A new intermetallic phase in the ternary system: Lithium-zinc-gallium, a hexagonal-type arrangement of extended icosahedral units. *Mater. Res. Bull.* **28** (1993) 1285-1294, DOI: 10.1016/0025-5408(93)90176-E.

[4] M. Tillard-Charbonnel, N. Chouaibi, C. Belin, J. Lapasset, Synthesis of the new ternary intermetallic phase $Li_{38}(Ga_xZn_{1-x})_{101}$, x ca. 0.663, displaying a hexagonal crystal superstructure. Structural approach in the subcell unit. *Eur. J. Solid State Inorg. Chem.* **29** (1992) 347-359.

[5] M. Tillard-Charbonnel, N. Chouaibi, C. Belin, Synthese et etude structurale de la nouvelle phase ternaire stoechiometrique $Na_{17}Zn_{12}Ga_{40.5}$. *C. R. Acad. Sci.* **315** (1992) 661-665.

[6] M. Tillard-Charbonnel, N. Chouaibi, C. Belin, Crystal structure of lithium cadmium gallium (58/16/128), $Li_{58}Cd_{16}Ga_{128}$. *Z. Kristallogr.* **209** (1994) 280-280, DOI: 10.1524/zkri.1994.209.3.280.

[7] M. Tillard-Charbonnel, C. Belin, Modelling of icosahedral frameworks of gallium: A new disordered intermetallic phase with sodium and cadmium, structure and bonding. *Mater. Res. Bull.* **27** (1992) 1277-1286, DOI: 10.1016/0025-5408(92)90092-E.

[8] G. Cordier, T. Friedrich, Crystal structure of calcium cadmium gallium (1/0.7/1.3), $CaCd_{0.7}Ga_{1.3}$. *Z. Kristallogr.* **201** (1992) 312-313, DOI: 10.1524/zkri.1992.201.14.312.

[9] G. Cordier, T. Friedrich, Crystal structure of strontium cadmium gallium (1/1.3/0.7), $SrCd_{1.3}Ga_{0.7}$. *Z. Kristallogr.* **201** (1992) 314-315, DOI: 10.1524/zkri.1992.201.14.314.

[10] G. Cordier, T. Friedrich, Crystal structure of strontium cadmium gallium (1/2/2), $SrCd_2Ga_2$. *Z. Kristallogr.* **201** (1992) 316-317, DOI: 10.1524/zkri.1992.201.14.316.

[11] G. Cordier, T. Friedrich, Crystal structure of barium cadmium gallium (1/3.2/0.8), $BaCd_{3.2}Ga_{0.8}$. *Z. Kristallogr.* **201** (1992) 318-319, DOI: 10.1524/zkri.1992.201.14.318.

[12] T. B. Massalski, H. Okamoto, P. R. Subramanian, L. Kacprzak. *Binary Alloy Phase Diagrams* (A S M Intl (Oh), Ohio, USA., 1990).

[13] G. Bruzzone, I sistemi binari Ca-Ga, Sr-Ga, Ba-Ga. *Bull. Sci. Fac. Chim. Ind. Bologna* **24** (1966) 113-132.

[14] G. Bruzzone, MX_4 compounds of alkaline earth metals with IIIB group elements. *Acta Crytallogr.* **18** (1965) 1081-1082, DOI: 10.1107/S0365110X65002578.

[15] R. Ferro, Il composto BaZn. *Atti Accad. Naz. Lincei* **17** (1954) 256-258.

[16] G. Bruzzone, M. Ferretti, F. Merlo, The Ba-Zn system. *J. Less-Common Met.* **114** (1985) 305-310, DOI: 10.1016/0022-5088(85)90448-5.

[17] C. Belin, Synthesis and crystal structure of the nonstoichiometric phase Li $Ga_{3.42}$. *Rev. Chim. Miner.* **21** (1984) 263-271.

[18] H. Pauly, A. Weiss, H. Witte, Kubisch flaechenzentrierte Legierungen der Zusammensetzung Li_2MgX mit raumzentrierter Unterstruktur. *Z. Metallkd.* **59** (1968) 414-418.

[19] A. V. Tkachuk, A. Mar, $Li_6A_{17}Hg_9$ (A = Ca, Sr, Yb): Intermetallic compounds of mercury with a Zeolite-like topology of cubic networks. *Chem. - Eur. J.* **15** (2009) 10348-10351, DOI: 10.1002/chem.200902250.

[20] H. J. Deiseroth, E. Biehl, $NaK_{29}Hg_{48}$: A contradiction to or an extension of theoretical concepts to rationalize the structures of complex intermetallics? *J. Solid State Chem.* **147** (1999) 177-184, DOI: 10.1006/jssc.1999.8209.

Chapter 5

List of Publications

1. Stuck in Our Teeth? Crystal Structure of a New Copper Amalgam, Cu_3Hg

Jonathan Sappl, Ralph Freund and Constantin Hoch
Published in: *Crystals* **7** (2017) 352, DOI: 10.3390/cryst7120352.

J. Sappl supervised the practical work, prepared the single-crystal samples and performed all analyses. C. Hoch conceptualized the studies and wrote the manuscript. R. Freund performed the synthesis.

2. Facile One-Step Syntheses of Several Complex Ionic Lithium Gallates from LiGa as Intermetallic Precursor

Jonathan Sappl, Felix Jung and Constantin Hoch
Published in: *Chem. Mater.* **32** (2020) 866-873, DOI: 10.1021/acs.chemmater.9b04540.

J. Sappl conceptualized and supervised the practical work, performed PXRD measurements and Rietveld refinements and wrote the manuscript, which was supervised by C. Hoch. F. Jung performed synthesis. A. K. Hatz performed electrochemical impedance measurements, J. Obel ICP–OES measurements, and R. Niklaus DFT calculations.

3. Synthesis and Crystal Structure of Three Ga-rich Lithium Gallides, $LiGa_6$, $Li_{11}Ga_{24}$ and $LiGa_2$

Jonathan Sappl and Constantin Hoch
Published in: *Inorg. Chem.* **59** (2020) 6566–6580. DOI: 10.1021/acs.inorgchem.0c00674.

Conceptualization were performed by J. Sappl, who also did all practical work and performed analyses. The manuscript was written by J. Sappl and C. Hoch, who supervised the project. DFT calculations were performed by R. Niklaus and F. Tambornino. Conductivity measurements were performed by R. Schönmann.